Polymorphism of Protein Condensates

A Dissertation

Presented to

the Faculty of the Department of Chemical & Biomolecular Engineering

University of Houston

In Partial Fulfilment

of the Requirement for the Degree

Doctor of Philosophy

In Chemical & Biomolecular Engineering

by

Mohammad S. Safari

May 2018

Polymorphism of Protein Condensates

_____

Mohammad S. Safari

Approved:

_____
Chair of the Committee
Peter G. Vekilov, Professor
Dept. Chemical & Biomolecular engineering

_____
Co-chair of the Committee
Jacinta C. Conrad, Associate Professor
Dept. Chemical & Biomolecular engineering

Committee Members:

_____
Megan Robertson, Associate Professor
Dept. Chemical & Biomolecular engineering

_____
Navin Varadarajan, Associate Professor
Dept. Chemical & Biomolecular engineering

_____
Vassiliy Lubchenko, Associate Professor
Dept. Chemistry

_____
Anatoly B. Kolomeisky, Professor
Dept. Chemistry (Rice University)

_____
Suresh K. Khator, Associate Dean
Cullen College of engineering

_____
Michael Harold, Professor and Chair
Dept. Chemical & Biomolecular engineering

Acknowledgements

I would like to gratefully acknowledge various people without whom this thesis would not have been written. I would like to thank my advisors Dr. Peter G. Vekilov and Jacinta C. Conrad whose help, support and guidance were so important in persuasion of my PhD. degree. They always encouraged me in the route of research and professional success, and without their support and guidance, none of my accomplishments would have achieved.

I wish to express my sincere thanks to Dr. Anatoly B. Kolomeisky for his insightful ideas in p53 condensation project and for the valuable discussions and meetings to find the proper pathway to tackle the project.

I would like to thank Dr. Vassiliy Lubchenko, Dr. Megan Robertson, and Dr. Navin Varadrajan for their kindest presence as my committee members and the valuable, constructive suggestions during my qualifier, proposal and defense.

I am extremely grateful to Dr. Patrick C. Cirino, Dr. Navin Varadrajan, and Dr. Richard C. Willson for providing me the opportunity to work in their lab without which several chapters of my research would not have been established. I would like to thank Zhiqing Wang for all the training and insightful discussions in the molecular biology field that helped me develop the p53 project.

I acknowledge the grants for funding support which made my PhD possible including NASA (NNX14AD68G to P.G.V. and J.C.C.), NSF (DMR-1151133, to J.C.C.), and the Welch Foundation (E-1869, to J.C.C.).

In the end, I would like to sincerely thank Dr. Vekilov one more time to provide me the opportunity to explore new fields that was beyond the scope of my initial research goals.

Polymorphism of Protein Condensates

A Dissertation

Presented to

the Faculty of the Department of Chemical & Biomolecular Engineering

University of Houston

In Partial Fulfilment

of the Requirement for the Degree

Doctor of Philosophy

In Chemical & Biomolecular Engineering

by

Mohammad S. Safari

May 2018

Abstract

Protein misfolding followed by aggregation is the major cause of neurodegenerative diseases such as Alzheimer's, Parkinson's, familial amyloid poly neuropathy (FAP), Huntington's, type-II diabetes, etc. Common aspect of all protein aggregation diseases is the altered protein conformation known as partially unfolded amyloidogenic intermediate that is capable of assembly into amyloid structures. Recently discovered mesoscopic protein-rich clusters may act as crucial precursors for the nucleation of ordered protein solids, such as crystals, sickle hemoglobin polymers, and amyloid fibrils. These clusters challenge settled paradigms of protein condensation as the constituent protein molecules present features characteristic of both partially misfolded and native proteins. Some of their unusual features include the kinetically determined size, thermodynamically controlled number, and their distinct nature from aggregation triggered by reduction of the intramolecular S−S bonds and amyloid aggregates. We investigated the role of protein structural flexibility on its ability to induce formation of mesoscopic clusters for multiple proteins including the p53, known as guardian of genome, which contains multi dis-ordered and β-sheet rich domains; hemoglobin A, which is the major component of red blood cells and contains a compact structure rich in α-helices; antimicrobial enzyme lysozyme which is a robust model in study of protein aggregation. Whereas lysozyme and hemoglobin A demonstrate mesoscopic clusters at high protein concentrations, p53, whose aggregation is tied to cancer development, exhibits clustering at physiological temperatures for low concentrations of the protein. These findings suggest that the clusters are a product of limited protein structural flexibility. Furthermore, we discovered that the crowding environment of the inside cell significantly promotes clustering of intrinsic disordered proteins (IDPs) such as p53. About half of human cancers are associated with mutations of the tumor suppressor p53. Mutated p53 emerges as a powerful oncogene, which blocks the activity of wild-type p53 and several distinct

anticancer pathways. The gained functions of the mutant have been related to the aggregation behaviors of wild-type and mutant p53. Our data reveals that in presence of crowders, the p53 clusters can capture some of the crowder molecules, which causes steric hindrance effects and raises the nucleation barrier of the aggregation. Thus these clusters can potentially act as storage of proteins and protect them from formation of toxic amyloid aggregates by providing sufficient time for the proteomic and chaperonin machinery to clear out or refold the misfolded aggregated species in the cell. The nucleation of p53 fibrils deviates from the accepted mechanism of sequential association of single solute molecule. We find the mesoscopic clusters serve as a pre-assembled precursor of high p53 concentration that facilitate fibril assembly. Fibril nucleation hosted by precursors represents a novel biological pathway, which awards unexplored avenues to suppression of protein fibrillation in aggregation diseases.

Table of Contents

List of Figures

Figure 14.3. Maturation of p53-rich clusters. (A-G) Representative OIM image collected after each incubation time. The observed volume is 5 × 80 × 120 μm^3. Clusters appear as red spots. Temperatures is set at 15 ℃ and Ficoll and p53 concentrations are 56 ml^{-1}mg and 1.2 μM respectively. (B-C) The average size and number of the clusters as a function of time determined by OIM. The average of five determinations in distinct solution volumes is shown. Error bars indicate standard deviations. The p53 concentration is 1.2 μM. The inset indicates normalized fluorescence emission at λ = 500 nm of p53 solution in presence of 8-Anilinonaphthalene-1-sulfonic acid (ANS) measured using excitation at λ = 350 nm with 56 mg ml^{-1} Ficoll (red triangles) and without Ficoll (black rectangles) for incubation at T = 15 ℃ for 4 hours with 40 minutes interval. The p53 and ANS concentrations are 7.7 and 850 μM respectively. The emission intensity is normalized to the maximum value observed in presence of fibrillar aggregates. 53

Figure 15.3. Reversibility and nucleation and growth of p53 fibrils. (A-B) Representative fluorescence micrograph of Thioflavin T (ThT) binding to fibrillar p53 aggregates formed by incubation of protein sample at 37 ℃ over 12 hours (A) with no Ficoll and (B) with 56 mg ml^{-1} Ficoll. The ThT and p53 concentrations are 200 μM and 7.7 μM respectively. (C-D) Representative fluorescence micrograph of incorporation of Ficoll into p53 aggregates formed by incubation at 37 ℃ over 12 hours in presence of fluorescein labeled Ficoll at 56 mg ml^{-1} (C) with no protein and (D) with 7.7 μM p53. (E) Concentration determination of p53 using UV-Vis spectrophotometry after incubation at T = 37 ℃ in presence of 56 mg ml^{-1} Ficoll. Black triangles show concentration of p53 solution after filtration to remove any formed aggregates after incubation. Green rectangles demonstrate the concentration of p53 incorporated into the fibrillar p53 aggregates, calculated by subtraction of initial concentration of p53 from the final value. (F) Intensity correlation functions of p53 solutions for three concentration of protein obtained by serial dilution of the stock at 1.5 μM to 1.3 and 0.9 μM. (G) The dependence of volume fraction of

List of Tables

Chapter 1 Introduction

Neurodegenerative diseases

Protein misfolding is the main cause of neurodegenerative diseases such as Alzheimer's, Parkinson's, familial amyloid poly neuropathy (FAP), Huntington's, type-II diabetes and etc.[1-4]. Although the general pathway of amyloid diseases resembles prion disorders, there exists fundamental differences between prion and protein aggregation disorders. Prion diseases are infections and are not known to be associated with protein misfolding. They are caused due to folding of the 142 amino acid PrP polypeptide to a different secondary structure known as PrP^{Sc} which contains longer β-sheets and shorter α-helix compared to the original native structure defined as PrP^{C}. The folded PrP^{Sc} undergoes incomplete proteolytic cleavage to generate short fragment PrP (27-30) that aggregates into amyloids [5-9].

Amyloid aggregates

Common aspect of all protein aggregation diseases is the altered protein conformation known as partially unfolded amyloidogenic intermediate that is capable of assembly into amyloid structures[10, 11]. Amyloid structures are cross β-sheets with their β-strands oriented perpendicular to the fibril axis. X-ray diffraction and synchrotron experiments revealed two repeating spaces of 4.8 and 10 A°, respectively indicating the spacing of the β-strands along the fibril axis and the average spacing of the β-sheets perpendicular to the fibril axis. The inner β-sheet spacing may vary from 8–20 A° depending on protein amino acid sequence and side chain conformations. One generic proposed structure for amyloids core is the helical cross sheets in which 24 strands with repeated spacing of 4.8 A° with total length of 115.5 A° are oriented along the fiber axis with further twist of 0–30° to facilitate extension of hydrogen bonding between the strands over the total fibril length [12-14]. Although formation of amyloid fibrils is a generic property of any polypeptide sequence, it is not yet deeply understood how these structures form

under cell regulatory machinery. One explanation to this question is the likelihood of formation of partially unfolded intermediates by loss of protein folding cooperativity due to single amino acid mutations that destabilizes protein native conformation[10, 11]. Another route for protein aggregation is the exhaustion of the proteomic and chaperonin system. Accumulation of misfolded or oxidized states of proteins in cells due to aging can result in inability of the proteomic system that can ultimately result in cell death[15-19] . Nevertheless, primary oligomers that form in early stages of protein aggregation expose hydrophobic residues on surface that can promote aberrant protein interactions to induce further downstream lethal responses to cell survival[20, 21].

Alzheimer's

An example is the Alzheimer's disease (AD). The causative genes of AD are located on chromosome 21, 14, and 1, respectively encoding a transmembrane protein knowns as APP (amyloid precursor protein), presenilin 1, and presenilin 2 (PS1, PS2) [22]. Aβ peptide is produced from the larger amyloid-precursor protein (APP) through two sequential enzymatic activities, β- and γ-secretase[23]. β-Secretase activity (mostly attributed to the BACE1 protein in the brain) is usually thought of as the rate limiting enzyme in Aβ production. β-Secretase activity leaves a membrane bound C-terminal fragment which is then cleaved by γ-secretase. This final cleavage generates the secreted Aβ in the cytosol, which may suggest information about the function of APP. The majority of Aβ is 40 amino acids long (Aβ40), however, a small fraction (<10%) is the more hydrophobic Aβ42. Higher levels of Aβ42, the more hydrophobic sequence facilitates the assembly of Aβ into more order structures including dimers and all the insoluble plaques that can further deposit in the brain [22, 23]. The mechanism of synapses damage and neurodegeneration through Aβ monomer/oligomers is not yet clear, however, formation of pore-like structures with channel activity [24], alterations in glutamate receptors and excitotoxicity [25], circuitry hyper-

excitability, mitochondrial dysfunction, lysosomal failure, and alterations in signaling pathways related to synaptic plasticity are investigated as possible pathways [22, 23, 26-29].

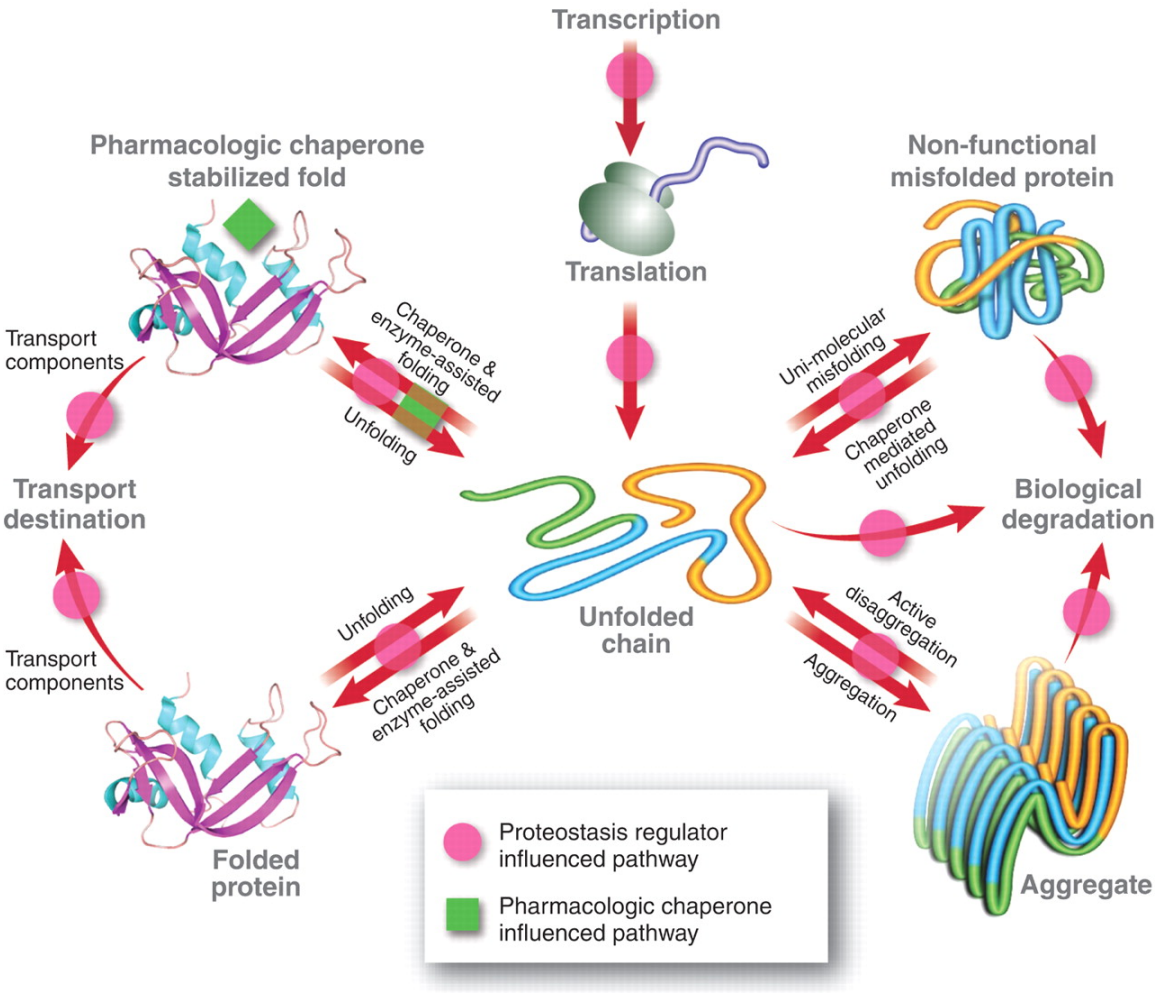

Figure 1.1. A proteostasis network comprising pathways represented by the red arrows. Imbalances in proteostasis often lead to disease and, therefore, proteostasis regulators (magenta circles) that manipulate the proteostasis pathways/network can restore protein homeostasis and ameliorate both loss- and gain-of-function diseases [17].

The mechanism of aggregation of Aβ peptide is suggested as nucleation dependent polymerization. Several studies reported that Aβ can exist as two conformations, β-sheet and α-helix. In a nucleation dependent aggregation, the lag phase is delayed by nucleation events that require molecules to overcome the energy barrier which alters significantly with folding state of protein. Controversially, both of the reported conformations are hypothesized to be the active

ensemble [30], however what is common in existing literature is that the oligomerization of Aβ may be the primary cause of neuron damage and synapses failure [26-28, 31, 32].

Huntington's

Another example is Huntington diseases which is caused by CAG triplet repeat in the exon of HTT gene that encodes an expanded poly-glutamine(Q) stretch in the huntingtin (HTT) protein [33, 34]. HTT is a very large protein (~375 kDa) predicted to consist mainly of repeated units of about 50 amino acids, termed HEAT repeat. These repeats are composed of two antiparallel α-helices with a helical hairpin configuration which assemble into a super helical structure with a continuous hydrophobic core[35]. HTT has many interaction partners, particularly at its N-terminus, suggesting that it serves as a scaffold to coordinate complexes of other proteins. The cellular functions of HTT are still not completely understood, however, the protein is mostly cytoplasmic, with membrane attachment via palmitoylation at cysteine 214 [36]. The appearance of the large poly-glutamine repeat in the HTT protein can result in conformational changes which is hypothesized to be the main trigger to pathogenic cascade. The structure of the Q17-HTT (HTT with 17 poly-glutamine repeat) bound to antibody 3B5H10 which recognizes the toxic form of the poly-glutamine, revealed that polyQ chain is constructed of a compact hairpin with two β-strands and a turn. These findings have suggested that the toxic conformation is composed of short β strands interspersed with β turns so that the strands are held together in an antiparallel conformation by intramolecular (and intermolecular) hydrogen bonds[37-39].

As in case of the Alzheimer's, oligomerization of polyQ plays a vital role in Huntington's disease progression by impairing the regular cell metabolism[34]. In a recent study, it was demonstrated that that glia (connective tissue of neuron cells) regulate steady-state numbers of HTT aggregates expressed in neurons through a clearance mechanism that requires the glial scavenger receptor Draper and downstream phagocytic engulfment machinery. Remarkably,

some of these captured HTT aggregates effect prion-like conversion of soluble, wild-type HTT in the neuron cells cytoplasm [40, 41]. Crucial aspect of the protein aggregation diseases is the formation of the misfolded proteins prone to toxic assemblies. In addition, generation of these assemblies results in the failure of the proteostasis machinery leading into diseases categorized as loss of function (LoF) and gain of function (GoF) disorders [17]. Loss-of-function diseases are typically caused by mutations leading to protein misfolding and degradation. Gain-of-toxic-function diseases, on the other hand, appear to arise when aggregation-associated proteotoxicity dominates over clearance inside or outside the cell[1, 15, 18, 22, 23, 25, 29, 33, 40].

Cancer and p53 aggregation

Protein aggregation is not only the cause of neurodegenerative diseases but it can also result in cancer [42-51]. One protein known as guardian of genome or p53 has demonstrated aggregation in cancer tumor cell lines[52]. The p53 is a regulatory protein that controls gene expressions using the DBD domain. It has a flexible N-terminal, a DNA binding domain as well as oligomerization domain in the C-terminal. It consists of several well-defined domains including a multipartite N-terminal transactivation (TA) domain (residues 1–73), a proline-rich region (63–97), the centrally located and highly conserved DNA-binding core domain (DBD) (residues 94–312), and within the C-terminus are located its tetramerization domain (residues 324–355) followed by an unstructured basic domain (CTD) (residues 360–393). The p53 is known to form tetrameric state using the oligomerization domain [53]. Under normal environment, p53 is eliminated following ubiquitin E3 ligase degradation with Mdm2[54]. Upon stress however, this gene is over expressed to repair DNA damage or signaling pathway. In cancer cells this protein has demonstrated single mutations known as somatic mutations. Two common types of p53 mutations are structural and contact mutations [46, 53].

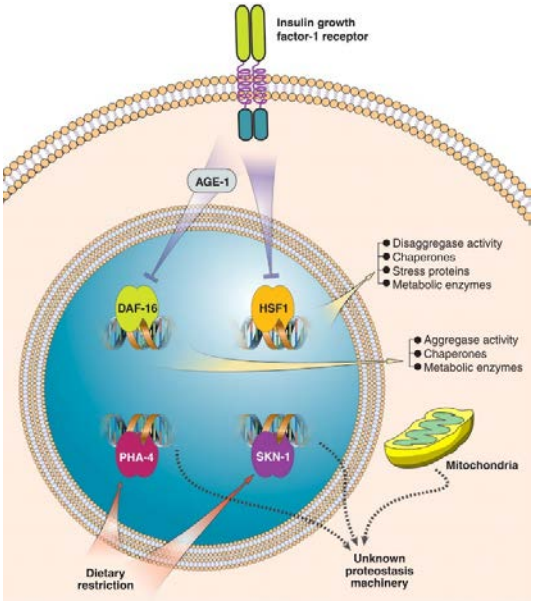

Figure 2.1. Signaling pathways that control longevity and youthfulness strongly influence proteostasis. The insulin growth factor-1 receptor signaling pathway negatively regulates the activity of the transcription factors DAF-16 and HSF-1.

The contact mutants impair the DNA binding ability of p53 while the structural mutants mostly destabilize the native folding conformation that result in protein aggregation. One major outcome of aggregation is loss of function in nucleus which leads the stress response un-repaired [55, 56].

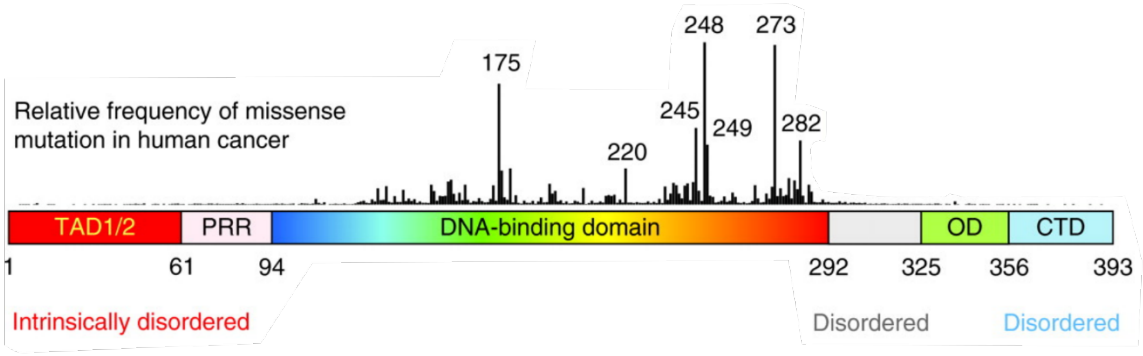

Figure 3.1. Hot spot mutants of p53[57]

In general, emergence of p53 mutation within a cell might have three non-exclusive outcome; First, it can affect the TP53 allele, reducing the overall capacity of the cell to mount proper p53 response; exert dominant negative effects by co-expressing the wtp53 or forming

mixed tetramers with p53 family (p63,p73) and rendering their functions and third, by possessing activities and regulating transcription factors that can contribute to tumor progression know as gain of function (GOF).[45] For example, accumulation of mutp53 has caused suppression of p73 resulting in accumulation of cells with polypoid and different aberrant chromosomes facilitating cancerous behavior. One recent research has reported that interaction of mutp53 with p63 can disrupt the TGF-β/Smad signaling resulting in cell metastasis and invasion[58]. Beside all the negative effects of mutant and hetero tetramerization mechanisms, posttranslational modification of wtp53 can also render the transcriptional activities of the protein. Questions such as why post translational modifications affect aggregation or oligomerization of p53 are still under poorly understood [51, 59, 60]. As discussed earlier, formation of the toxic misfolded conformation of proteins can result in impairment of cell regulatory functions, cell death and ultimately progression and metastasis of the protein aggregation diseases. Most of these aggregation pathways follow the common sigmoidal kinetics where nucleation events are the rate determining step for the process. In the case of protein aggregation the structure of protein in the lag phase of this process is poorly understood. Multiple theories is been proposed for the possible slow kinetics. In one theory, the presence of a higher β-sheet conformer is essential for further aggregation. The state with higher β-sheet content is named active ensemble in some cases and facilitates formation of further fibrillation [61-64].

Mesoscopic protein-rich clusters; new insights into protein condensation

About a decade ago Vekilov et al., reported formation of dense liquid protein-rich clusters in presence of high protein concentrations [65-67]. First observation was detected upon odd nucleation measurements, when the nucleation rate dropped after a critical temperature[68, 69]. Experimental data demonstrated that these protein rich clusters occupy about 10^{-4} – 10^{-7} volume fraction of the solution with the size varying from 50 – 100 nm [63, 65, 70, 71]. Simulation data

suggested that the number of these clusters are thermodynamically controlled while the size depends on the formation of a transient dimer that stabilize the life time of these clusters by small fluctuations on the excess free energy of the protein mixture[72-75]. The mesoscopic clusters have been a focus of recent investigations mostly because they present essential sites for the nucleation of ordered solids of both folded proteins, such as crystals[76-78] and sickle cell hemoglobin polymers[67], and partially misfolded chains that form amyloid fibrils[79, 80]. Nucleation of ordered protein solids is the crucial first step in the formation of each condensate, and its rate largely determines the rate of condensation. The number of nuclei is limited by a free energy barrier, whereas the growth of the nucleated domains obeys the general chemical kinetics laws[62]. A protein solution supersaturated with respect to a condensate overcomes the nucleation barrier by means of localized fluctuations that bring the solute concentration close to that of the incipient phase. According to classical nucleation theory, the rarity of successful transitions over the barrier strongly delays nucleation and con-strains the overall growth rate of the condensate[81, 82]. Surprisingly, recent experimental measurements of nucleation rates revealed that they are even lower, by many orders of magnitude, than those predicted by theory [67, 68, 71, 83]. The issue of low nucleation rates and several other unexplained features of protein nucleation kinetics was resolved by the discovery that the mesoscopic protein-rich clusters are a crucial precursor for the nuclei of ordered protein solids. This finding underscores the urgent need for in-depth understanding of the structure and formation mechanisms of the mesoscopic clusters. The mesoscopic clusters challenge basic paradigms of protein condensation. Although the clusters are likely liquid, they exist under conditions that are distinct from those of the macroscopic protein dense liquid [65, 70, 75, 78]. The clusters are much larger than the prediction of colloid clustering models that are often applied to protein condensation. The cluster size is steady and independent of the parameters that define the solution thermodynamics, such

as pH, ionic strength, and protein concentration. By contrast, the fraction of the protein captured in the clusters is determined by the protein chemical potential. A recent theory, supported by experimental evidence, explained several puzzling cluster behaviors. This model posits that the mesoscopic clusters consist of a concentrated mixture of intact protein monomers and an additional protein species, emerging at the elevated protein concentration within the clusters[72, 75].

Role of dense liquid clusters in protein condensation (open Q&A)

This cluster scenario raises several fundamental questions on the cluster composition and mechanisms. Are the mesoscopic clusters similar to amyloid fibrils, which also consist of partially unfolded protein? How different are they from fully disordered proteins, which make up amorphous aggregates? Is the chemical integrity of the protein molecules in the clusters preserved, including the disulfide bonds? Does protein nucleation occur inside these clusters? How does crowding affect protein condensation?

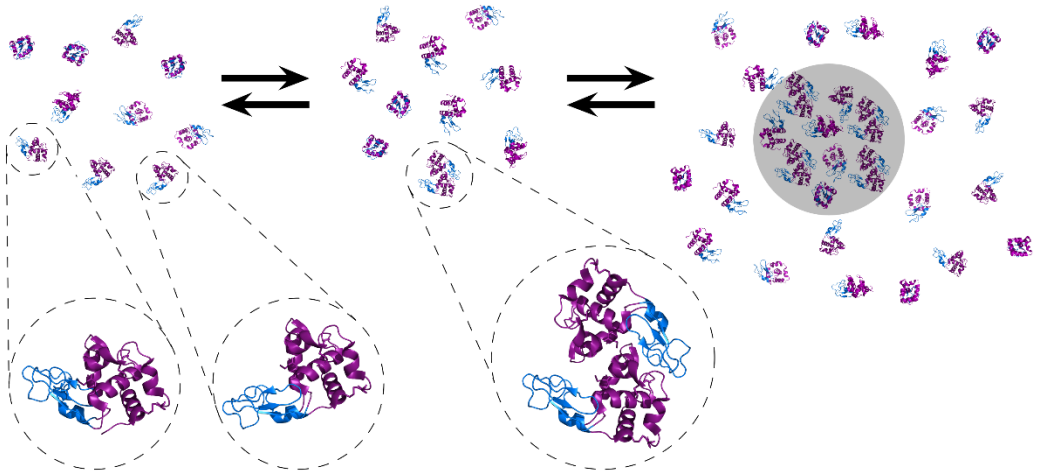

Figure 4.1 The mechanism of formation of the mesoscopic protein-rich clusters in lysozyme solution. Protein native monomers, partially unfolded monomers, and domain-swapped dimers are shown in the callouts. The α and β domains, identified as in McCammon, et al. are highlighted in purple and blue, respectively. A cluster, highlighted in grey in the right panel, is a region of high protein concentration, into which monomers diffuse and convert to dimers. The dimers migrate back into the solution, where they decay into monomers.

In my Ph.D. work, we addressed these questions by experiments with the protein lysozyme, an antimicrobial enzyme, whose easy availability from hen egg white has allowed the accumulation of a significant database of its biochemical and biophysical properties. We further investigated the effect of protein structure by testing the ability of multi domain protein p53 that contains dis-ordered and folded domains for assembly into mesoscopic clusters and fibrillar aggregates in regular and crowded environment. Unlike lysozyme that requires high concentrations to exhibit mesoscopic clusters, we observed that crowding by 10% (v/v) can promote formation of p53-rich clusters that obtain more than 70% of the available protein. We also investigated the effect of Ficoll on kinetics of fibril formation and our findings revealed that crowding perturbed the nucleation and growth of the fibrillar aggregates in opposite directions; whereas nucleation was slower in presence of crowder, the growth was faster. This effect is counterintuitive; the faster growth can be explained in terms of excluded volume effects that Ficoll induces as a crowder which facilitate protein condensation, however the reason for slower nucleation rate is not crystal clear. Our fluorescence microscopy revealed that Ficoll was incorporating in p53 clusters that facilitate nucleation of fibrils, thus decreases the local p53 concentration inside clusters resulting in slower nucleation rates that are exponent function of protein concentration. To investigate the role of protein folding on cluster formation we examined the effect of shear flow to temporarily stabilize the formation of partially folded conformation and tested the clustering ability of the protein conformer[5, 84]. Our findings demonstrated that perturbation of the protein conformation by shearing solutions of the protein lysozyme greater than 20 s^{-1} applied for longer than 1 hour reduced the volume of the cluster population. In previously published literature, it was also reported that crystal morphology changes in protein crystallization experiments performed under microgravity in ribonuclease

S[85], insulin[86], and lysozyme. Together with all these findings, we decided to investigate the role of microgravity and significantly low shear flow on mesoscopic protein-rich clusters.

To study the behavior of clusters under zero shear flow, experiments are required to be accomplished on International Space Station (ISS) and the only available setup available on ISS is a camera and Light Microscopy Module (LMM). To apply ISS setup to our study we established a recent method known as differential dynamic microscopy (DDM) [87-90] that allows characterization of dynamics of submicron particles below the microscope resolution. Whereas the method is simply applying a light microscopy to generate scattering field correlation function, it requires PYTHON/MATLAB image processing algorithm to generate the diffusion speckle. We established DDM to study weakly scattering protein-rich clusters and we found out that this method can also be applied to measure protein clusters dispersity and allows the user to resolve the dynamics of bidisperse suspension of particles as low volume fraction ratio of large/small particles as 0.003 and size ratios above 20 where traditional light scattering techniques such as DLS fails to detect any signal of larger particles. With our current findings on DDM, we will be able to examine the effect of microgravity on clustering mechanism by ISS station equipment.

Chapter 2 Polymorphism of lysozyme condensates

Introduction

Nucleation although well studied, it is still poorly understood. Nucleation rate measurements of protein lysozyme crystals revealed discrepancies of ten or more orders of magnitude slower than the predictions of the classical nucleation theory[68]. In separate experiments, it was demonstrated that nucleation rate of lysozyme crystals in presence of 3-4% NaCl was independent of the protein concentration above a certain critical concertation and the phenomenon was not as consequence of liquid-liquid separation of the protein at high concentrations[91]. Based on these observations, our group put forward the idea of mesoscopic protein-rich clusters that act as nucleation precursors for two step nucleation events. Recent simulation data coupled with experiments revealed some unique features of these clusters including thermodynamically controlled number, kinetically determined size, and partially folded conformation of the protein inside the cluster core[67, 69, 72, 74, 77, 78, 92]. This cluster scenario raises several fundamental questions on the cluster composition and mechanisms. Are the mesoscopic clusters similar to amyloid fibrils, which also consist of partially unfolded protein? How different are they from fully disordered proteins, which make up amorphous aggregates? Is the chemical integrity of the protein molecules in the clusters preserved, including the disulfide bonds? In view of the irreversibility of some protein aggregates, is cluster formation reversible? Here, we address these questions by experiments with the protein lysozyme, an antimicrobial enzyme, whose easy availability from hen egg white has allowed the accumulation of a significant database of its biochemical and biophysical properties.

Material and methods

All products are used without any further purification. Lyophilized lysozyme and Conjugated HRP-A11 are purchased from Fischer Scientific and Abcam. TCEP (tris(2-carboxyethyl)phosphine, 8-Anilinonaphthalene-1-sulfonic acid (ANS), Thioflavin T (ThT) and DTNB

(5,5'-dithio-bis-(2-nitrobenzoic acid)) are purchase from Sigma Aldrich. Lysozyme was dissolved at ~160 mg ml^{-1} in 20 Mm HEPES buffer. Protein concentration was determined by absorbance measurements using a Beckman Coulter Du 800 spectrophotometer and extinction coefficient ε = 2.64 ml $mg^{-1}cm^{-1}$ at 280 nm[93]. To remove the salts from lyophilized powder, the solution is buffer exchanged using GE healthcare PD-10 desalting columns to remove the salts. After buffer exchange protein solution is set at 60 mg/ml and filtered through 0.22 µm Polyethersulfone (PES) syringe filters prior to all measurements. TCEP (tris(2-carboxyethyl)phosphine was dissolved in HEPES buffer to concentration of 0.2 M. 8-Anilinonaphthalene-1-sulfonic acid (ANS) was dissolved in HEPES buffer to concentration of 20 mM. ANS and ThT stock solutions are prepared in HEPES buffer at 21 and 5 mM. Concentrations are measured spectrophotometry using wavelengths of 270 and 375 nm for ANS and 416 nm for ThT in ethanol with extinction coefficients of 18, 8 and 26.6 $mM^{-1}cm^{-1}$ subsequently[94-98]. DTNB (5,5'-dithio-bis-(2-nitrobenzoic acid)) was prepared by dissolving in HEPES buffer at concentration 8 mg/ml. All solutions are with filtered 0.22 µm PTFE (Polytetrafluoroethylene) filters prior to all measurements.

Quantification of Broken S-S Bonds The disulfide bridges in lysozyme were reduced by (tris(2-carboxyethyl)phosphine (TCEP)[99-102]. To eliminate unreacted TCEP, TCEP was eliminated first by buffer exchange. To quantify the number of sulfhydryl SH groups formed as a result of the reduction with TCEP or other solution treatments, we added Elman's reagent, 5,5'-dithio-bis-(2-nitrobenzoic acid) (DTNB),[103-105] which forms a 5-thio-2-nitrobenzoic acid (TNB) at a concertation equivalent to that of the sulfhydryl. To prepare a calibration curve for sulfhydryl measurements, we used L-cysteine and glutathione. We prepared solutions of L-cysteine and glutathione with concentrations 0 , 0.25, 0.5 , 0.75, 1.0 , 1.25 and 1.5 mM in 0.1 M potassium phosphate buffer with 0.1mM EDTA, pH = 8.0. We used black NUNC 96 well plates for all the measurement using a plate reader**.** 20 µl of each sample is mixed with 4 µl of DTNB stock and 176

µl of 0.1 M potassium phosphate buffer was added to each well. Absorbance at 412 nm was measured 20 minutes after mixing. Measurements were also checked by calculating the theoretical absorbance using an extinction coefficient of 14150 $cm^{-1}M^{-1}$ for TNB. For each sulfhydryl concentration, the three values from L-cysteine, glutathione and theoretical was averaged and the standard deviation is reported as error bars. To find out the optical path length of 96 well plate, each measurement is also repeated using the Beckman Coulter Du 800 spectrophotometer and the slope of the line was 1.85 ± 0.05.

ThT, ANS, and DTNB assay for lysozyme structural integrity The conformational integrity of lysozyme was tested using the 1-anilino-8-naphthalenesulfonate (ANS) and Thioflavin T (ThT) assays. ANS was dissolved at 13 mM in 20 mM HEPES at pH = 7.8. The solution was filtered through a 0.2 µm Teflon filter. The ANS concentration was determined spectrophotometrically using extinction coefficient 18 mM^{-1} cm^{-1} at 270 nm.[106] 20 µL of this solution were added to 20 µL of the tested lysozyme solution and diluted with 160 µL of 20 mM HEPES to a total volume of 200 µL.[106] For experimental statistics, five identical samples of this solution mixture were loaded in a multi-well plate and the florescence response to excitation at 350 nm was recorded between 400 and 650 nm (with an increment of 5 nm) by an Infinite 200 PRO microplate reader (Tecan). ThT was dissolved at 6 mM in 20 mM HEPES at pH = 7.8. As with ANS, the solution was filtered through a 0.2 µm Teflon filter. The ThT concentration was determined spectrophotometrically using extinction coefficient 26.6 $mM^{-1}cm^{-1}$ at 416 nm.[106] 1 µL of this solution was added to 20 µL of the tested lysozyme solution and diluted with HEPES to 200 µL.[106] Five identical samples of this solution mixture were loaded in a multi-well plate and the florescence response to excitation at 442 nm was recorded between 472 and 650 nm (with an increment of 2 nm) by an Infinite 200 PRO microplate reader (Tecan).

Characterization of lysozyme activity The enzymatic activity of lysozyme was measured by monitoring the rate of absorbance decrease of a suspension of *Micrococcus lysodeikticus* (M3770 Sigma)[107]. A cell suspension is prepared by dissolving 5 mg of cells in 10 ml of 20 mM HEPES buffer. 0.2 µl of 60 mg/ml lysozyme was mixed with 250 µl of HEPES buffer. 125 µl of this solution is diluted in half with 125 µl of HEPES again and ultimately 190 ul of this final solution is added to 10 µl of the cell suspension. The lysozyme concentration was 0.05 mg/ml. The rate of absorbance decrease indicates the number of functional active sites in the solution.

Cluster characterization by oblique illumination microscopy (OIM) The method is also referred to as Browning microscopy [69, 108, 109] or particle tracking [110]. We use Nanosight LM10-HS microscope (Nanosight Ltd) to examine the Brownian motion of individual clusters in the tested solutions. We loaded a solution sample in a thermostatically controlled cuvette of volume ~ 0.3 ml and depth 0.5 mm. A green laser beam with wavelength 532 nm passes through the solution. All species in the solution scatter the incident light. The intensity scattered by a cluster is $(\frac{R_2}{R_1})^6 \approx 30^6 \approx 7.3 \times 10^6$-fold greater than that scattered by a monomer (R_1 is the monomer radius), so the clusters are well seen on the background of monomers. A 20× lens transfers the entire picture to a sensitive CMOS camera that records a movie of clusters undergoing Brownian motion. The rate of movie acquisition depends on the camera settings; in our experiments it was about 25 fps. Each frame of the movie is an image of clusters as bright white spots on a dark background. The accompanying software package determines the center of these spots in each frame of the movie and builds contiguous cluster trajectories. The cluster diffusivity is obtained from the slope of the dependence of the mean squared displacement on lag time. The cluster radius R_2 is evaluated from the Stokes-Einstein equation using viscosity values determined as discussed above. The number of cluster spots in a frame (using the focal depth of 5 µm) yields the cluster concentration.

We carefully match the movies recorded by the Nanosight device with the data file that it outputs. We found that objects recorded for times shorter than 1 s are interference spots from two or more clusters tracked for significantly longer times. This observation is supported by the estimate that a cluster with diffusivity $D_2 \approx 10^{-12}$ m^2s^{-1} would be detectable in a focal plane with depth 5 μm for about 25 s. We did not consider them as parts of the cluster population in the determination of the cluster parameters.

Dynamic light scattering (DLS) Light scattering data were collected on an instrument by ALV-GmbH, Langen, Germany, equipped with He-Ne laser operating at 632.8 nm, and an ALV-5000 EPP Multiple tau Digital Correlator. At least 5 correlation functions of 45 seconds were collected. The intensity-intensity correlation functions $g_2(\tau)$, where τ is the lag time, recorded for up to twelve hours, all possess two distinct shoulders, indicating the presence of two populations of scatters (Fig. 5.3b). We determine the characteristic diffusion times τ_m and τ_c of the monomers and clusters, respectively, by fitting the normalized correlation function with a squared sum of exponentials, $g_2(\tau) - 1 = \left(A_m \exp\left(-\tau/\tau_m\right) + A_c \exp\left(-\tau/\tau_c\right)\right)^2 + \varepsilon(\tau), (1.2)$, where A_m and A_c are the respective amplitudes, which are proportional to the intensity scattered by the monomers and clusters, and $\varepsilon(\tau)$ accounts for mechanical, optical and electronic noise in the signal[109, 111] ($\varepsilon(\tau)$ was one or two orders of magnitude lower than amplitudes A_m and A_c.

We used τ_m and τ_c to determine the monomer and cluster diffusivities, D_m and D_c, from $D_m = (q^2\tau_m)^{-1}$ and $D_c = (q^2\tau_c)^{-1}$, where $q = \frac{4\pi n}{\lambda}\sin(\theta/2)$ is the scattering wave vector at 90°, λ = 632.8 nm is the wavelength of the incident red laser and n is the solution refractive index measured as discussed in [112]. The parameters τ_m, τ_c, A_m, A_c, and ε were evaluated by non-linear curve fitting using SciPy (scipy.optimizize.minimize) routine. [113]

From τ_m, τ_c, A_m, and A_c we compute the cluster size R_c, and the hydrodynamic radius of the monomer R_m used for verification of the experimental procedures. We also evaluate the monomer diffusivity D_m, used to characterize intermolecular interaction and oligomerization. For R_i (i = m, c) we use the Stokes-Einstein relation, $R_i = \frac{k_B T q^2}{6\pi\eta_i}\tau_i$. The temperature was set at $T = 297.65$ K and k_b is the Boltzmann constant. $\eta_m = 1.025$ mPa·s is the viscosity of the buffer solution through which the monomers diffuse. The viscosity η_c was determined from the dynamics of Fluoro-Max Dyed Red Fluorescent polystyrene spheres, with diameter $2R_p$ = 2 μm, diffusing in the tested protein solution and characterized by DLS.

Identification of amyloid oligomers using antibodies To tests the amyloid nature of the protein aggregates, we used blotting with amyloid-recognizing antibodies. Conjugated anti-amyloid oligomers antibody[114] ab183461 was purchased from Abcam. A polyvinylidene fluoride (PVDF) membrane was wetted with methanol for 5 min and washed with TBS buffer (20mM Tris, 150 Mm NaCl, pH = 7.5) for 20 minutes. 4 µl of tested protein solution was injected on the membrane and allowed to penetrate for 30 mins. Blocking was performed in 5 % BSA in TBS buffer with 0.01% Tween (TBST) 20 for 1hr. The antibody concentration was set at 2µg/ml in 3% BSA/TBST and allowed to stain for 5 hr. After incubation, membrane was washed for 45 mins with TBST buffer and developed with TMB enzyme substrate from Thermo Fisher.

Induction and characterization of aggregation The mesoscopic protein-rich clusters are an intrinsic property of the solution. To assess the role of amyloid structures in cluster formation, we induced lysozyme fibrillation by heat-shocking the protein at 65, 80, or 90°C for six minutes.[64, 115, 116] The formation of amyloid structures was verified by selective binding of Thioflavin T (ThT) and 8-Anilinonaphthalene-1-sulfonic acid (ANS), detected by fluorescence excited by 442 nm for ThT and 350 nm for ANS. To compare the cluster behaviors with those of aggregates

forming after chemical modification of the protein, we reduced the intramolecular disulfide bridges using (tris(2-carboxyethyl)phosphine (TCEP).;[99-101] [99-101] Owing to the low-concentration buffer used, the addition of this acidic reagent lowered the pH by up to 0.2, to 7.6. We removed unreacted TCEP and the products of its oxidation by buffer exchange. To quantify the number of sulfhydryl, SH, groups in the native protein and those formed as a result of S-S bond reduction we used the reaction of SH with Elman's reagent, 5,5'-dithio-bis-(2-nitrobenzoic acid) (DTNB), [103, 104] which yields 5-thio-2-nitrobenzoic acid (TNB) at a concentration equivalent to that of the sulfhydryl. To ensure completeness of the reaction, we waited 20 min after the addition of DTNB. [104] We quantified the TNB concentration from its absorbance at 412 nm. In addition, we tested the presence of amyloid oligomers in the solution by immunoblotting with ab183461, an antibody that recognizes amyloid structures. The enzymatic activity of lysozyme was evaluated by monitoring the rate of absorbance decrease of a suspension of *Micrococcus lysodeikticus* in the presence of the protein.

Characterization of mesoscopic clusters

Lysozyme solutions at low ionic strength are stable against the formation of protein condensates for extended times. One expects that such solutions are homogeneous at all length scales, including the molecular. Surprisingly, observation by OIM of a 60 mg ml^{-1} (ca. 4 mM) lysozyme solution in 20 mM HEPES (at pH 7.8, at which the ionic strength is 33 mM) reveals particles suspended in the solution that randomly migrate driven by Brownian collisions, Figure 5.3a. Careful examination of all steps in the solution preparation excluded the possibility that these heterogeneities are dust particles or gas bubbles. Recording the diffusion trajectories of individual particles, we determine the radii R_c of individual particles as discussed in material and method of lysozyme section. The R_c distribution in Figure 5.2b is relatively narrow, between ca.

10 and ca. 75 nm, with an average size of ca. 40 nm. The particle number density n_c, Figure 5.2a,b, is very low and corresponds to particle volume fraction $\phi_c = 4\pi(\sum R_c^3 n_c)/3$ of ca. 10^{-6}.

Characterization of the same solution by DLS reveals the presence of two shoulders in the intensity-intensity correlation function in Figure 5.2c, with characteristic diffusion times of $\tau_m \approx$ 20 μs and $\tau_c \approx 1$ ms. We determine the diffusivities, D_m and D_c, and radii, R_m and R_c, of the two respective scatterers. After accounting for the intermolecular repulsion,[112] we obtain $R_m \approx 1.6$ nm, the hydrodynamic radius of the lysozyme monomer, whereas the average $R_c = 37$ nm is similar to that found in the OIM experiment (the somewhat higher radius detected by OIM is due to the lower wavelength used in that method, 532 nm, compared to 632.8 nm in DLS, which makes the OIM method more sensitive to larger particles)[117]. The amplitude A_c of the large scatterers is only two-fold higher than that of the monomers A_m, Figure 5.2d. The ratio A_c/A_m is proportional to both the concentration ratio of the two solution species and $(R_c/R_m)^6$.[118, 119] As $R_c/R_m \approx \tau_c/\tau_m \approx 50$, the low A_c/A_m ratio is consistent with the low particle concentration detected by OIM. Continuous DLS monitoring of the solution for 12 hours revealed that the particle size and the fraction of protein composing the particles, characterized by R_c and A_c/A_m, respectively, are steady, Figure 5.2c,d. Several characteristics of the large particles revealed by Figure 5.2a,b,c,d are unusual for both disordered protein aggregates or emerging domains of a stable phase, such as crystals or dense liquid. The narrow size distribution is inconsistent with both types of aggregation. The concentration and mesoscopic size of the particles are steady over extended times, in sharp contrast to expectations for newly formed phases in which both the domain sizes and the number of new domains grow in time.[120] On the other hand, these characteristics are typical of the mesoscopic protein-rich clusters, found in solutions of lysozyme and several other proteins at varying conditions.[75, 121-125] We conclude that the particles detected in Figure

5.2a,b,c,d are mesoscopic lysozyme-rich clusters. The size and concentration of the clusters in Figure 5.2b,d are consistent with recent *in situ* transmission electron microscopy images[126].

A crucial issue in understanding the cluster mechanism is whether the clusters adjust to the parameters of the solution, or represent irreversibly aggregated protein. To test the cluster reversibility, we monitored the dependence of R_c and A_c/A_m on the protein concentration, varied in two ways. First, we prepared a solution of 60 mg ml^{-1} and diluted it with buffer to 50, 40, and 30 mg ml^{-1}. Second, we independently prepared solutions with these four concentrations. These experiments test whether the clusters formed at the initial concentration adjust to the diluted solution, and whether newly formed clusters are similar to those resulting from transformation of preexisting condensates. The two methods of solution preparation yielded clusters with identical R_c and A_c/A_m. Figure 5.2e reveals that R_c increases by ca. 35% as the concentration is diluted from 60 to 30 mg ml^{-1}, whereas the ratio A_c/A_m decreases three-fold, indicating a similar decrease of the fraction of protein held in the clusters. Diluting a solution of irreversibly aggregated protein would lower the concentration of protein held in the clusters concurrently with the protein concentration, leading to a constant R_c and A_c/A_m. The R_c and A_c/A_m trends in Figure 5.2e demonstrate that the clusters are reversible aggregates that adjust to the conditions of the hosting solution. The decoupled behaviors of R_c and A_c/A_m, observed in Figure 5.2e, are unusual for typical phase transformations, such as freezing or vaporization, in which the size of the incipient domains increases concurrently with the volume of the new phase. On the other hand, such decoupling has been observed previously with the mesoscopic protein-rich clusters.[112] It has been attributed to the unique nature of the cluster population, whose volume is determined by the thermodynamic balance between the clusters and the solution, whereas the size of its domains results from the kinetics of formation and decay of protein dimers.[112, 113, 122, 127]

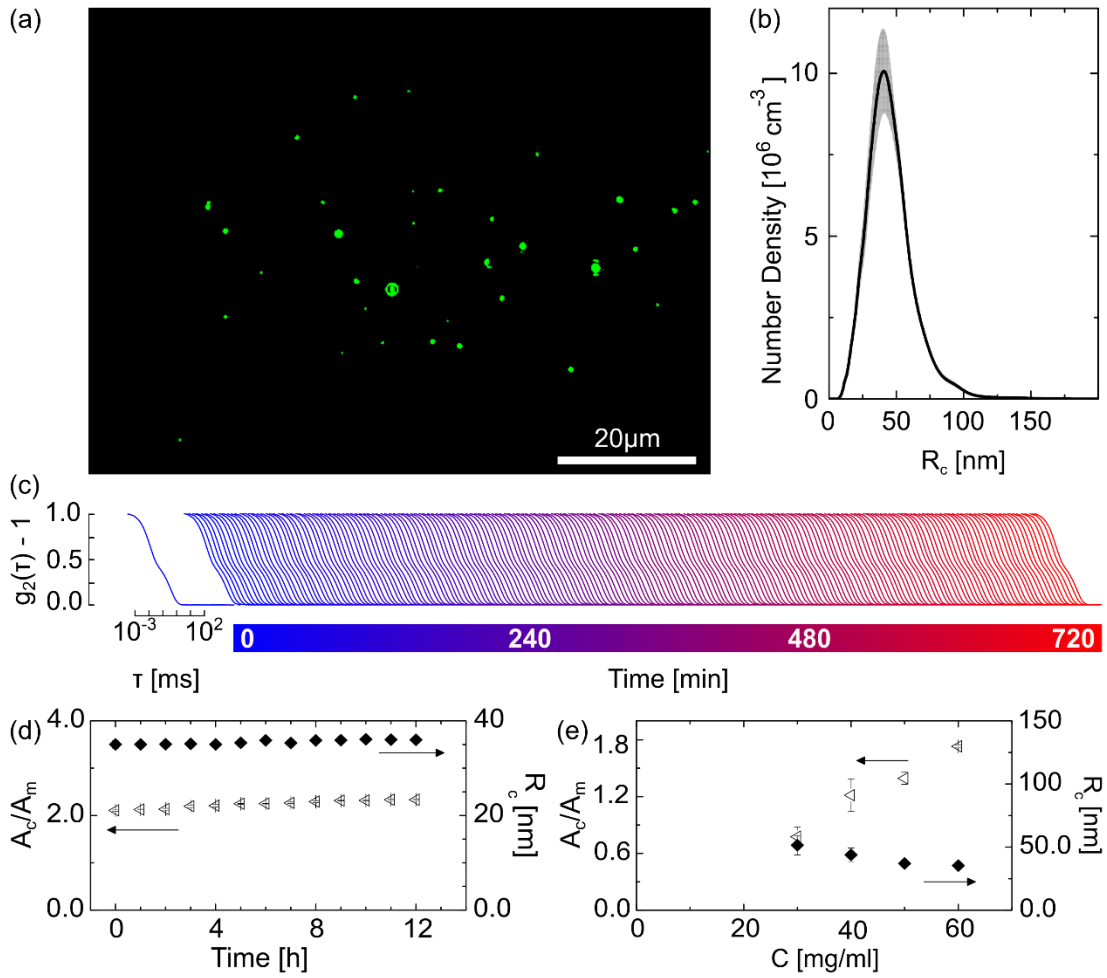

Figure 5.2. Characterization of the mesoscopic protein-rich clusters by oblique illumination microscopy (OIM) and dynamic light scattering (DLS). (a) A representative OIM image. The observed volume is ca. 120 × 80 × 5 μm^3. Clusters appear as green spots. (b) Number density distribution of the cluster sizes determined by OIM. The average of five determinations in distinct solution volumes is shown. The error bars represent the standard deviation. (c) Intensity correlation functions g_2 of the light scattered by a cluster-containing solution. The two shoulders of g_2 correspond to lysozyme monomers and clusters, respectively. g_2 is unchanged over 12 hours, indicating that the cluster population is steady. (d) The evolutions of the ratio of the correlation function amplitudes A_c/A_m, which characterizes the fraction of the protein held in the clusters, and the cluster radius R_c, evaluated from g_2 in (c). (e) The dependences of A_c/A_m and R_c on the protein concentration. The values of A_c/A_m and R_c in (d) and (e) represent averages of ten correlation functions; the error bars represent the standard deviation. In (a) – (d), lysozyme concentration was 60 mg ml^{-1}.

Perturbations of the protein structural integrity

Modeling of the interaction potential between native lysozyme molecules (complimenting an earlier theoretical estimate by McCammon and collaborators)[128-130] suggested that dimers or other oligomers of native lysozyme cannot support the formation of the observed mesoscopic clusters.[131] Experiments with moderate concentrations of urea and

ethanol[69, 112] and with solution shearing,[113] which destabilize the native conformation, and NMR analyses of cluster-containing and cluster-free solutions[69] indicate that partial protein unfolding is an integral part of the cluster mechanism. To differentiate the degree of unfolding required for cluster formation from that leading to amyloid fibrillation, we compared the cluster population to amyloid aggregates. To generate amyloid structures, we heated lysozyme solutions to 65, 80, and 90°C.[64, 106, 115, 116, 132-135] To constrain the amount of aggregated protein, we exposed the protein to an elevated temperature for only six minutes[64, 106, 115, 116].

Another aspect of the correlation between conformational flexibility and cluster formation is whether intramolecular S-S bridges are disrupted during the unfolding that leads to clusters [99-101, 115]. To elucidate this issue, we compare the behaviors of the mesoscopic clusters to aggregates induced by reducing the intramolecular S-S bonds using (tris(2-carboxyethyl)phosphine (TCEP). To evaluate the effects of varying levels of S-S bond disruption, we employ three concentrations of TCEP: 0.1, 0.2, and 0.4 mM. Unreacted TCEP was removed by buffer exchange prior to any additional characterization. We quantify the fraction of S-S bonds converted to sulfhydryl SH by comparing the reaction of the reduced protein with 5,5'-dithio-bis-(2-nitrobenzoic acid) (DTNB) to that of glutathione and L-cysteine, which contain one SH group per molecule. The highest fraction of disrupted S-S bonds, after treatment with 0.4 mM TCEP, is 9.8%, Figure 6.2a, suggesting that the reduction of more than one S-S bond per lysozyme molecule is unlikely. The two S-S bonds that appear exposed to the solution, the intra-α-domain C6-C127 and the inter-α-β-domain C76 – C94 [101], are indicated in Figure 6.2c. The steady fraction of broken S-S bonds, Figure 6.2b, reveals that the resulting SH groups do not rebind into intramolecular S-S bridges or form intermolecular S-S bonds. This observation suggests that the aggregates induced by S-S bond reduction assemble by non-covalent bonds. The enzymatic

activity of lysozyme is a sensitive indicator of the structural integrity of the active center of the molecule, located between the α and β domains, illustrated in Figure 6.2c.

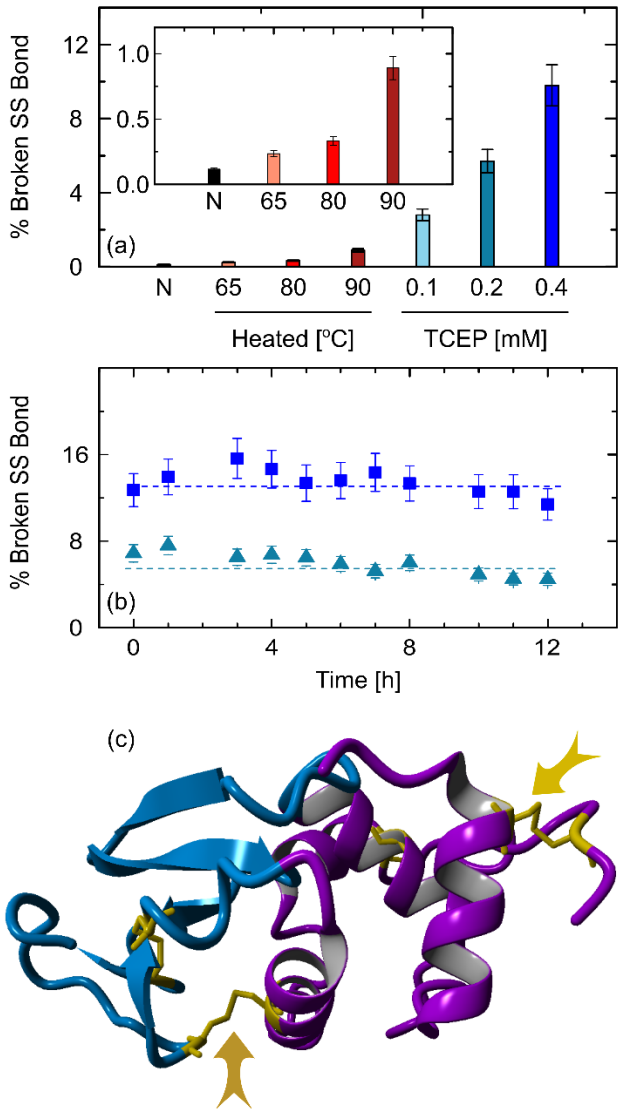

Figure 6.2. Perturbations of lysozyme structural integrity. (a) Quantification of the sulfhydryl, SH, groups using Elman's reagent, 5,5'-dithio-bis-(2-nitrobenzoic acid) (DTNB) in native solutions, N; solutions heated to temperatures shown on the abscissa; and in solutions treated with (tris(2-carboxyethyl)phosphine (TCEP) at concentrations shown in the abscissa. The average of three independent determinations is plotted; error bars represent the standard deviation. (b) Evolution of the sulfhydryl concentration in lysozyme solutions treated with 0.2 (triangles) and 0.4 (squares) mM TCEP measured after removing the unreacted TCEP by buffer exchange. (c) The structure of lysozyme drawn using by YASARA[136] and the PDB file 5L9J.[137] The α and β domains, identified as in McCammon, et al. are highlighted in purple and blue, respectively.

Lysozyme hydrolyzes a tetrasaccharide found in Gram-positive bacteria and breaks the glycosidic bond between n-acetylmuramic acid and n-acetylglucosamine [138]. We monitored the light absorbance of a bacterial suspension in the presence of native and treated lysozyme, Figure 7.2a,b. The active enzyme destroys the bacteria, clarifies the suspension, and lowers the absorbance. The activity of TCEP-treated lysozyme is similar, within the error of the determination, to that of the native protein, Figure 7.2a. This result is consistent with the low fraction of broken S-S bonds, Figure 6.2a, and may imply that TCEP reduces the intra-α-domain C6-C127 S-S bond, indicated with the downward arrow in Figure 6.2c, which has no direct role in the stability of the active center, located between the α and β domains.[139] Heating to 65°C for 6 min does not affect the activity of lysozyme, Figure 7.2b. The activity is significantly lowered after heating to 80°C. The steady optical density in the presence of lysozyme heated to 90°C suggests that exposure to this temperature completely destabilizes the active center in the majority of the molecules in the solution. The activity loss due to heating at increased temperature is consistent with previous observations of partial unfolding and fibrillation of lysozyme.[140] We tested the conformational integrity of heated and TCEP-treated lysozyme using the 1-anilino-8-naphthalenesulfonate (ANS) and Thioflavin T (ThT) assays. ANS is a fluorescent probe for the detection of partially unfolded states. ANS binds to hydrophobic sites of proteins, resulting in a blue shift of the fluorescence emission maximum and increase of the fluorescence intensity.[95, 141] ThT binds to β-sheet stacks common in amyloid structures and this binding enhances its fluorescence emission;[94] importantly, ThT is insensitive to lysozyme amyloid oligomers and only interacts with protofibrils and their more complex structures [132, 133, 142]. The fluorescent intensities in Figure 7.2d demonstrates that ANS binding to lysozyme heated to 65°C is indistinguishable from that of native lysozyme; heating to 80°C induces binding comparable to that of native lysozyme, indicating that few new hydrophobic sites were exposed to the solution

owing to these treatments. ANS strongly binds to lysozyme heated to 90°C, suggesting numerous exposed hydrophobic sites.

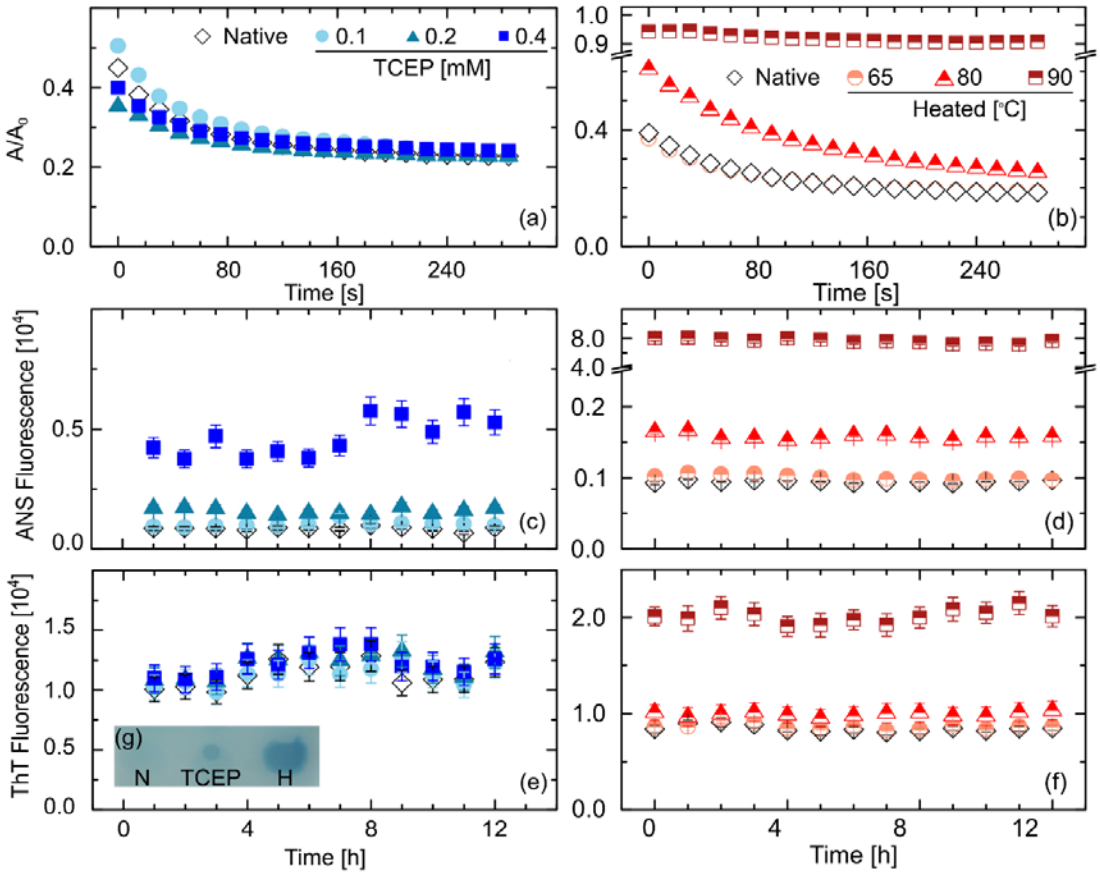

Figure 7.2. Characterization of the lysozyme structure perturbations. (a) and (b) Determination of lysozyme enzymatic activity in native and treated solutions. The absorbance A at 450 nm of a suspension of the bacterium Micrococcus lysodeikticus, relative to that in a suspension in the absence of lysozyme A_0, decreases as lysozyme degrades the bacteria. The slopes of the dependences characterize the enzyme activity. (a) In solutions treated with TCEP at concentrations shown in the legend. (b) In solutions heated to temperatures shown in the legend. (c) – (e) Tests of lysozyme conformational integrity after the treatments listed in (a) and (b) using 1-anilino-8-naphthalenesulfonate (ANS), in (c) and (d), and Thioflavin T (ThT) in (e) and (f). Fluorescence spectra of lysozyme solutions were recorded in the presence of the respective probe molecule upon excitation with 350 nm, in (c) and (d), and 442 nm, in (e) and (f). Both types of spectra exhibit maxima at about 490 nm. The evolution of the intensity at the maxima is plotted. The time evolutions in (a) – (e) were monitored in four solution samples and the average is plotted. The error bars represent the standard deviation. (g) Dot blot characterization of the binding of an amyloid-recognizing antibody to native (N), treated with 0.4 mM TCEP, and heated to 90°C (H) lysozyme.

The results on ANS binding in Figure 7.2c suggest that the degree of exposed hydrophobic patches after treatment with 0.4 mM TCEP is low; it is even lower for protein treated with 0.2 mM

TCEP. ANS binding to protein treated with 0.1 mM TCEP is comparable to that of native lysozyme. The results of the ThT assays in Figure 7.3e,f suggest that the amount of stacked β-sheets in the lysozyme treated with TCEP and heated to 65 and 80°C is similar to that in the native protein, whereas the lysozyme heated to 90°C presents abundant amyloid structures. Concomitantly, immunoblotting of native, TCEP-treated, and lysozyme heated to 90°C with an antibody that recognizes amyloid structures, Figure 7.2g, indicates no amyloid structures in the native protein, weak amyloid response in the TCEP-treated, and pronounced amyloid formation in the heated lysozyme. Collectively, the results in Figure 7.2 indicate that disruption of the S-S bonds by TCEP partially unfolds the protein. Limited exposure to 65°C does not affect the native protein structure, whereas heating to 80°C leads to partial unfolding that does not progress to amyloid fibrillation. Heating to 90°C causes the formation of amyloid structures. These responses are in agreement with expectations.[99-101, 106, 115, 140]

Distinct aggregation pathways of structurally modified lysozyme

The DLS correlation functions of heated and TCEP-treated solutions possess two shoulders, corresponding to the diffusion of monomers and aggregates, respectively, and similar to those of the native protein in Figure 5.2c. In solutions treated with 0.1 and 0.2 mM TCEP the monomer diffusivity D_m, determined from the characteristic diffusion time of the fast shoulder D_m, is similar to the native diffusivity and steady for 12 hours, Figure 8.2a,b. By contrast, in solutions exposed to 0.4 mM TCEP the diffusivity decreases over this time. Lower diffusivity could be an indication of intermolecular attraction. [112, 143, 144] Since the fraction of broken S-S bonds in this solution is steady over the tested period, Figure 6.2b, a slowly emerging attraction is hard to envision. With this, the decreasing D_m trend suggests the assembly of disordered oligomers of up to several molecules that capture a majority of the monomers in the solution.

In solutions heated to 65, 80 and 90°C, D_m is approximately steady over 12 hours, Figure 8.2b. After heating to 65 and 80°C, D_m is lower by ca. 5 and 15 %, respectively, than that of the native monomer. In combination with the weak ANS signal from hydrophobic interfaces, Figure 7.2d, and the lack of ThT evidence for amyloid aggregation in Figure 7.2e, the suppressed D_m suggests enhanced attraction between the lysozyme monomers after partial unfolding that exposes hydrophobic residues to the solvent.[112] In contrast to these mild effects, exposure to 90°C lowers D_m ca. 2.5-fold from the value in untreated solutions.

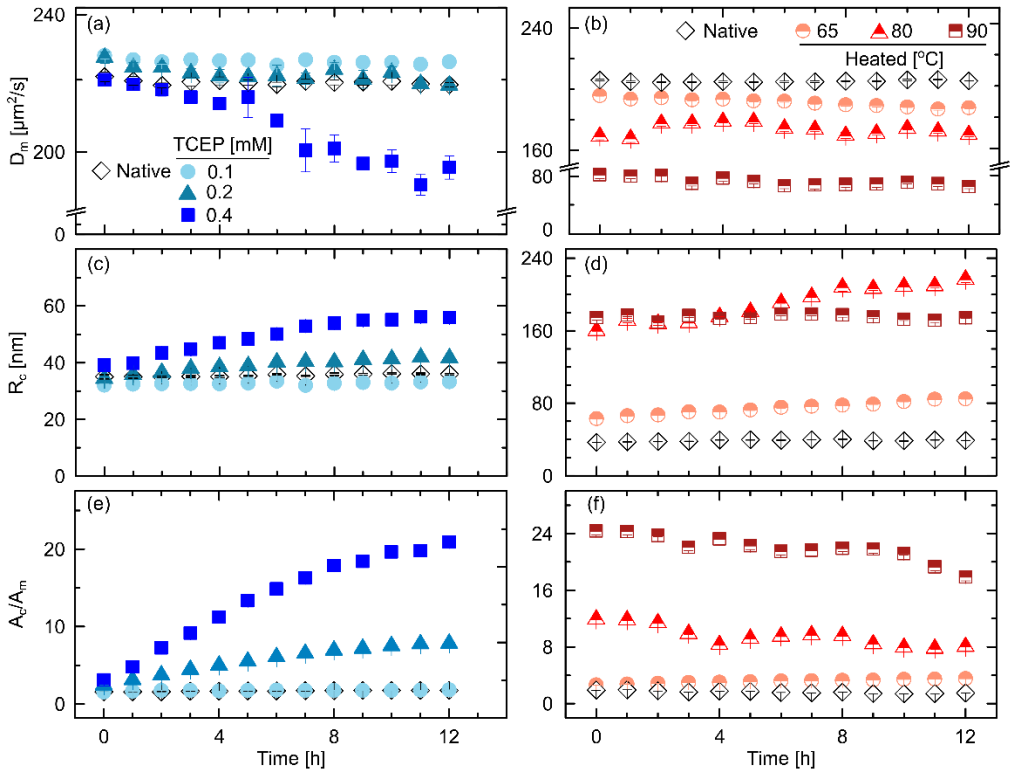

Figure 8.2. Condensates of native and treated lysozyme. (a) and (b) Diffusivity of lysozyme monomers D_m in native solutions and in solutions treated with TCEP at concentrations shown in the legend (a) and after heating for 6 min to temperature shown in the legend in (b). (c) and (d) Evolution of the radius R_c of clusters and aggregates detected by DLS after TCEP treatment and heating as in (a) and (b), respectively. (e) and (f) The ratio of the light scattering correlation function amplitudes A_c/A_m for solutions of TCEP-treated, in (e), and heated, in (f) lysozyme. The averages determined from ten correlation functions are plotted; the error bars represent the standard deviation.

The dramatically lower diffusivity of the protein exposed to 90°C and the strong ThT and ANS responses observed in Figure 7.2d,f indicate the assembly of the monomers into amyloid oligomers of ca. ten molecules.

The radius R_c of the clusters and aggregates existing in native and treated solutions, Figure 8.2c,d, is determined from the slow diffusion time D_c of the DLS correlation function. In solutions treated with 0.1 and 0.2 mM TCEP, the aggregates, which form immediately after solution preparation, are similar in size to the mesoscopic clusters of native lysozyme, Figure 8.2c. The aggregates formed in 0.4 mM TCEP solution are larger and capture ca. 2× higher fraction of the total protein, Figure 8.2e. Over time, the size of the aggregates in solutions treated with 0.2 and 0.4 mM TCEP increases, Figure 8.2c, in parallel with the increase of the fraction of aggregated protein, Figure 8.2e. The coupling of R_c and A_c/A_m and the time evolution of the condensate population in solutions with chemically modified protein are in sharp contrast with the respective behaviors of the mesoscopic clusters of native protein, revealed in Figure 5.2d,e. Solutions heated to 65°C exhibit aggregates with R_c somewhat higher than the clusters present in untreated solutions, Figure 8.2d. The A_c/A_m ratio, Figure 8.2f, reveals that the aggregates capture a fraction of the protein similar to that in untreated solutions. These comparisons suggest that the aggregates observed in solutions heated to 65°C represent mesoscopic clusters whose size is enhanced by the destabilization of a fraction of the monomers. The lack of amyloid structures in solutions heated to 80°C suggests that the heterogeneities detected in these solutions also represent mesoscopic clusters, whose larger size is due to the stronger protein unfolding. The clusters slowly grow, from 160 to 220 nm over 12 hours. The concomitant decrease in the fraction of protein captured in the clusters, represented by A_c/A_m, is weak (A_c/A_m is expected to scale with $(R_c/R_m)^3$),[118, 119] suggesting that this evolution represents Ostwald ripening of the clusters, which occurs faster than in previous observations[75] owing to destabilized protein conformation.

The amyloid aggregates, present in solutions heated to 90°C, are ca. 4× larger than the clusters of native lysozyme. Their size is steady over 12 hours. The steady decrease in the respective A_c/A_m ratio may be due to the formation of complex amyloid structures and their precipitation.[132] The discussed behaviors indicate persistence of cluster formation, typical of native protein solutions, after short-term exposure to 65 and 80°C, and amyloid aggregation that requires heating to 90°C. This conclusion is consistent with the preservation of intact lysozyme α helices upon heating close to the protein melting temperature (extrapolating the pH dependence of the lysozyme melting temperature[140] to pH 7.8 of our tests suggests that it is between 80 and 90°C), followed by drastic structure destabilization within additional 10°C[140].

The values of R_c and A_c/A_m for native protein in Figure 8.2c,d are similar to those for solutions treated with 0.1 and 0.2 mM TCEP even though the latter two solutions contain ca. 3 and 6%, respectively, broken intramolecular S-S bonds. The lack of correlation between the broken S-S bonds and the cluster properties suggests that broken S-S bonds, present in 0.2% of the native protein, Figure 6.2b, are not necessary for cluster formation.[113] The evolution of R_m, and A_c/A_m in lysozyme solutions treated with 0.2 and 0.4 mM TCEP in Figure 8.2c,d suggests the growth of a population of disordered aggregates of chemically modified lysozyme, or the incorporation of disordered oligomers in the mesoscopic clusters, which increases the cluster size and stabilizes the cluster population. Both scenarios utilize the disordered oligomers, evidenced by the decreasing D_m in Figure 8.2a, and are compatible with the results of the ANS assays for partial unfolding in Figure 7.2c.

To assess the applicability of these scenarios, we tested the reversibility of aggregation of structurally modified lysozyme by monitoring the dependence of A_c/A_m on the protein concentration. We prepared a solution of 60 mg ml^{-1} and diluted with buffer down to 20 mg ml^{-1}.

We mimicked irreversibly aggregated lysozyme by suspending latex particles with radius 100 nm in a lysozyme solution. Diluting this suspension with buffer lowers the concentration of both particles and protein and keeps the ratio A_c/A_m constant, Figure 9.2a. The fraction of the protein captured in amyloid aggregates decreases significantly upon dilution, Figure 9.2b, reflecting the reversibility of small amyloid aggregates, seen with several proteins.[145] The A_c/A_m trend for lysozyme freshly treated with 0.2 mM TCEP indicates that these condensates are reversible, Figure 9.2c. The observed reversibility implies that the disordered oligomers do not form a separate population of aggregates (aggregation of lysozyme with broken S-S bonds is expected to be irreversible,[99-101, 115]), but rather incorporate into the mesoscopic clusters, where they lead to greater cluster size and higher total volume of the cluster population.

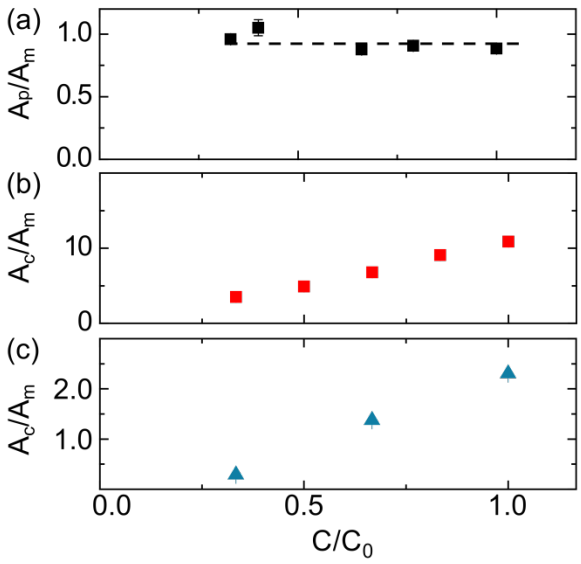

Figure 9.2. Reversibility of the aggregates formed in heated and TCEP-treated solutions. (a) The ratio A_p/A_m of the amplitudes of the DLS correlation function g_2 from a suspension of latex particles of radius R_p = 100 nm in a lysozyme solution with $C_{m,0}$ = 60 mg ml^{-1} as a function of particle concentration. The initial particle concertation $C_{p,0}$ corresponds to volume fraction $\varphi_0 = 4 \times 10^{-6}$. A solution with $C_{p,0}$ and $C_{m,0}$ was diluted with 20 mM HEPES buffer so that the ratio C_p/C_m remained constant. (b) and (c) The dependence of the ratio A_c/A_m on the protein concentration for solutions heated to 90°C, in (b), and for solutions treated with 0.2 mM TCEP, in (c). C_0 = 60 mg ml^{-1} in both (b) and (c). The averages determined from ten correlation functions are plotted; the error bars represent the standard deviation.

Aggregation of chemically modified lysozyme

The evolution of the aggregates in solutions with a higher fraction of broken S-S bonds, induced by treatment with 0.4 mM TCEP in Figure 8.2c,d, diverges from that in the other tested solutions. For additional evidence for an alternative aggregation mechanism in solutions with high concentration of chemically modified molecules, we explore the cluster size distribution determined by OIM. The data in Figure 10.2 demonstrate that in solution of native lysozyme, the cluster population 12 hours after solution preparation is practically identical to that in freshly prepared solutions. This observation agrees with the data in Figure 5.2c,d. The average radius of clusters in solutions freshly treated with TCEP is slightly greater than in native solutions, and the cluster concentration is higher by ca. 50%, Figure 10.3e, consistent with the observations in Figure 8.2c,d. Importantly, after 12 hours, the TCEP-treated solution exhibits a second population of aggregates with radius ca. 90 nm, which exists in parallel with the mesoscopic clusters present in both native and TCEP-treated solutions, Figure 10.2d and e. The second population of condensates might be a product of the aggregation of the disordered oligomers, reflected in the decreasing D_m trend in Figure 8.2a. We tested the reversibility of aggregation in solutions kept in the presence of 0.4 mM TCEP for 12 hours. For this, we prepared a 60 mg ml^{-1} lysozyme solution, applied TCEP, and stored the solution at 22°C for 12 hours. We divided this solution into three aliquots that were undiluted and diluted to two final concentrations: 40 and 20 mg ml^{-1}. DLS correlation functions indicate that R_c and A_c/A_m, Figure 11.2, are larger than in solutions of native protein, Figure 5.3e, consistent with observations in Figures 8.2 and 10.2. R_c is independent and A_c/A_m is a weak function of the dilution ratio, suggesting a weak reversibility of the condensates. The weak reversibility is consistent with the presence of two populations of aggregates, revealed by the OIM size distributions in Figure 10.2e. Disordered aggregates formed entirely of chemically

modified protein are expected to be irreversible; [99-101]however, these aggregates constitute only a fraction of the condensates seen in Figure 8.2d,e.

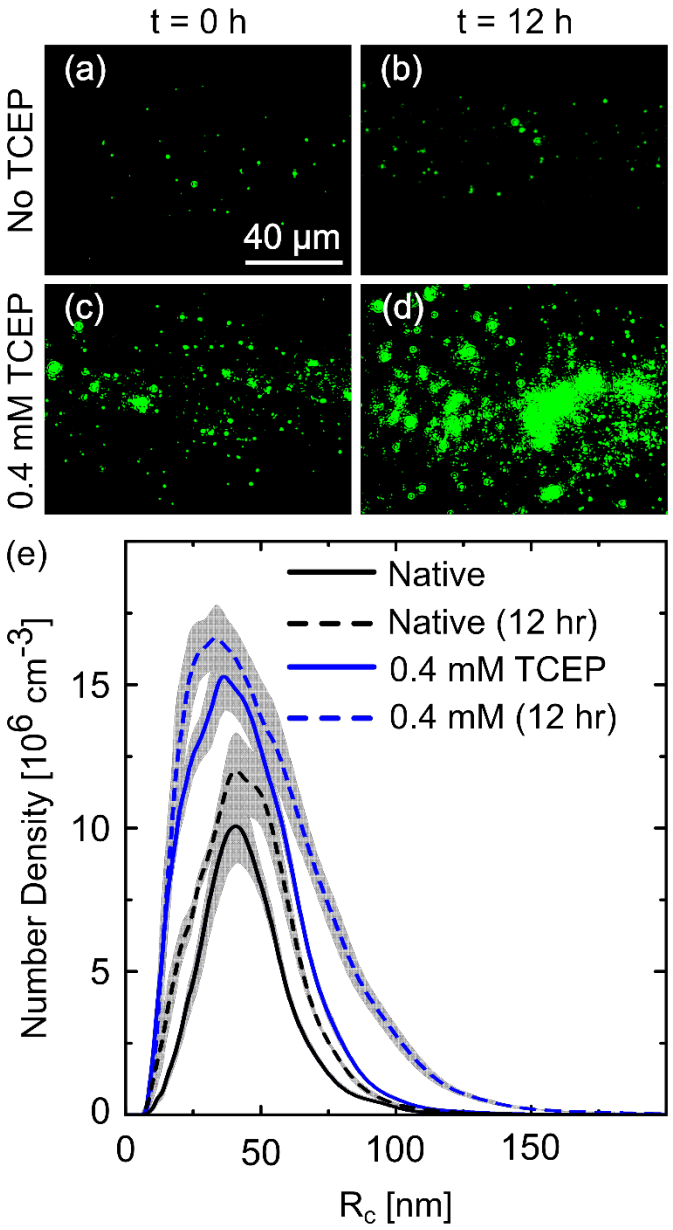

Figure 10.2. The evolution of aggregates in TCEP-treated solutions. (a) – (d) Representative OIM images from native lysozyme solutions and from solutions treated with 0.4 mM TCEP, shortly after preparation and after 12 hours. Clusters appear as green spots. The observed volume is approximately 120 × 80 × 5 µm^3. Lysozyme concentration is 60 mg ml^{-1} in all panels. (e) Number density distributions of the cluster sizes determined by OIM in the four solutions represented in (a) – (d). The average of five determinations in distinct solution volumes is shown; the error bars represent the standard deviation.

It appears that the population of mesoscopic clusters, preserved in these solutions after aging in the presence of TCEP, has retained its reversibility. Collectively, the observations in Figures 6.2 – 9.2 suggest that disordered chains of chemically modified protein form oligomers in the solution that may invade the mesoscopic clusters or assemble into distinct condensates, existing in parallel with the mesoscopic clusters. The disordered oligomers embedded in the clusters modify their properties, but do not affect the cluster reversibility; condensates assembled from oligomers are likely irreversible.

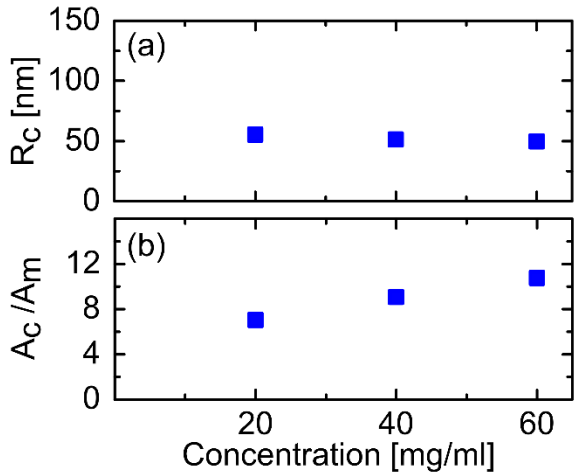

Figure 11.2. Weak reversibility of aggregates formed in solutions treated with 0.4 mM TCEP and aged for 12 hours. (a) The dependence of the aggregate radius R_c in solutions treated with 0.4 mM TCEP on the lysozyme concentration obtained by dilution of the highest concentration sample after incubation for 12 hours at 22°C. (b) The corresponding dependences of the ratio A_c/A_m. The averages determined from ten correlation functions are plotted; the error bars representing the standard deviation are smaller than the symbol size.

Summary

The results presented here demonstrate that three distinct condensate polymorphs may self-assemble in lysozyme solutions. The selection of condensation pathway is guided by the environmental stress: mesoscopic protein-rich clusters exist at typical laboratory conditions and in solutions heated to 65 or 80°C; heating to 90°C for a limited time induces amyloid fibrillation, whereas reduction potential breaks the intramolecular S-S bonds and leads to disordered aggregates. The mesoscopic protein-rich clusters represent a unique class of condensate: their

radius is steady for 12 hours at ca. 40 nm, whereas the amyloid structures are as large as 180 nm and the disordered aggregates grow to 60 nm. Another signature behavior of the mesoscopic clusters is that the cluster radius is decoupled from the fraction of protein captured in the clusters.

We show that the partial unfolding of a small fraction of the lysozyme molecules, a necessary precursor for the formation of mesoscopic clusters,[69, 112, 113] differs from the unfolding of a large population of molecules leading to amyloid fibrils. This observation supports the notion that the mesoscopic clusters require opening of the hinge between the α and β domains of lysozyme,[69, 112, 113] whereas fibrillation is preceded by destabilization of the α helices[115, 146, 147]. In accordance with this molecular viewpoint, the enzymatic activity of lysozyme is fully retained in cluster forming solutions, but the protein that assembles into amyloid structures is inactive. Furthermore, we show that breaking of the intramolecular S-S bonds, which are essential for the structural integrity of lysozyme, [99-101, 115] is not a prerequisite for cluster formation.

The formation of mesoscopic clusters of lysozyme is reversible and the fraction of protein captured in them adjusts to variation of the concentration of the host solution. The clusters may capture a low concentration of disordered oligomers. High amounts of chemically modified protein, however, assemble into irreversible disordered aggregates that exist in parallel with the mesoscopic clusters.

Chapter 3 Non-classical nucleation of tumor suppressor p53 fibrils hosted by mesoscopic protein-rich clusters

Introduction

The aggregation of proteins into ordered arrays of native or partially unfolded chains has been associates with conditions such as sickle cell, Alzheimer's, diabetes mellitus 2, among others, comprising the growing class of aggregation diseases [148-150]. The transcription factor p53, one of the most important tumor suppressors, transforms after mutation into a powerful oncogene, which blocks the anti-cancer activity of wild-type p53, its paralogs p63 and p73, and several distinct pathways [151, 152], [50]. Several mechanisms of the gain of oncogenic function (GOF) of mutant p53 have been put forth. A subsection of the malignant mutations destabilize the p53 conformation. The associated enhanced aggregation of the mutant and co-aggregation with wild-type p53 and its paralogues represent a potent GOF mechanism, which defines cancer, in certain respect, as an aggregation-related disease. Importantly, fibril suppression, for instance, by stabilization of the mutant p53 conformation, has been identified as a general way to fight cancer [151, 153]. The aggregation of mutant and wild-type p53, *in vitro* and *in vivo*, exhibits features typical of β-amyloid fibrillation. The amyloid domains bind to Thioflavin T (ThT), a die that recognizes β-aggregates and emits fluorescence only when bound, and the fluorescent intensity increases following a typical sigmoid curve [52, 59, 154-158]. In the sigmoid correlation, an initial period of insignificant signal increase is followed by exponential gain and, finally, by saturation [154, 159]. The three periods correspond, respectively, to the nucleation of fibrillar domains that are still small and produce negligible signal, continued nucleation and growth of the nucleated domains, and depletion of the soluble protein to the solubility, whereupon fibrillar growth ceases.

The observations on p53 fibrillation have provoked questions on the relevant molecular mechanisms. Notably, the concentration independence of the parameters of the sigmoid curve

and the short initial time period have suggested that a non-classical mechanism of fibril nucleation and growth operates [154, 155]. Furthermore, tests of whether mutant p53 fibrils cross seed wild-type aggregation have produced both positive and negative outcomes [52, 59, 156]. Whereas it is clear how mutations that destabilize p53 conformation incite aggregation, the enhanced fibril formation of mutants at the DNA binding sites, which retain their conformational stability, is a mystery [59, 151]. Additional open questions relate to the significance of intracellular crowding for the kinetics of fibril nucleation and growth and the similarity and differences between fibrils of wild-type and mutant p53. To address these questions, we explore the aggregation of wild-type p53 at near physiological conditions and in crowded environments. Besides serving as a reference for mutant p53 behaviors, aggregation of wild-type p53 is of interest because it may, under certain conditions, behave like mutant p53 [50]. Wild-type p53 has been detected in a mutant conformation in hypoxic cells [160] and after binding to a common p53 regulator protein, MDM2 [161].

Material and methods

TCEP (tris(2-carboxyethyl)phosphine, 8-Anilinonaphthalene-1-sulfonic acid (ANS), Thioflavin T (ThT), Ficoll PM-70, and Fluorescein are purchased from Sigma Aldrich. EDAC N-(3-Dimethylaminopropyl)-N'-ethylcarbodiimide hydrochloride and BODIPY-530/550 NHS ester are purchased from Thermo Fisher Scientific. For wild type p53, plasmid pET15b-TP53 containing N-terminal 6–his–WT–p53 (1–393) is purchased from Addgene [162].

Protein expression Plasmid pET15b-TP53, obtained from Addgene was transformed into *E. coli* BL21 (DE3). A single colony of the fresh transformants was inoculated into 10 mL media containing 20 g L^{-1} Bacto-trypton, 10 g L^{-1} yeast extract, 5 g L^{-1} NaCl, and 100 µg mL^{-1} ampicillin. The culture was let grown for 5 hours and the seed culture was then diluted to 1 liter of the same media with a factor of 100. When OD_{600} of the subculture reached 0.4–0.5, cells were cold-

shocked on ice for 25 minutes followed by inducing by 0.1 mM IPTG (β-D-1-thiogalactopyranoside) and 0.2 mM $ZnCl_2$, and the culture was let grown at 20 °C at 250 rpm for overnight [162-165].

The cells were pelleted and re-suspended in 100 mM KH_2PO_4/K_2HPO_4 (pH = 8.0), 300 mM NaCl, 5% glycerol, 2 mM TCEP (2 mL per 1 g of wet cells) to a final volume of 40 mL. 1 mL of 10x EDTA free-protease inhibitor cocktail (SIGMA FAST protease inhibitor tablets) is added to the cell suspension. The suspension was then aliquoted into 4 mL fractions in 5 mL Eppendorf tubes for sonication to lyse the cells. Each aliquot was thrice sonicated using a Q-SONICA MISONIX XL-2000 (11 watt output) for 30 seconds on ice with 15 min intervals between sonications. The lysate was then centrifuged at 5000 rpm for 1 hour to pellet the cell mass. The supernatant was filtered with 0.45 µm SFCA syringe filters prior to purification. It is worth mentioning that lysing procedure using DNAse and lysozyme (chemical lysing), although more expensive, might be more beneficial than sonication lysing. The outcome would be p53 with higher purity, since sonication can result in formation of a small fragment around 20kDa which gets co-purified with p53., however chemical lysing requires thrice freeze and thawed at −20 °C for at least 1 hour prior to addition of any lysozyme and DNAse.

Protein purification For purification, Ni Sepharose™ 6 Fast Flow column was equilibrated with 100 mM KH_2PO_4/K_2HPO_4 (pH = 8.0), 300 mM NaCl, 5% glycerol, 2 mM TCEP, and 25 mM imidazole. Bound p53 was eluted with a linear gradient of imidazole (0.7 CV, the cheaper imidazole from Sigma Aldrich is the oxidized state of imidazole and it generates absorbance of ~300 mAU/500 mM imidazole, thus it is essential to elute the p53 with sharp imidazole gradient from Ni-NTA resin ~ 0.7-0.8 CV or follow p53—hist on AKTA). Fractions containing p53 were diluted 1:1 with 20 mM KH_2PO_4/K_2HPO_4 (pH = 6.50), 5 % glycerol, and 5 mM TCEP for further binding to HiTrap™ Heparin HP column and the bound p53 was eluted with linear gradient of NaCl (15 CV gradient of

2M NaCl. The AKTA UNICORN 7 (HPLC software) was programmed to collect the maxima of the eluted peak (or follow p53-heparin program). In vitro expression and Ni-NTA purification could likely result in formation of different charge states of p53, which potentially alter the folding state from native structure). The purified p53 was further buffer exchanged using GE healthcare PD-10 desalting columns to 50 mM Tris (pH = 7.85), 150 mM NaCl, 5 mM TCEP, and 10% glycerol for storage and experiments. Buffer exchanged p53 was flash frozen in liquid nitrogen and stored in aliquots of ~15 µM as stock in −80 °C. Yield of soluble p53 with final purity of ~85% after all steps was about ~1.5 mg per 1 L of medium[163]. It is worth mentioning that extra 6-hist tag could get cleaved using thrombin, however, due the cost of this process it was not performed in these experiment. Hist-tag cleaved p53 can further be purified following dilution with KHP buffer, loading into Heparin resin and elution with 2 M NaCl.

Characterization of solubility of p53 For solubility measurements without Ficoll, frozen aliquots were thawed on ice. Thawed protein and incubation buffer (50 mM Tris (pH = 7.85), 150 mM NaCl, 5 mM TCEP, 10% glycerol) were filtered with 0.22 µm Polyethersulfone (PES) syringe filters prior to all measurements. The concentration of stock p53 solution was determined by absorbance measurements using a Beckman Coulter Du 800 spectrophotometer and extinction coefficient ε = 0.763 mL $mg^{-1}cm^{-1}$ at 280 nm [93, 163]. After filtration, the concentration of the stock p53 solution was ~12 µM. Independent solutions of p53 with concentrations of 0.6 – 8.2 µM were prepared at 7 °C by serially diluting the p53 stock solution with the incubation buffer. Diluted samples were then incubated at 15 and 37 °C for at least 4 hours. After incubation, samples were filtered with 0.22 µm PES syringe filters to eliminate any formed aggregate and p53 concentration was determined spectrophotometrically. For measurements of the solubility of p53 in a crowded, Ficoll-rich environment, independent solutions of p53 with concentrations of 0.6 – 7.7 µM were prepared at 7 °C by serially diluting the stock solution with the incubation buffer and a stock Ficoll

solution of concentration 250 mg mL^{-1} containing 200 mM KCl in DI-water to set the Ficoll concentration at 56 mg mL^{-1} while keeping the ionic strength at physiological conditions in all samples. Prepared samples were incubated at 15 and 37 °C for 4 hours and filtered with 0.22 µm PES filters prior to concentration determination.

Dynamic light scattering (DLS) DLS data were collected with an ALV goniometer equipped with a He-Ne laser (wavelength λ = 632.8 nm) and an ALV-5000/EPP Multiple tau Digital Correlator (ALV-GmbH, Langen, Germany).

Low-temperature measurements: p53 monomers and oligomers. The normalized intensity-intensity correlation functions $g_2(q,\tau)$ 45 seconds each, recorded for up to four hours of incubation at T = 15°C with fixed scattering angle of 90°, all possess one polydisperse shoulder, indicating the presence of oligomeric species of similar sizes (Fig. 12.3) [43, 166]. We determine the characteristic diffusion time τ and polydispersity index $\mu\,\tau^2$ of the p53 solution at a concentration of 6 µM by fitting the normalized correlation function with a polydisperse exponent fit [167], $g_2(q,\tau) - 1 = \left(A\exp\left(-{}^{t}/_{\tau}\right)\left(1+\mu\frac{t^2}{2}\right)\right)^2 + \varepsilon(\tau)$, (1.3), where *A* is the scattering amplitude, which is proportional to the intensity scattered by the oligomeric species in the solution, and $\varepsilon(\tau)$ accounts for mechanical, optical, and electronic noise in the signal[109, 111]. In our measurements, ε was one or two orders of magnitude lower than the *A* values. We used τ and μ to determine the average diffusivity and dispersity, *D* and PDI, from $D = (q^2\tau)^{-1}$ and $\mathrm{PDI} = \mu\tau^2$, where $q = \frac{4\pi n}{\lambda}\sin(\theta/2)$ is the wave vector at a scattering angle of 90°, λ = 632.8 nm is the wavelength of the incident red laser and *n = 1.33* is the solution refractive index [112], [113].

Higher-temperature measurements: p53 monomers and fibrils. To test the reversibility of the fibrils (Fig. 15.3F), the p53 solution with concentration of 1.5 µM was incubated at T =37 °C for four hours. The stock solution was then tested with dynamic light scattering for co-existence

of monomer and fibrillar aggregates. To test the reversibility of the fibrillar aggregates, the stock was further diluted into incubation buffer (50 mM Tris, 150 mM NaCl, 5 mM TCEP, 10% glycerol, pH = 7.85) respectively to 1.3 and 0.9 μM and 45 seconds intensity correlation functions were collected using DLS [113, 168]. We determined the characteristic diffusion times τ_m and τ_c of the monomers and clusters from the two distinct shoulders of the normalized correlation function by fitting with a squared sum of exponentials [74, 167], $g_2(q,\tau) - 1 = \left(A_m \exp\left(-{}^{t}/_{\tau_m}\right)(1 + \mu_m \frac{t^2}{2}) + A_c \exp\left(-{}^{t}/_{\tau_c}\right)\right)^2 + \varepsilon(\tau)$, (2.3). The data was fitted with $\tau > 10^{-5}$ s because the incubation buffer at 37°C generates small background for time scales smaller than this threshold. A_m and A_c are the respective amplitudes, which are proportional to the intensity scattered by the monomers and clusters, and $\varepsilon(\tau)$ accounts for mechanical, optical, and electronic noise in the signal[109, 111]. We used τ_m and τ_c to determine the monomer and cluster diffusivities, D_m and D_c, from $D_m = (q^2\tau_m)^{-1}$ and $D_c = (q^2\tau_c)^{-1}$, where $q = \frac{4\pi n}{\lambda}\sin(\theta/2)$ is the scattering wave vector at 90°.

From the characteristic time scales τ we computed the average size R of monomers and clusters from the Stokes-Einstein relation, $R_i = \frac{k_B T}{6\pi\eta_i D}$ [169]. Here T, k_B, and η_i are respectively the temperature, Boltzmann constant, and the viscosity of the buffer solution. The buffer viscosity η_i was determined from the dynamics of Fluoro-Max Dyed Red Fluorescent polystyrene spheres, with diameter $2R_p = 2$ μm, diffusing in the buffer solution and characterized by DLS [74]. Viscosities of the buffer with 10% glycerol without Ficoll at T = 15 and 37 °C were $\eta_i = 1.50 \pm 0.05$ and $\eta_i = 0.95 \pm 0.03$ mPa·s, respectively.

Cluster characterization by oblique illumination microscopy (OIM) Movies were acquired over 30 seconds unless mentioned otherwise. We found that objects recorded for times shorter

than 1 s were interference spots from two or more clusters tracked for significantly longer times. This observation is supported by the estimate that a cluster with diffusivity $D_2 \approx 10^{-12}$ m^2s^{-1} would be detectable in a focal plane with depth 5 μm for about 25 s. We did not consider them as parts of the cluster population in the determination of the cluster parameters.

Effect of temperature on p53 aggregation: To monitor the aggregation of p53 as a function of temperature by OIM (Fig. 12.3), a stock p53 solution was diluted to 2.2 μM and filtered with 0.22 μm PES prior to measurement. The protein solution was incubated for 10 minutes at temperatures of 15, 18, 25, 37, and 42 °C. Five distinct movies per each temperature were collected to characterize aggregation of the protein after incubation. We evaluated the average size of the clusters using the Stokes-Einstein equation, $R_i = \frac{k_B T}{6\pi\eta_i D}$ [170], where T is the experiment temperature varying from 15 to 42 °C, k_B and η_i are respectively the Boltzmann constant and the viscosity of the buffer solution at the experiment temperature measured as discussed in DLS section. It is worth mentioning that p53 solutions are extremely sensitive to temperature and the Nano sight laser warms up the sample rapidly, thus these experiments are performed with minimal waste of time. Another issue to consider is the crash of the Nano sight camera, which occurs during heavy data collections, thus it is essential to assert movies are properly collected.

Effect of crowding on p53 clustering: To characterize clustering of p53 at T =15 °C (Fig. 13.3), two variables were selected. To probe the effect of Ficoll concentration on clustering of p53, the Ficoll concentration was varied from $0 - 90$ mg mL^{-1} while holding the concentration of p53 fixed at 1.2 μM. It is necessary to prepare fresh Ficoll solutions. For this purpose, Ficoll solution at 100 mg/ml Ficoll with 200 mM KCl (to keep the ionic strength constant) was prepared over night with mild rotation. Before performing any experiment on p53 clusters, it is essential to test if the

Ficoll stock solution is homogeneous. To probe the effect of p53 concentration, the Ficoll concentration was set at 90 mg mL^{-1} and the p53 concentration was varied from 0.3 – 2.3 μM.

Ostwald ripening of p53 clusters: To test the Ostwald ripening of p53-rich clusters at T =15 °C (Fig. 14.3), the p53 and Ficoll concentrations were fixed at 1.2 μM and 56 mg mL^{-1} and five distinct movies were collected at times 5, 10, 30, 60, 90, 120, and 150 minutes after preparation of each sample. The average size of the clusters were calculated using the Stokes-Einstein equation, $R_i = \frac{k_B T}{6\pi\eta_i D}$ [170], where T = 288.15 K for all cluster experiments in presence of the Ficoll as crowder and η_i (viscosity of the solution in presence of Ficoll) measured as discussed in DLS section.

Incorporation of Ficoll into p53 mesoscopic clusters: To determine if p53-rich clusters contain Ficoll inside (Fig. 13.3), p53 solution at concentration of 1.2 μM was prepared in presence of 15 mg mL^{-1} BODIPY-labeled Ficoll and 41 mg mL^{-1} un-labeled Ficoll. This solution was incubated at 15°C in Nanosight cuvette for two hours. First, a movie of 10 seconds was collected without any filter cube in the optical path. Within 1 minute after the end of the collected movie, the fluorescence filter cube was inserted into the optical path and a fluorescence movie was collected for 10 seconds. Assuming diffusion coefficient of D = 1 $\mu m^2\ s^{-1}$ for clusters in presence of Ficoll, the approximate displacement of the clusters is < 6 μm ($\Delta x = \sqrt{Dt/\eta}$), thus the approximate position of clusters remained constant over the experiment. To confirm that fluorescence was due to incorporation of labeled Ficoll into p53 clusters, the control sample was tested for fluorescence with same Ficoll composition without any p53.

Fluorescence labeling of Ficoll Ficoll PM70 was activated with chloroacetate at pH>13 for four hours. 0.45 g Ficoll was dissolved in 5 ml water. Chloroacetate was added to concentration of 2M with further addition of 1.6 g NaOH to set pH >13. Reaction was carried out

at T = 60 °C (this value corresponds to T = 90°C of the hot plate) with 250 rpm. The reaction is stopped by dropping the pH to ~6 and dialysis was initiated overnight followed by 10k Amicon filtration to eliminate any residual of small molecules and concentrate the Ficoll to ~1mL. For addition of amine group to the activated Ficoll, 500 µl 65% hydrazine (~2M) is added to the mixture and pH is set to ~4.5 followed by addition of ~50 mg EDAC (N-(3-Dimethylaminopropyl)-N'-ethylcarbodiimide hydrochloride) to initiate the reaction. The reaction was carried out at T = 50°C (this corresponds to T = 75°C of the hot plate) with constant agitation at 250 rpm and monitoring the pH every 20 minutes. Amine-activated Ficoll was then buffer exchanged overnight followed by 10k Amicon filtration to final volume of ~ 1 ml [171, 172]. Amine activated Ficoll was then reacted with ~0.15 g Fluorescein in presence of ~ 50 mg EDAC to generate fluorescein-labeled Ficoll. Reaction was carried out for 4 hours at T = 50°C with 250 rpm mixing with pH ~4.5. After reaction, filtration with 0.2 µm PTFE is essential prior to dialysis to eliminate the large dye aggregates. Dialysis was carried out against 2 L DI-water for one week with constant exchange of the water per day to speed up dialysis. The dialysate was concentrated using 10k Amicon centrifuge filters followed by an extra buffer exchange step using a desalting PD-10 column to eliminate any residual free dye. The eluted Ficoll was concentrated to 100 mg mL^{-1} using an Amicon 10k filter followed by centrifugation for 20 minutes at 14000 rpm and further filtration with 0.2 µm PTFE (Polytetrafluoroethylene) syringe filters. An extinction coefficient of 2.00 ± 0.12 × 10^{-3} mL mg^{-1} cm^{-1} at 280 nm was used for determination of Ficoll concentration, which was calculated independently by measuring absorbance of duplicate solutions of 164 mg mL^{-1} of un-labeled Ficoll solution and ratio of 1.7 for the $A_{475\ nm}/A_{280\ nm}$ of fluorescein is used to subtract the dye background. The absorbance ratio of the dye at 475 nm to 280 nm was measured spectrophotometrically in independent measurements. To determine whether Ficoll incorporated into p53 fibrils, the p53 concentration was set at 7.7 µM in presence of 56 mg mL^{-1}

fluorescein-labelled Ficoll and the solution was incubated at T =37 °C over 12 hours to form large aggregates. Control sample was prepared with same content of labeled Ficoll without p53. 10 µL of samples were placed on a large cover slip (48 mm × 65 mm, Fisherbrand), covered with a smaller cover slip (22 mm × 22 mm, Fisherbrand), and placed on the stage of epi-fluorescence microscope (Leica DM 3000B) equipped with a 40× objective lens (NA. 0.65). Images were collected using a sCMOS camera (pco.edge 4.2, field of view 212.5 × 213.3) from four distinct locations of the samples under excitation wavelength of 488 nm[173]. Representative micrographs of control and p53 sample are shown in Fig. 15.3C–D. For incorporation of Ficoll into clusters, the amine activated Ficoll solution was reacted with NHS-ester BODIPY/530 in 0.2 M $NaHCO_3$ at pH = 8.3 (to have the right buffer capacity and pH, 0.4 M $NaHCO_3$ at pH = 8.3 was prepared as stock and it was diluted 1:1 with Ficoll solution) overnight in a dark Eppendorf tube in a water bath at T = 25°C with constant agitation (~350 rpm). BODIPY labeled-Ficoll under was buffer exchanged and concentrated as mentioned above to final concentration of 30 mg mL^{-1} Ficoll.

Static light scattering to measure p53-p53 interactions Osmotic compressibility was measured with the ALV instrument (reference DLS section). We measured the scattered intensity of the p53 solutions with protein concentration varying from 0.12 – 0.4 mg mL^{-1} in the incubation buffer (pH = 7.85; 50 mM Tris, 150 mM NaCl, 10% glycerol, and 5 mM TCEP). The average molecular weight $M(w)$ and the second virial coefficient B_{22} can be calculated from the plot of KC/R as a function of p53 concentration following the equation[72, 174], $\frac{KC}{R} = M(w) + 2B_{22}C$ (3.3). Here $R = I_\theta/I_0$ is the Rayleigh ratio of scattered light to incident; K is system constant defined as $K = N_A^{-1}\left(\frac{2\pi n}{\lambda^2}\right)^2\left(\frac{dn}{dc}\right)^2$,[174] where $n = 1.33$ is the refractive index of the solvent and $dn/dc = 0.20$ is the first derivative of the refractive index with respect to protein

concentration measured using a Brookhaven instrument differential refractometer operating at a wavelength of 620 nm[72].

ThT and ANS assay for characterization of p53 aggregation kinetics The aggregation kinetics of p53 was measured at T = 37 °C using a 1-anilino-8-naphthalenesulfonate (ANS) assay, which enables detection of small oligomeric species forming due to partial unfolding of hydrophobic core of the proteins during the lag phase of protein aggregation[95, 106, 175]. ANS was dissolved at 4 mM in incubation buffer (50 mM Tris, 150 mM NaCl, 5 mM TCEP, 10 % glycerol; pH = 7.85). The solution was filtered through a 0.2 µm Teflon filter. The ANS concentration was determined spectrophotometrically using extinction coefficient 18 mM^{-1} cm^{-1} at 270 nm[95]. 10 µL of this solution were added to 200 µL of the tested p53 solutions at final concentration of 6.5 ± 0.5 µM prepared by addition of 116 µL of 12.0 ± 0.5 µM stock p53 to 0, 24, 47, and 84 µL of stock Ficoll solution at 250 mg mL^{-1} diluted respectively with 84, 60, 37, and 0 µL of incubation buffer (50 mM Tris, 150 mM NaCl, 5 mM TCEP, 10% glycerol, pH = 7.85) to a total volume of 200 µL. For experimental statistics, two identical samples of each solution mixture were loaded in a 96-well plate and the fluorescence response to excitation at 350 nm was recorded at an emission wavelength of 500 nm by an Infinite 200 PRO microplate reader (Tecan) at 10 minute intervals over six hours. To test the fibrillar nature of the aggregates, ThT was dissolved at 5 mM in incubation buffer (50 mM Tris, 150 mM NaCl, 5 mM TCEP, 10% glycerol, pH = 7.85). The ThT concentration was determined spectrophotometrically using extinction coefficient 26.6 $mM^{-1}cm^{-1}$ at 416 nm[94-96]. The p53 solution at concentration of 7.7 µM was incubated with 0 and 56 mg mL^{-1} Ficoll at T = 37 °C for 12 hours to form large aggregates. The aggregates were then pelleted using centrifugation at 14,000 rpm for 20 minutes. The pellet was re-suspended in 100 µL of the incubation buffer and 1 µL of stock ThT solution was added to the suspension. After 20 minutes

of incubation, 10 μL of samples were imaged and representative images are shown in Fig. 15.3A–B[173].

Temperature promotes p53 aggregation

We monitored the aggregation of p53 as a function of temperature using oblique illumination microscopy (OIM) [109, 111]. This method enables the detection of nano- and microscale objects through the light scattered at wavevectors of order μm^{-1}. The scattering intensity is proportional to the sixth power of the scatterers' sizes; thus, in a solution containing objects of varying size the scattering signal is dominated by larger particles. This feature makes this technique particularly well suited to characterize the size and number distribution of the small aggregates (p53 oligomeric assemblies) that appear as bright cyan spots in OIM micrographs (Fig. 12.3B-F). The aggregation of p53 strongly depends on temperature. Solutions incubated at 15°C contain no visible aggregates (Fig. 12.3B). Solutions incubated at 18°C, however, contain a few aggregates (Fig. 12.3C), indicative of appearance of small oligomeric assemblies. Pronounced aggregation is observed in solutions heated to temperatures of 37 °C (Fig. 12.3B-F), with the average size and number of the aggregates both increasing nonlinearly with temperature (Fig. 12.3G-H) [92, 109, 112]. The remarkable growth in size and number of these aggregates at temperatures close to the mid-denaturation point of p53 [163] (Fig. 12.3 G-H) suggests that unfolding of p53 may be an essential trigger for aggregation [154, 164, 176]. To determine the solubility of p53 with respect to the aggregate phase, we measured the concentration of protein that remains soluble once aggregation is complete for solutions incubated at two conditions: at T =15 °C with no condensate, and at T = 37 °C, where earlier studies reported the formation of p53 fibrillar aggregates. The final p53 was nearly identical to the initial concentration, confirming that the protein did not form large aggregates at this temperature (Fig 12.3I). The final p53

concentration in solutions incubated at T = 37°C, however, was sharply lower than the initial concentration, with aggregates capturing up to 80% of the total p53 (Fig. 12.3J).

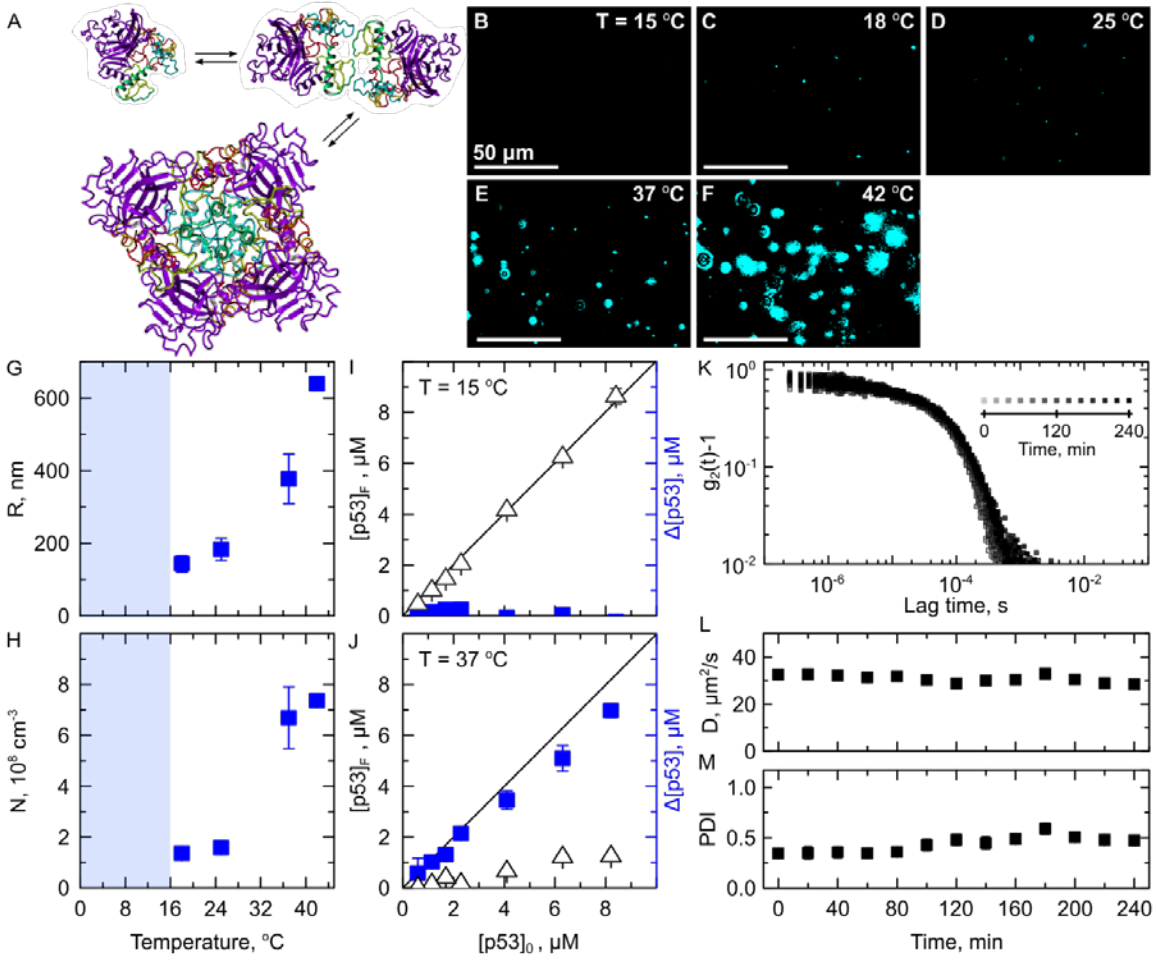

Figure 12.3. Temperature promotes p53 aggregation. (A) Oligomerization of p53. Full length structure of p53 is generated by inputting the FASTA sequence in PHYRE2 algorithm available online using intensive mode. 82% of the residues are modelled with more than 90% confidence. Residues 96-354 (DBD and OD) are modelled using p53 template on PDB with 100% confidence [53, 177]. (B-F) Representative image of oblique illumination microscopy (OIM) collected after incubation for 20 minutes at each temperature. The observed volume is $5 \times 80 \times 120$ µm^3. Aggregates appear as cyan spots. (G-H) The average size and the total number of the aggregates determined by OIM respectively. The average of five determinations in distinct solution volumes is shown. Error bars indicate standard deviations. The p53 concentration is 2.2 µM. (I-J) Concentration determination of p53 using UV-Vis spectrophotometry after incubation at two distinct temperatures of (G) 15°C and (H) 37°C. Black triangles show concentration of p53 solution after filtration to remove any aggregates after incubation. Blue rectangles demonstrate the concentration of p53 incorporated into the protein aggregates, calculated by subtraction of initial concentration of p53 from the final. (K) Intensity correlation functions g_2 of the light scattered by a p53 solution at 6 µM incubated at 15°C for 4 h. G_2 is steady over 4 h incubation at 15°C. (L-M) Evolution of diffusivity and dispersity of protein solution generated by polydisperse fitting of the intensity correlation functions. The error bars are generated from four different intensity correlation functions.

Surprisingly, the final p53 concentration in solution was not constant, instead decreasing with respect to the initial p53 concentration (Fig. 12.3J). This finding is in striking contrast with fibrillar aggregation, for which the final solution displays a constant solubility with respect to the fibril polymorph [178, 179]. This result thus suggests that p53 fibrillation may be driven by a non-classical condensation. Although p53 solutions at low temperatures appeared to be homogeneous, the methods employed are more suitable for large aggregates. To determine whether p53 solutions contain small oligomers or aggregates below the OIM resolution limit (R < 20 nm), we used dynamic light scattering to characterize any small condensates. The intensity-intensity correlation functions revealed one distinct yet broad shoulder (Fig. 12.3K), indicating the presence of aggregates of a broad size range. The average diffusivity $D_m = 32\ \mu\text{m}^2\ \text{s}^{-1}$, extracted from a polydisperse cumulant fit, is almost 4 times slower than diffusivity expected for the 43.7 kDa monomer ($D_m = 120.0\ \mu\text{m}^2\ s^{-1}$) indicating that majority of p53 exists as tetramers. The considerable polydispersity ($\mu\tau^2 \sim 0.35$) is indicative of the presence of multiple small oligomeric species, including dimers and octamers as previously reported [43, 166]. Both average diffusivity (D_m) and polydispersity ($\mu\tau^2$) remained constant over time, confirming that the p53 solution was stable over 4 hours of incubation at T = 15°C.

Crowding induces p53-rich clusters

Our initial temperature study revealed that solutions prepared at T =15°C contained only small oligomers and no large aggregates (Fig. 12.3B, I, K–M). To explore the effects of crowding on aggregation, we next examined the change in condensation of p53 at T =15°C upon addition of Ficoll, a crowding agent. Oblique illumination microscopy (OIM) revealed that the p53 undergoes significant condensation when Ficoll is added to solutions (Fig. 13.3A). Surprisingly, the average size of the condensates, 80 – 90 nm, was independent of both p53 and Ficoll concentration (Fig. 13.3E–F). Condensates captured more than 70% of protein content, but did

not display solubility; instead, the final p53 concentration in the supernatant was an exponential function of the initial concentration (inset to Fig. 13.3G). These features distinguish the observed condensates from common types of aggregation observed in proteins, such as amyloid fibrils, liquid–liquid phase separation, and amorphous aggregates. In fibrillar aggregation or liquid-liquid phase separation, the final protein concentration in the supernatant is constant and is independent of the initial concentration, indicating the solubility with respect to the fibril polymorph or the inverse of the equilibrium constant for phase separation. In the case of protein fibrils, the average length of the fibrils increases for higher initial protein concentration. In solid aggregation, the final solute concentration increases monotonically as a function of initial value, and the aggregate size depends monotonically on protein concentration. Unlike these typical aggregation pathways, crowding induces unusual condensation of p53: the condensate size was independent of protein concentration and the final p53 concentration was an exponential function of the initial concentration. These unusual features have been previously reported for mesoscopic protein-rich clusters that facilitate non–classical nucleation and are, importantly, in equilibrium with the solution. The current theory of cluster formation suggests that protein complexes such as dimers, trimers, tetramers, etc. enhance protein-protein interactions in the cluster core. Whereas the formation of these complexes is frequently driven by mechanisms involving partial unfolding of the proteins, the lack of dependence of cluster size on protein concentration in this theory arises from kinetics, as the size of the condensate is determined by the balance between the lifetime of complexes and their rate of outward diffusion from the cluster core [69, 72, 75, 168, 180]. By contrast, the exponential dependence of protein concentration, is a consequence of thermodynamic equilibrium, which requires equality of the chemical potentials inside the cluster and in the bulk solution.

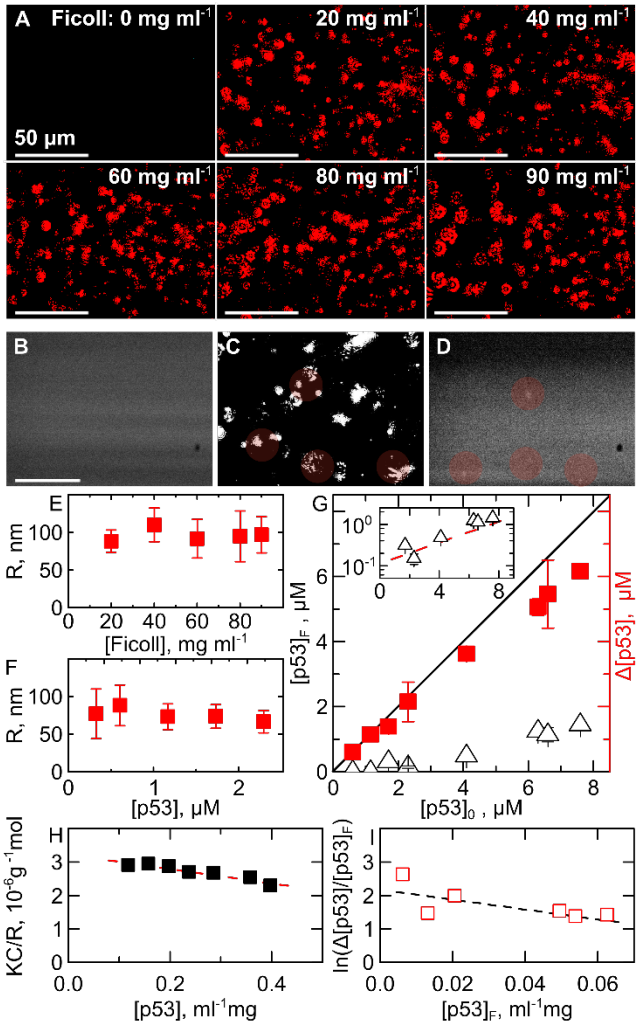

Figure 13.3. Crowding induces p53-rich clusters at T = 15 °C. (A) Representative image of OIM collected immediately after addition of crowder to the protein solution. The observed volume is 5 × 80 × 120 μm^3. Clusters appear as red spots. The p53 concentration is set at 1.2 μM and crowder concentration varies from 20 to 100 ml^{-1}mg at T = 15°C. (B-D) Micrographs of incorporation of Ficoll into p53 clusters collected after 2 hours of incubation of samples at 15°C in presence of 15 mg ml^{-1} BODIPY labeled Ficoll and 41 mg ml^{-1} un-labeled Ficoll (B) fluorescence OIM image of control sample with no protein in presence of 530 nm filter cube in the optical path, (C) OIM micrograph in presence of 1.2 μM p53, and (D) fluorescence OIM of 1.2 μM p53 solution. Red circles demonstrate clusters containing BODIPY labeled Ficoll inside. (E-F) The average size of the clusters as a function of Ficoll and p53 concentration, respectively determined by OIM. In panel E and F the p53 and Ficoll concentration is set at 1.2 μM and 90 ml^{-1}mg respectively. The average of five determinations in distinct solution volumes is shown. Error bars indicate standard deviations. The p53 concentration is 1.2. Due to existence of too many clusters in the solution, determination of total number of clusters by OIM is not possible. (G) Concentration determination of p53 using UV-Vis spectrophotometry after incubation at T = 15°C in presence of 56 mg ml^{-1} Ficoll. Black triangles show concentration of p53 solution after filtration to remove any formed aggregates after incubation. Red rectangles demonstrate the concentration of p53 incorporated into the p53-rich clusters, calculated by subtraction of initial concentration of p53 from the final value. (H) Static light scattering of p53 solution (I) dependence of protein concentration inside mesoscopic clusters on final solute concentration in the solution

Under the assumption of equilibrium, the solute concentration inside the cluster C_2 is given by $C_2 = C_f \exp\left(-\frac{\psi_2 - \mu_1^0}{RT}\right) \exp(2B_2 M_w C_f)$, where C_f is the final solute concentration in the bulk. Thus the cluster theory predicts that the ratio of concentration of protein captured in clusters (Δ[p53]) to the final concentration of p53 in the supernatant ($[p53]_f$) should be a linear function of $[p53]_f$ with slope related to the second virial coefficient (B_2). To test this prediction, we determined the second virial coefficient B_2 of the p53 solution by light scattering [174, 181]. This analysis yielded molecular weight $M_w = 303$ kDa and $B_2 = -1.1 \times 10^{-3}$ mol m^{3}kg^{-2} (Fig. 13.3H). This value of M_w, nearly 6–7 times that of the p53 monomer, indicates the presence of higher order oligomers (up to octamers) in the solution (Fig. 13.3H). This result is consistent with the high polydispersity of p53 solutions and the observed slow diffusion (approximately that of the tetramer) obtained from DLS (Fig. 12.3L-M). The considerable negative value for B_2 indicates that attraction between p53 molecules drives the formation of these condensates. Finally, the slope of $\Delta[p53]/[p53]_f$ as a function of $[p53]_f$ (Fig. 13.3I) was negative, similar to B_2, suggesting that the condensates that are formed in the presence of crowders resemble the protein-rich clusters [72, 74, 75]. There is, however, an unexpected order of magnitude difference between the slope of Fig. 13.3I (slope = 14.0) and the value predicted from theory ($2B_2M_w = 0.1$). This discrepancy suggests that the magnitude of B_2 and M_w may be altered by interactions between Ficoll and the p53-rich clusters. To test whether Ficoll incorporates into the clusters, we examined solutions of fluorescently-labeled Ficoll with and without p53 using OIM. We observed that p53 condensation induced by crowders also occurs in solutions containing fluorescently-labeled Ficoll (Fig. 13.3C). Moreover, some of these p53 condensates exhibit localized fluorescence (Fig. 13.3D). Because solutions of Ficoll with no p53 are uniformly bright (Fig. 13.3B), this result confirms that Ficoll is indeed captured in some of the p53 condensates. Incorporation of Ficoll into p53 clusters

likely modifies the protein-protein interactions (B_2) and may also increase M_w, thus addressing the deviation in the slope extracted from Fig. 13.3I from that predicted by theory.

Maturation of p53-rich clusters

The unusual concentration dependence and lack of solubility of the condensates formed in the presence of Ficoll suggests that these condensates may be protein-rich clusters. As a test of this idea, we monitored the time evolution of these condensates during incubation at T = 15°C (Fig. 14.3A). At the end of incubation, while the condensate number decreased, their size increased as a power-law with time, $t^{0.38\pm0.08}$, on short time scales, and saturated within 60 minutes (Fig. 14.3B–C). This observation is reminiscent of the Ostwald ripening of protein-rich clusters reported in earlier work for other proteins [67, 72, 74, 75, 78, 112]. In Ostwald ripening, the average size of clusters grows in order to minimize the overall free energy of the thermodynamic system. The smaller clusters, which are less stable due to their higher surface energy, dissolve and result in supersaturation of the solution. This supersaturation, in turn, drives condensation of the solute to the more stable large phases; thus, the condensate size increases and their number decreases. One scenario for Ostwald ripening, which assumes diffusion is the slowest step, is provided by the Lifshitz–Slyozov–Wagner (LSW) theory, which predicts that the condensate size grows as a power law with time with exponent of 1/3. This exponent is similar to that observed in the time evolution of the Ficoll-induced condensates (Fig. 14.3B) [112, 168, 182-184] indicating that these condensates grow with a mechanism similar to Ostwald ripening. Growth via Ostwald ripening is distinct from the growth observed in early stage fibril formation, which requires exposure of hydrophobic sites by protein unfolding. This comparison suggests that p53-rich clusters are distinct from fibrillary aggregates. To confirm that the observed ripening is not due to early stage fibril development, we characterized the structural integrity of the protein in our condensates using a 1-anilino-8-naphthalenesulfonate (ANS) assay, which is commonly

applied to detect partially unfolded states of proteins by binding to the exposed hydrophobic sites. During early stages of amyloid fibril formation, the pronounced increase in ANS fluorescence intensity ($\lambda_{emission}$ = 500 nm) indicates the presence of small oligomeric species containing misfolded proteins driving aggregation [95, 106, 175]. In sharp contrast, the ANS fluorescence of our p53 solutions without or with Ficoll exhibited no change over 4 hours (Fig. 14.3C inset) and the average value (0.1–0.12) was less than 15% of that of fibrillar aggregates.

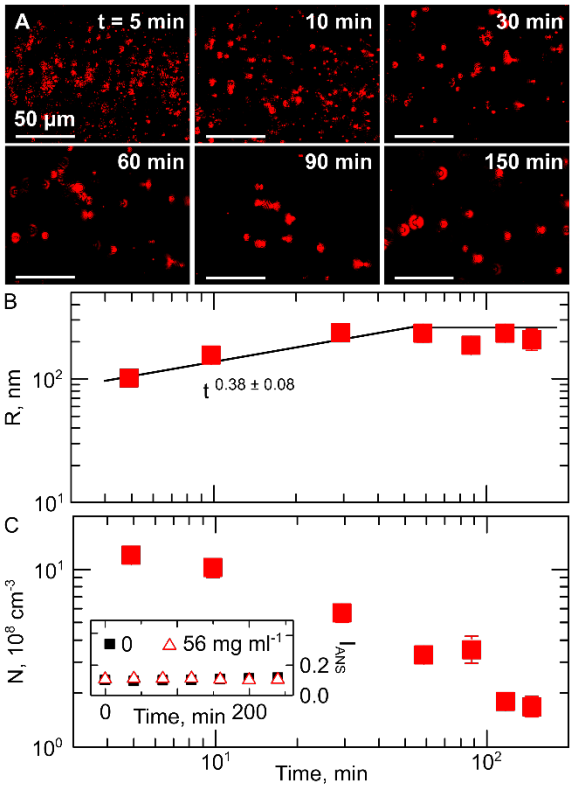

Figure 14.3. Maturation of p53-rich clusters. (A-G) Representative OIM image collected after each incubation time. The observed volume is 5 × 80 × 120 μm^3. Clusters appear as red spots. Temperatures is set at 15°C and Ficoll and p53 concentrations are 56 ml^{-1}mg and 1.2 μM respectively. (B-C) The average size and number of the clusters as a function of time determined by OIM. The average of five determinations in distinct solution volumes is shown. Error bars indicate standard deviations. The p53 concentration is 1.2 μM. The inset indicates normalized fluorescence emission at λ = 500 nm of p53 solution in presence of 8-Anilinonaphthalene-1-sulfonic acid (ANS) measured using excitation at λ = 350 nm with 56 mg ml^{-1} Ficoll (red triangles) and without Ficoll (black rectangles) for incubation at T = 15°C for 4 hours with 40 minutes interval. The p53 and ANS concentrations are 7.7 and 850 μM respectively. The emission intensity is normalized to the maximum value observed in presence of fibrillar aggregates.

This finding confirms that p53 is stable at low temperatures, in accord with the stability also observed using DLS (Fig. 12.3), and further indicates that Ficoll does not alter p53 conformational stability. Together, these observations suggest that the p53-rich clusters grow by Ostwald ripening with no significant perturbation in the conformation of p53 (Fig. 14.3B–C) [106, 185-187]. The results presented in Figs. 13.3 and Fig 14.3 illustrate that p53 in a crowded environment is capable of forming mesoscopic protein-rich clusters, driven by an increase in the strength of the p53-p53 interactions. Similar to mesoscopic protein clusters, p53 condensates grow in size similar to Ostwald ripening; their number density is decoupled from the cluster size; and the protein structure integrity is mostly preserved inside the condensates, as reported for other protein clusters [67, 74, 168, 182, 183]. Intriguingly, at low temperatures, these clusters form only in the presence of the crowding agent Ficoll. This condition is reminiscent of the conditions inside cells, where the volume fraction of crowders may be as high as 40%, and suggests that cluster formation of p53 may also play a role in physiological conditions.

Reversibility and nucleation and growth of p53 fibrils

To mimic physiological conditions, we increased the temperature to 37 °C and examined protein aggregation with and without crowders. All solutions of p53 incubated at T = 37 °C, whether without (Fig. 15.3A) or with (Fig. 15.3B) Ficoll, exhibited aggregates. To determine the nature of these aggregates, we used a Thioflavin T (ThT) assay; the fluorescence emission of ThT ($\lambda_{emission}$ = 488 nm) increases considerably upon binding to the β-sheet stacks common in amyloid structures. Aggregates formed both in the presence (Fig. 15.3A) and absence (Fig. 15.3.B) of Ficoll exhibited strong fluorescence when exposed to ThT, indicating that the p53 aggregates formed at T = 37 °C contained fibrillar structures in the presence or absence of crowder.

Aggregates of p53 formed in the presence of Ficoll were more compact compared to those formed in the absence of Ficoll (Fig. 15.3A-B), suggesting that Ficoll is captured inside these

aggregates. We incubated fluorescein-labeled Ficoll with unlabeled p53 at T = 37 °C and imaged the solutions with fluorescence microscopy after aggregation was complete. Whereas micrographs of solution without p53 were uniformly fluorescent and displayed no detectable aggregates (Fig. 15.3C), solutions containing both (unlabeled) p53 and (labeled) Ficoll contained green fluorescent aggregates (Fig. 15.3D). This experiment confirmed that the aggregates of p53 formed at 37 °C contained Ficoll, just as p53-rich clusters at T = 15°C, and this can modify the morphology of the aggregates. By contrast, capture of Ficoll did not alter the lack of solubility of these aggregates. The final concentration of p53 after filtration increased monotonically with the initial p53 concentration in the presence (Fig. 15.3E) or absence (Fig. 12.3J) of the crowder. Although the ThT assay revealed that the aggregates contained fibrillar structures, the aggregates did not exhibit the solubility expected for fibrils, suggesting the aggregates formed at 37 °C are composed of at least two different types of condensates. One type is clearly the fibrillar structures that are indicated by the positive ThT response. We hypothesize that the second type is akin to the p53-rich clusters formed at lower temperatures (15°C), which are both reversible and lack solubility. We therefore carried out assays to look for signatures of clusters at higher temperatures. First, we used dynamic light scattering to determine whether p53 condensates formed at T = 37°C in the absence of Ficoll exhibit reversibility. To eliminate the formation of large aggregates (whose scattering would be expected to dominate the small clusters), we examined only low concentrations of p53 solution. The intensity-intensity correlation functions of p53 solutions prepared at 37°C exhibited two distinct, broad shoulders (Fig. 15.3F). The first shoulder is indicative of polydisperse oligomeric species (R_m ~ 10 nm and $\mu\tau^2$ ~ 0.39) and the second corresponds to p53 condensates (R_c~150 nm and $\mu\tau^2$ ~ 0.42), whose size is similar to that of the p53-rich clusters observed in presence of Ficoll at T =15°C (Figs. 12.3 and Fig. 13.3). From the correlation functions, we calculated the concentration of these

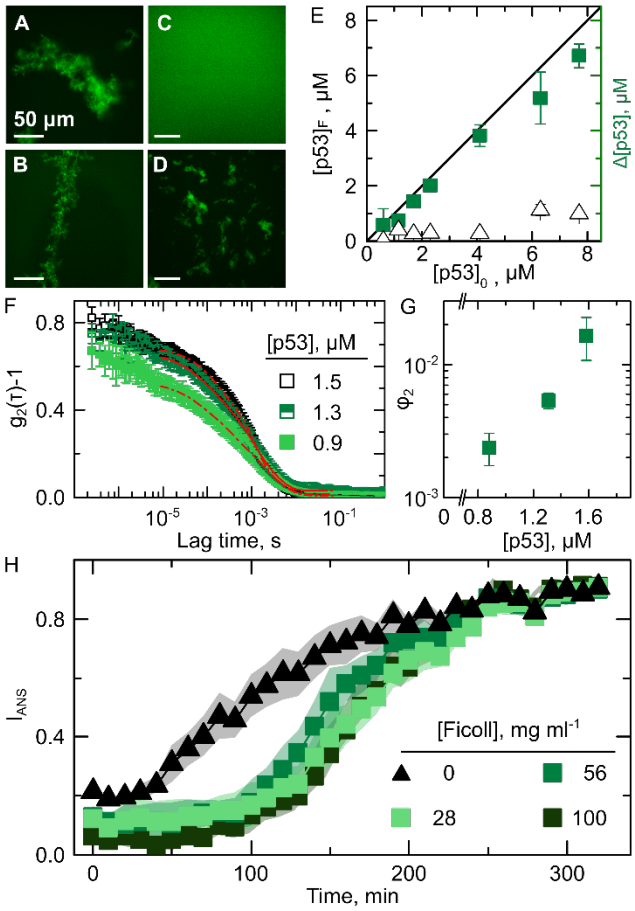

Figure 15.3. Reversibility and nucleation and growth of p53 fibrils. (A-B) Representative fluorescence micrograph of Thioflavin T (ThT) binding to fibrillar p53 aggregates formed by incubation of protein sample at 37°C over 12 hours (A) with no Ficoll and (B) with 56 mg ml^{-1} Ficoll. The ThT and p53 concentrations are 200 μM and 7.7 μM respectively. (C-D) Representative fluorescence micrograph of incorporation of Ficoll into p53 aggregates formed by incubation at 37°C over 12 hours in presence of fluorescein labeled Ficoll at 56 mg ml^{-1} (C) with no protein and (D) with 7.7 μM p53. (E) Concentration determination of p53 using UV-Vis spectrophotometry after incubation at T = 37°C in presence of 56 mg ml^{-1} Ficoll. Black triangles show concentration of p53 solution after filtration to remove any formed aggregates after incubation. Green rectangles demonstrate the concentration of p53 incorporated into the fibrillar p53 aggregates, calculated by subtraction of initial concentration of p53 from the final value. (F) Intensity correlation functions of p53 solutions for three concentration of protein obtained by serial dilution of the stock at 1.5 μM to 1.3 and 0.9 μM. (G) The dependence of volume fraction of fibrillar aggregates on the protein concentration obtained by serial dilution of a stock p53 at 1.5 μM incubated for 4 hours at T = 37°C to allow growth of the fibrillar aggregates.(H) Normalized fluorescence emission at λ = 500 nm of p53 solution in presence of 8-Anilinonaphthalene-1-sulfonic acid (ANS) measured using excitation at λ = 350 nm in presence of no crowder (black triangles) and with 28, 56, and 100 mg ml^{-1} Ficoll (full, half open, and open rectangles respectively) measured over 6 hours at T = 37°C. The p53 and ANS concentrations are 6.5 ± 0.5 and 850 μM respectively. The emission intensity is normalized to the maximum value observed in presence of fibrillar aggregates.

condensates as a function of the p53 concentration to determine if they exhibit the reversibility expected for p53-rich clusters. The volume fraction of p53 condensates formed at low

concentrations of p53 at T = 37°C exhibited a non-linear dependence on protein concentration (Fig. 15.3G): a twofold dilution of the protein concentration, from 1.6 to 0.8 μM, generated an order of magnitude decrease in volume fraction of clusters, from ~10^{-4} to ~10^{-5}.Because the volume fraction of irreversible aggregates would increase linearly with protein concentration, this result indicates that the p53 condensates formed at high temperatures are reversible. The size and reversibility of the condensates formed at 37°C are similar to those observed for p53-rich clusters at 15°C, suggesting that p53-rich clusters also form at physiological temperatures without Ficoll. Previous literature reported that solute-rich clusters promote nucleation; in the case of p53, Ficoll significantly promotes clustering of p53 at T = 15°C. Thus, we investigated if the presence of p53-rich clusters would tune the nucleation of p53 aggregates. The p53 rapidly aggregates in the absence of Ficoll, (Fig. 15.3H), with a lag phase shorter than 10 minutes and growth rate of 0.014 ± 0.003 min^{-1}. These kinetics are characteristic of fibril formation, as earlier studies have reported a short lag phase [59, 154, 176, 188, 189] and a growth rate of 0.02 min^{-1}. Surprisingly, p53 solutions containing Ficoll exhibited markedly different kinetics, with a longer lag phase of ~ 60 minutes and a faster growth rate of 0.028 ± 0.005 min^{-1} (Fig. 15.3H). How addition of crowders can induce these kinetics is not obvious. Excluded volume effects due to crowders would increase the chemical potential of the p53, thereby decreasing the nucleation time and increase the growth rate. By contrast, our experiments demonstrated a *slower* nucleation accompanying *faster* growth. The coexistence of clusters and fibrils, suggested by the unusual reversibility and lack of solubility, reconciles the contradictory kinetics of fibril formation. Incorporation of Ficoll into the clusters causes steric hindrance effects, which increases the nucleation barrier and lowers the nucleation rate. Faster growth of the fibrils, however, requires that they nucleate *within* the p53-rich clusters. Such a scenario is suggested by earlier studies of protein-rich clusters, which are known to contribute to non-classical nucleation

pathways in other protein and non-protein solutions. After nucleation, the higher local concentration of p53 inside clusters promotes the faster growth of the fibrils.

Together our findings revealed that p53 forms mesoscopic clusters prior to assembly into large fibrillar aggregates at higher temperatures and the fibrils nucleate inside these clusters, whose formation, facilitates the rapid nucleation of fibrils due to the locally high p53 concentration inside the cluster core. Presence of crowders significantly promotes cluster formation, which can capture some of the crowders inside. Importantly, these clusters demonstrate unusual features including reversibility, lack of solubility, and an average size of ~ 100 nm independent of p53 or crowder concentration. These findings although in vitro, they could provide new insights into the state of p53 inside the cell, where p53 can face 7–40 % (v/v) macromolecular crowding by other proteins, DNA/RNA, carbohydrates and etc. These clusters can potentially act as storage of p53 and protect the protein from formation of toxic amyloid aggregates by slowing down the nucleation time. Thus these clusters could be one potential therapeutic target for p53 aggregation which is suggested as one likely pathway for cancer development. Finally, it remains to be addressed what is the precise mechanism of p53 cluster formation, however we suggest that due to the IDP (intrinsic disorder protein) nature of the p53 and the excluded volume effects that rise by presence of crowder, the cluster formation may be driven by misassembled oligomers of p53 that form to lower the free energy and stabilize the thermodynamic system of the cell.

Summary

Our findings demonstrate that p53 is stable at temperatures far from its melting point of 42°C. By contrast, it forms mesoscopic protein-rich clusters that are in dynamic equilibrium with bulk solution and could aide nucleation of the fibrils. The locally high p53 concentration inside the cluster core results in the rapid nucleation of fibrils similar to previously reported non-classical

pathways [190], [10, 11, 178, 184, 187]. Although our data is not revealing the detailed protein conformation inside the cluster, the IDP nature of p53 and the excluded volume effects that rise in presence of crowders may suggest that the unfolding mechanism and formation of misassembled oligomers such as tetramers/pentamers might be the key for formation of these clusters at higher temperatures [67, 74, 112, 183]. We also found out that addition of crowder significantly promotes formation of these clusters at low temperatures with up taking more than 80% of the protein. Although our data demonstrates that these clusters are essential for nucleation of fibrillar aggregates, capturing the crowder molecules inside the cluster core can increase the nucleation barrier due to the steric hindrance effects and thus, slows down the nucleation of fibrils; in such a scenario, these clusters can potentially act as p53 storage and maintain the protein from formation of toxic aggregates prior to degradation by proteomic machinery. Together, these findings may suggest that inside crowded environment of the cells may indeed promote existence of p53 as mesoscopic clusters or liquid-liquid phase separated condensates that preserve the protein from aggregation by increasing the lag phase of the process. This shift of the lag phase to longer times might cooperate with proteostasis machinery to degrade the p53 within its 5–20 minutes half–life prior to toxic amyloid aggregation [17, 29].

Chapter 4 Differential dynamic microscopy of weakly scattering and polydisperse protein-rich clusters

Introduction

In this chapter, we demonstrate the applicability of brightfield DDM (b-DDM) to characterize weakly scattering and polydisperse biological nanoscale objects. As model systems we use solutions of two proteins, hemoglobin A and lysozyme, that contain polydisperse protein-rich liquid clusters of radius 70–250 nm which are precursors for protein nucleation [67, 68, 91]. Hemoglobin A is the main oxygen-transporting protein found in red blood cells; the presence of free heme in solution (the prosthetic group of hemoglobin) promotes the formation of hemoglobin clusters. Lysozyme is a well-studied and robust protein for which cluster formation is thought to be due to conformational changes in the lysozyme dimer. Both solutions scatter light only weakly, and the properties of the clusters of both proteins remain constant over many hours at room temperature. Using b-DDM, we obtain the average diffusion coefficient from the wave-vector dependence of the diffusive relaxation time. First, we show that the signal-to-noise ratio obtained in b-DDM depends on the thickness of the sample chamber; as a consequence, the accessible range of wave vectors is maximized with minimal sample volume at an optimal chamber thickness. Second, we find that the average diffusion coefficient of clusters obtained from b-DDM measurements is consistently smaller than that obtained from DLS at a scattering angle of 90°. We attribute the apparent discrepancy between b-DDM and DLS to a combination of Mie scattering and polydispersity: b-DDM accesses smaller scattering angles than DLS and hence captures more signal from the larger clusters, which preferentially scatter more light in the forward direction. These results demonstrate that DDM is a simple yet powerful tool for characterizing weakly-scattering and polydisperse submicron particles, including many found in biological settings.

Material and Methods

Lysozyme Lyophilized lysozyme, purchased from Affymetrix, was dissolved at 200 mg ml^{-1} in pure deionized (DI) water. Protein concentration was determined by absorbance measurements using a Beckman Coulter DU 800 spectrophotometer and extinction coefficient ϵ = 2.64 ml mg^{-1} cm^{-1} at 280 nm. The solution was dialyzed for two days against DI water to remove undesired low molecular weight salts. After dialysis, the solution was adjusted to a concentration of 103 mg ml^{-1} and filtered through 0.45 µm Polyethersulfone (PES) syringe filters prior to all measurements. The measured pH of this solution was 5.41 likely due to acidic salts present in the lyophilized powder after purification.

Hemoglobin A Blood from healthy adults was collected at the University of Houston Health Center (UHHC) following a protocol approved by the University of Houston Committee for Protection of Human Subjects. 1 mL of blood was diluted to 50 mL using PBS buffer. We centrifuged the diluted blood for 20 minutes. We decanted and discarded the supernatant containing blood plasma, white blood cells, and other blood components. We repeated the sequence of washing with PBS, centrifugation, and supernatant removal two additional times for a total of three washes. After that we added from deionized water to the precipitated red blood cells to a final volume of 15 ml with mild agitation of the solution to resuspend. The red blood cells ruptured under the influence of the osmotic pressure difference between the cells and the water. The RBC lysate was centrifuged at 5000 rpm at 4°C overnight followed by filtration using 0.45 µm SFCA syringe filters. Purification of the Hemoglobin A (HbA) was carried out by binding the protein to a strong anion exchange Q-Sepharose resin under 20 mM Tris, 5% glycerol, pH = 8.5, followed by elution of HbA in 10 CV 1M NaCl (HbA program on AKTA). Collected fractions are further concentrated using a 30k Amicon filter. The concentrated HbA was further buffer exchanged using PD-10 desalting column into PBS buffer and stored in liquid nitrogen. A solution

sample was thawed and diluted to 50 mg ml^{-1} in potassium phosphate buffer at a concentration of 0.15 M and pH 7.35. The hemoglobin A concentration was determined using Drabkin's reagent (which converts hemoglobin to the cyan-met form) and extinction coefficient ϵ = 0.6614 ml mg^{-1} cm^{-1} at 540 nm for cyan-met hemoglobin[191]. The solution was filtered through 0.22 μm PES syringe filters prior to all measurements.

Differential dynamic microscopy (DDM) Samples for differential dynamic microscopy were sealed in glass chambers constructed from cover glasses. Two 22 × 22 mm^2 cover glasses (thickness 0.19–0.23 mm, Fisherbrand), separated laterally by ~ 10 mm, were attached to a rectangular cover glass with dimensions of 48 × 65 mm^2 (thickness 0.13–0.17 mm, Gold Seal) using an epoxy-based adhesive (Dev- con). A 22 × 22 mm^2 cover glass was then centered on top of the two cover glasses to create an open chamber. One side of the chamber was sealed with epoxy[192]. Protein solution was introduced into the chamber through the open side, which was then closed with epoxy. We assumed that the thickness of this chamber was 160 μm. To study the effects of chamber thickness on the b-DDM signal, we also used Borosilicate square capillaries (Vitrocom) with internal diameters of 500 μm and 800 μm. To access thicknesses smaller than 160 μm, we designed a wedge-shaped chamber. In this case, a single 22 × 22 mm^2 cover glass (thickness 0.19–0.23 mm, Fisherbrand) was attached using a UV adhesive (Norland Adhesive) to a rectangular cover glass with dimensions 48 × 65 mm^2 (thickness 0.13–0.17 mm, Gold Seal). A 22 × 22 mm^2 cover glass was placed over the top to create an open wedge-shaped chamber. One of the open sides was sealed completely using UV adhesive; the other one was partially sealed. Protein solution was introduced from the half-open side, which was subsequently sealed with UV adhesive. To calibrate the thickness at different locations along the wedge-shaped chamber, we filled it with a solution of fluorescently labeled poly(methyl methacrylate) (PMMA) particles. The chamber was imaged with a confocal point scanner (VT-Eye, VisiTech International) attached to

an inverted microscope (Leica DM4000) with a 100× oil-immersion objective (Leica Microsystems HCX PL APO, numerical aperture of 1.4) at wavelength 491 nm. The thickness at a select location was evaluated as the difference between the highest and lowest microscope stage positions at which fluorescently labeled PMMA particles were in focus. This method was constrained to thicknesses lower than 80 μm. To determine higher thicknesses in the same chamber, up to 125 μm, we assumed that the increase in thickness was linear and extrapolated from the measured thicknesses using the distance from the thin chamber edge. For b-DDM data collection, protein solutions were imaged on a Leica inverted microscope attached to 100× oil immersion objective using a high speed 8-bit AOS camera (AOS Technologies AG). The microscope was equipped with a condenser of numerical aperture 0.7; an electronic aperture inside the microscope was partly closed during measurements, reducing the effective numerical aperture to NA. ~0.41 for hemoglobin and NA ~0.23 for lysozyme and introducing maximum angles (θ_{max}) of 24.5° and 14°, respectively. We recorded multiple series of 4200 images of size 480 × 640 pixels^2 at a frame rate of 63 frames per second. To extract the dynamics of cluster diffusion from micrographs, a DDM algorithm was implemented as described in Cerbino et.al*[87, 88, 193].* Images separated by a fixed lag time τ were subtracted to obtain the intensity difference $\Delta(x; y;\tau) = I(x; y; t+\tau) - I(x; y; t)$, where $I(x; y; t)$ was the intensity at position $(x; y)$ measured at time t. τ ranged from 0.0158 s to 25 s. Because the size of clusters fell below the resolution limit of microscope, image subtraction generated a speckle pattern. We computed the two-dimensional Fourier transform (FFT) of $\Delta(x; y;\tau)$ and averaged over all image pairs with the same τ. This procedure yielded a Fourier power spectrum $\Delta(u_x; u_y;\tau)$, where u_x and u_y were the coordinates in Fourier space. For a given τ, averaging was performed over $4200 - n_f$ image pairs, where n_f = frame rate × τ. The Brownian motion of clusters was not geometrically constrained, and as a result the 2-D power spectra were

isotropic. We therefore averaged the 2-D power spectra azimuthally to obtain image structure functions $\Delta(q;\tau)$, where $q = 2\pi\sqrt{u_x^2 + u_y^2}$ is the wave vector magnitude.

The light scattered by monomers at small angles was negligible, and hence the b-DDM signal was predominantly due to cluster diffusion. In the DDM theory derived for a monodisperse population of scatterers[89, 194-197], the structure function is fit to $\Delta(q;\tau) = A(q)\left[1 - \exp\left(-\frac{t}{\tau(q)}\right)\right] + B(q)$, where $A(q)$ is a prefactor that depends on the generalized optical transfer function, $B(q)$ is the background, and $\tau(q)$ is the characteristic relaxation time of the scatterers at a wave vector q. Here we modified the standard DDM fitting function to model a polydisperse population of scatterers, and fitted $\Delta(q;\tau)$ of the protein cluster solutions at each q using a modified cumulant fit[167], $\Delta(q;\tau) = A(q)\left[1 - \exp\left(-\frac{t}{\tau(q)}\right)(1 + \frac{\mu t^2}{2})\right] + B(q), (1.4)$. $\tau(q)$ is the wave-vector dependent cluster relaxation time and $\mu\tau^2$ is a measure of the polydispersity of the cluster population. The use of the polydisperse cumulant function allowed us to describe curvature in $\Delta(q;\tau)$ at the shortest time scales that could not be well fitted using a single-exponential model. We found that $\tau \propto q^2$, and thus the diffusion coefficient D_c was evaluated as the slope of the straight line $1/\tau$ versus q^2. The range of wave vectors was determined by the optical properties of the experimental setup. The minimal accessible wave vector was $q_{min} = 2\pi/l$ where l was the largest dimension of the original images that were captured by the camera; using the typical $l = 140\ \mu m$, $q_{min} = 0.05\ \mu m^{-1}$. The maximum accessible wave vector was $q_{max} = 2\pi/\Delta l$ where Δl was the pixel dimension in the space of the image; using the typical $\Delta l = 0.21\ \mu m$, $q_{max} = 28\ \mu m^{-1}$. In practice, q_{max} was limited by the smallest resolvable distance that a cluster could travel between two frames.

Dynamic light scattering (DLS) Thirty intensity correlation functions were acquired at 90 ◦ for 60 s each to obtain an average intensity-intensity correlation function $g_2(\tau)$ at lag times τ ranging from 0.1 μs to 10 s. We therefore determined the characteristic diffusion times τ_m and τ_c of the monomers and clusters, respectively, by fitting the normalized correlation function with a square sum of two terms, a single exponential function corresponding to the monomer population and a modified cumulant function to model the polydisperse cluster population, $g_2(q,\tau) - 1 = \left(A_c \exp\left(-{}^{t}/_{\tau_c}\right)\left(1 + \mu_c \frac{t^2}{2}\right) + A_m \exp\left(-{}^{t}/_{\tau_m}\right)\right)^2 + \varepsilon(\tau), (2.4)$, where A_m and A_c are related to the concentration of monomers and clusters, $\mu\tau_c^2$ is the polydispersity of the clusters, and ϵ accounts for inevitable noise . We calculated cluster diffusivity by $D_c = 1/q^2\tau_c$, where $q = \left(\frac{4\pi n}{\lambda}\right)\sin(\frac{\theta}{2})$.

Viscosity determination We determined the average cluster radius R_c from D_c (measured using DDM or DLS) using the Stokes-Einstein equation: $R_c = k_B T/(6\pi\eta D_c)$. Viscosity of lysozyme solutions are determined by measuring the diffusive dynamics of polystyrene particles 2R = 2 μm in lysozyme solution. For hemoglobin A solution, viscosity is determined by $\eta = \eta_0 \exp\left(\frac{[\eta]C}{1-\left(\frac{k}{\vartheta}\right)[\eta]C}\right)$ where $\eta_0 = 0.937\, mPa.s$ is the viscosity of PBS buffer at T = 25 °C, $[\eta] = 0.036\, dL/g$ is the viscosity increment, C is the concentration of HbA in g/dL units, and $\left(\frac{k}{\vartheta}\right) = 0.42$ is constant depending on crowding and shape coefficient for non-spherical objects[67].

Characterization of the protein–rich clusters with b-DDM

We acquire optical microscopy movies of protein-rich liquid clusters diffusing in solution for two studied proteins. Optical brightfield micrographs of a hemoglobin A solution at a concentration of 50 mg ml^{-1} show that the clusters are too small to be directly resolved (Figure 16.4(a)); the large black spots correspond to dust and dirt in the microscope optical train.

Subtracting two micrographs that are separated by a fixed lag time τ generates an image with a diffuse speckle pattern, as shown in Figures 16.4(b)—(d). The fluctuations increase as the lag time separating the micrographs is increased, indicating that the cluster positions become increasingly decorrelated over time.

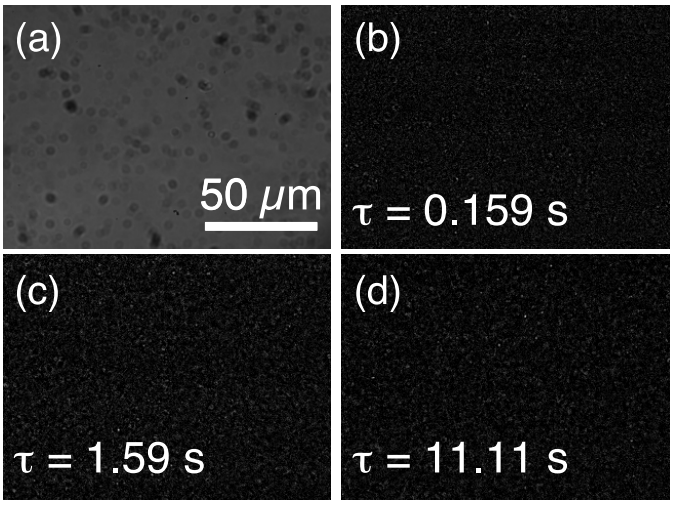

Figure 16.4 (a) Representative brightfield micrograph of a hemoglobin A solution with concentration 50 mg ml^{-1}. (b)—(d) Representative subtractions of two images at lag times τ, as indicated in the panels. The scale bar for all images is shown in panel (a).

To characterize the dynamics of these clusters, we apply b-DDM and investigate the behavior of the azimuthally averaged structure function $\Delta(q,\tau)$. At a constant lag time τ, $\Delta(q,\tau)$ exhibits a pronounced maximum at a particular wave vector q, as shown in Figure 17.4 for a solution containing hemoglobin A clusters. The location of this maximum (i.e., $1/q_{max}$) corresponds to the characteristic diffusive length scale at the lag time τ. Increasing the lag time shifts this maximum to lower q, as expected, and both the height and width of the maximum increase.[194] At a constant scattering wave vector q, $\Delta(q,\tau)$ first increases monotonically at short lag times and reaches a plateau at long lag times, as shown for solutions containing hemoglobin A and lysozyme clusters in Figure 18.4(a) and (b), respectively.

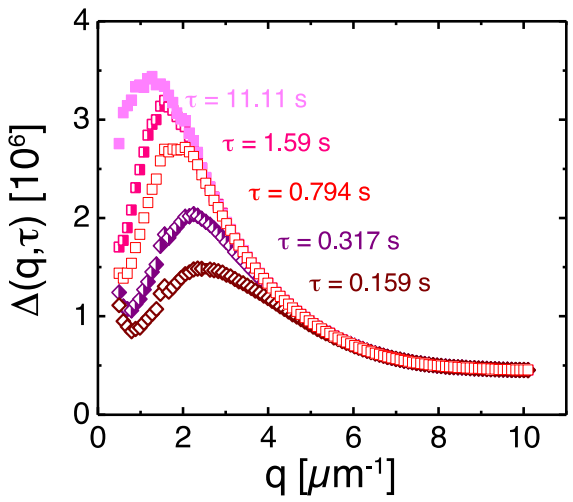

Figure 17.4. Structure function Δ as a function of wave vector q at lag times τ specified in the plot, obtained with brightfield differential dynamic microscopy (b-DDM) for a hemoglobin A solution with concentration 50 mg ml^{-1}.

For a fixed q, the structure function Δ can be fit to a single exponential decay (eq 1.4), from which we extract the q-dependent characteristic relaxation time $\tau_c(q)$, signal coefficient $A(q)$, and background term $B(q)$. The background term $B(q)$ is nearly constant at all wave vectors and does not differ significantly between the two proteins, consistent with the suggestion that $B(q)$ depends only on the power spectrum of the optical train of the microscope.[194] Hemoglobin A generates a measurable DDM signal for q = 0.5 – 6.9 μm^{-1}; by contrast, lysozyme generates a measurable signal for a smaller range of wave vectors, q = 1 – 4 μm^{-1}. Here a measurable signal is one for which the quotient $A(q)/B(q)$, one metric of the signal-to-noise ratio,[198] is greater than or equal to 0.04. For both proteins, the reciprocal relaxation time $1/\tau_c(q)$ scales linearly with q^2 (Figure 19.4) and a linear fit goes through the origin. These features indicate that the dynamics of the clusters is purely diffusive. We calculate the average diffusion coefficient for each cluster from the slope of the fit line and obtain D = 0.704 × 10^{-12} m^2 s^{-1} and 1.29 × 10^{-12} m^2 s^{-1} for hemoglobin A and lysozyme clusters, respectively. From the Stokes-Einstein equation, $2R_c = k_B T/3\pi\eta D$, where η is the viscosity of a solution of protein monomers, the characteristic diameters $2R_c$ of hemoglobin A and lysozyme clusters are 259 nm and 117 nm, respectively.

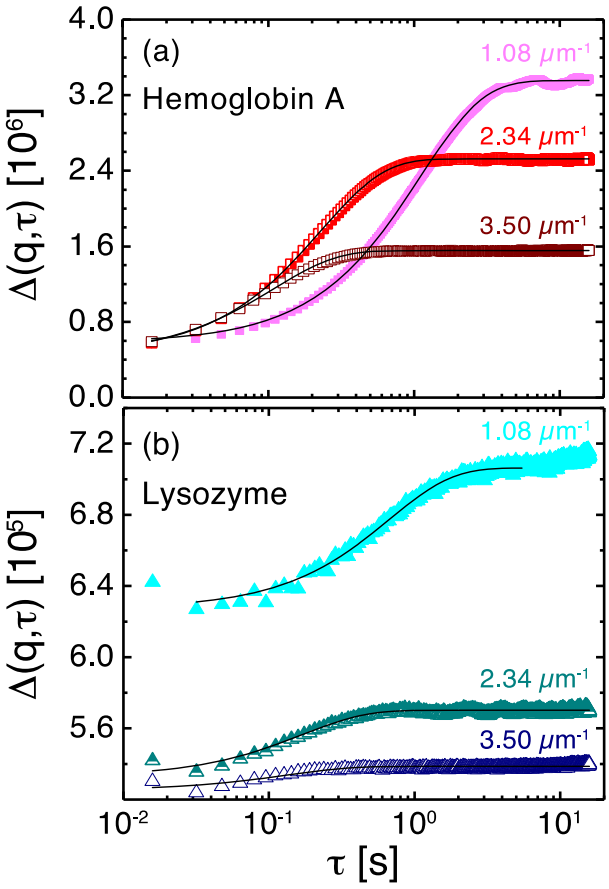

Figure 18.4. Structure function Δ as a function of lag time τ at three wave vectors q, indicated the plots, for solutions of (a) hemoglobin A at concentration 50 mg ml^{-1} and (b) lysozyme at concentration 103 mg ml^{-1}. Lines are best fits to eq 1.4.

The hemoglobin A clusters are larger and thus scatter more light, leading to a greater DDM signal-to-noise ratio as compared to that of lysozyme clusters, consistent with the structure functions shown in Figure 18.4.

Comparison with DLS

To verify the diffusion coefficients and cluster sizes obtained using b-DDM, we measure the characteristic relaxation time scale using dynamic light scattering (DLS) at a single scattering angle of 90°. The dynamic correlation functions $g_2 - 1$ of hemoglobin A (Figure 20.4(a)) and of lysozyme solutions (Figure 20.4(b)) exhibit two distinct relaxations, indicating the presence of objects of two different characteristic sizes.

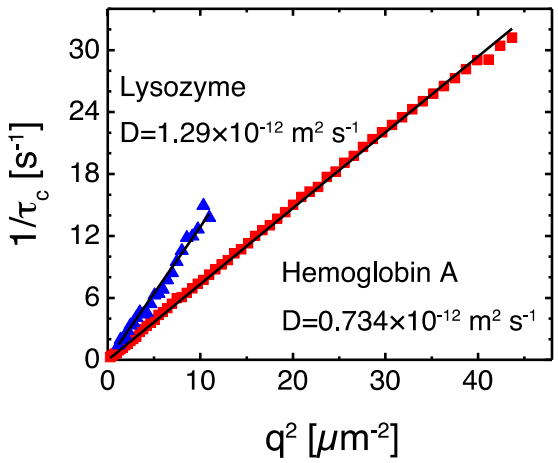

Figure 19.4. The reciprocal relaxation time $1/\tau_c$ as a function of the wave vector q for hemoglobin A solution with concentration 50 mg ml^{-1} (squares) and lysozyme solution with concentration 103 mg ml^{-1} (triangles). τ_c scales as q^{-2} and the intercept is insignificant (linear fits pass through the origin), as expected for freely diffusing clusters.

From each dynamic correlation function we obtain the corresponding intensity distribution function $G(\tau)$ using the CONTIN algorithm,[199, 200] shown in Figure 20.4(c) and (d) for hemoglobin A and lysozyme, respectively. For each protein, $G(\tau)$ exhibits two peaks. The sharp maximum at short lag times, at 0.04 ms and 0.01 ms, respectively, for hemoglobin A and for lysozyme, corresponds to the relaxation time of the monodisperse protein monomers. The broad peak at longer lag times corresponds to the distribution of relaxation times of the polydisperse clusters[180]; using the Stokes-Einstein equation, we calculate an average diameter of 171 nm and 90 nm, respectively, for hemoglobin A and lysozyme; these values are in agreement with previous determinations for both proteins.[74, 201] Notably, we find that the characteristic diffusion time of clusters obtained from DDM, indicated by the black arrows in Figure 20.4(c) and (d), is always longer than that obtained from the position of the maximum in $G(\tau)$ from DLS. This result indicates that the characteristic size measured by DDM is always larger than that obtained using DLS.

The effect of polydispersity on apparent cluster sizes

To understand the origin of this discrepancy between the sizes obtained from DDM and DLS, we consider the scattering process that generates both signals. For a particle of diameter $2R$ interacting with light of wavelength λ in a medium of refractive index n_m, the size parameter $x = 2\pi R n_m/\lambda$ determines the relevant scattering limit.

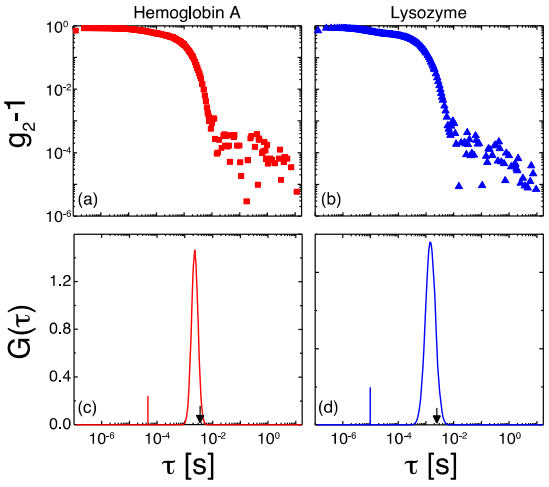

Figure 20.4. (a) and (b) Autocorrelation function $g_2 - 1$ of scattered light as a function of lag time Δt for (a) a hemoglobin A solution with concentration 50 mg ml^{-1} and (b) a lysozyme solution with concentration 103 mg ml^{-1}. All dynamic light scattering measurements were performed at a detector angle of 90°, corresponding to a scattering vector q = 18.7 μm^{-1}. (c) and (d) Corresponding intensity distribution functions G(τ), obtained by CONTIN,[199, 200] for (c) a hemoglobin A solution and (d) a lysozyme solution. The black arrows indicate the characteristic diffusion times determined by b-DDM.

The illumination source used in the microscopy experiments has a broad distribution of wavelengths; using an average wavelength of λ_0 = 550 nm for the incident white light, x = 2.60 and 1.37 for hemoglobin A and lysozyme clusters, respectively. Because the size of the particles is comparable to the wavelength of incident light, we consider the Mie solution to Maxwell's equations, which describes the scattering of an incident plane wave from a collection of spheres. The Mie solution is written as a series expansion in terms of spherical harmonic functions[202], which in turn are typically expressed in terms of the associated Legendre polynomials $P_l^m \cos(\theta) = \frac{(1-\cos^2\theta)^{\frac{m}{2}}}{2^l l!}\frac{d^{l+m}(\cos^2\theta-1)^l}{d(\cos\theta)^{l+m}}$. The angular dependence of the Mie angular functions

$\pi_n(\cos\theta) = (1/\sin\theta)P_l^m(\cos\theta)$ and $\tau_n(\cos\theta) = \frac{d}{d\theta}P_l^m(\cos\theta)$ thus determines the intensity of scattered light as a function of the scattering angle[203]. The function $\pi_n(\tau_n)$ exhibits fore-aft symmetry for even (odd) *n*, with lobes directed forwards (0°) and backwards (180°); for odd (even) *n*, however, the backward lobe vanishes. This angular dependence leads to a forward-directed bias in the scattering intensity that becomes more pronounced as the index *l* is increased. Furthermore, as the size of the scattering objects is increased, more terms in the series expansion are incorporated in the scattering diagram[204] and thus larger objects preferentially scatter more in the forward direction. We employ a Mie scattering model[205] to quantify the difference in magnitude of the intensity of forward- and laterally-scattered light for hemoglobin A clusters. For calculations of the DLS scattering intensity, we use the excitation wavelength of λ = 633 nm in our experimental DLS setup and a scattering angle of 90°. For calculations of the DDM scattering intensity, following ref [194], we assume that the distribution of wavelengths in the illumination source can be described by a Gaussian function centered at a wavelength λ_0 = 550 nm. At a single scattering angle, the intensity of scattered light increases as the particle radius is increased (Figure 21.4(a,b)). For a given particle radius, the scattered intensity is greater at 0° than at 90°, as expected in the Mie scattering regime. The DDM experiments access scattering angles ranging from approximately 1.8 to 15 degrees, as calculated from the minimum and maximum scattering vectors q = 0.5 and 4 μm^{-1} via $q = (4\pi n_m/\lambda_0)\sin(\theta/2)$ for which the structure function could be analyzed for both proteins. We note, however, that the proteins scatter light through all angles down to zero degrees, even if the structure functions cannot be analyzed at the lowest angles. To model the signal obtained in the DDM experiments, we therefore calculate the Mie intensity over an angular range of 0 – 24°. The resulting intensity at 90° as a function of particle radius exhibits a local minimum at a particular radius (Figure 21.4(c)), which arises from morphological resonances due to constructive interference[204]. The

protein-rich liquid clusters are not monodisperse but instead exhibit a broad distribution of sizes, as indicated by DLS. To assess the effect of cluster size polydispersity on the DDM signal intensity, we assume that the cluster size distribution can be described by a Gaussian function of characteristic width σ that is centered at the average radius of lysozyme clusters measured using DLS, R_c = 90 nm. We sum the Mie scattering intensities for lysozyme clusters of each radius, weighted by the Gaussian function, and thereby obtain the scattered intensity for a polydisperse distribution of cluster sizes. When the characteristic width σ is small ($\sigma/R \approx 0.025$), the distributions of scattered intensity at 0°, at 90°, and 24° (the maximum accessible DDM angle) strongly overlap with the distribution of cluster radii (Figure 21.4(d)), indicating that the characteristic radius measured at each angle is nearly identical. By contrast, when the cluster radii are more broadly distributed ($\sigma/R \approx 0.45$) the position of the maximum in scattering intensity is shifted to larger radius compared to that of the Gaussian radius distribution, as shown in Figure 21.4(e). Moreover, this shift is more pronounced for smaller scattering angular 0° and 24° corresponding to the angular range accessed in the DDM experiments, than at 90°, corresponding to the angle in the DLS experiments. This result is consistent with the experimental observations reported in Figure 20.4(c,d), confirming that polydispersity can generate the discrepancy between the DDM and DLS characteristic sizes. We quantify the predicted discrepancy between the characteristic sizes measured using b-DDM and DLS by the difference in peak positions for the 0° and 24° scattering intensity and the 90° scattering intensity and find that this discrepancy increases monotonically with σ (inset to Figure 21.4(d)). As the cluster size distribution broadens, the characteristic size measured by DDM becomes progressively larger compared to that measured by DLS.

Do thicker chambers yield stronger DDM signal?

The DDM measurements reported in Figures 16.4—21.4 are performed in thin chambers of thickness ~160 μm. Many biological samples are difficult to purify or obtain in large volumes, and so the use of thinner chambers and hence smaller sample volumes is desirable.

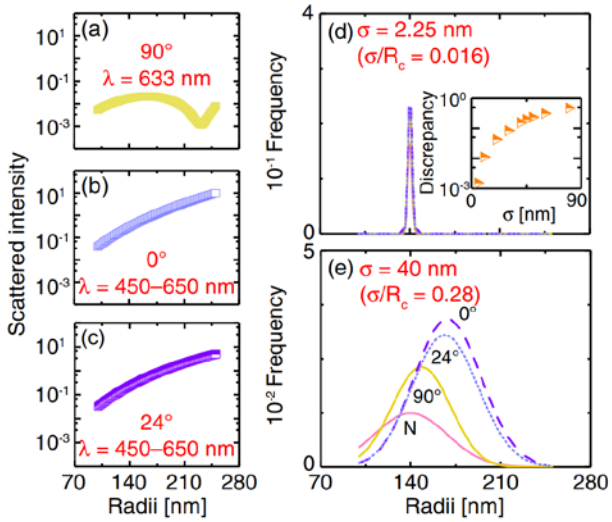

Figure 21.4. (a)—(c) Scattering intensity of lysozyme clusters as a function of cluster radius predicted using Mie scattering theory for (a) dynamic light scattering, using a wavelength λ = 633 nm and a scattering angle of θ = 90°; (b) b-DDM, using a wavelength range λ =450 – 650 nm and a scattering angle of θ = 0°; (c) b-DDM, using a wavelength range λ =450—650 nm and a scattering angle range θ = 0 – 10°. (d), (e) Calculated scattering intensity distributions containing clusters with a Gaussian size distribution (N) of width (d) σ = 2.25 nm and (e) σ = 40 nm. Inset in (d): Discrepancy between the peak positions predicted for DLS and DDM as a function of size distribution width σ.

The brightfield DDM method generates signal from a thickness that is greater than the focal volume of the optical train but can be limited by the sample thickness. The minimum sample thickness required to neglect finite size effects in the DDM signal is $L_{min} > 1/\Delta q$, where Δq is the uncertainty in the scattering wav be vector due to the finite numerical aperture of the condenser and the polychromaticity of the illumination source.[194] We calculate $(\Delta q/q)^2 \approx 0.0307$ using the expression from ref [194] and obtain L_{min} = 11 μm and 0.83 μm at the minimum and maximum q of 0.5 and 6.9 μm^{-1}, respectively, accessible with hemoglobin A solutions. To determine the chamber thickness required to generate signal in DDM for weakly scattering protein clusters, we measure the image structure function $\Delta(q, \tau)$ for hemoglobin clusters in chambers of thickness

ranging from 25 to 800 μm, for which we expect finite-size effects to be negligible. The dependence on chamber thickness arises from the fact that planes farther from the object plane contribute progressively less to the DDM signal[194]. At a low wave vector (q = 0.88 μm^{-1}) the signal above the noise (i.e., $A(q)/B(q)$) is sufficiently large, allowing each $\Delta(q,\tau)$ to be fit to eqn 2.4 and the relaxation time scale $\tau_c(q)$ to be extracted (Figure 22.4(a)). [198]At higher wave vectors, however, $A(q)/B(q) < 0.04$ for the thinnest sample chambers and these $\Delta(q,\tau)$ cannot be fit to eqn 1.4 (Figure 22.4(b)). Reducing the chamber thickness below ~160 μm restricts the range of wave vectors from which $\tau_c(q)$ can be extracted, in accord with the theoretical prediction from ref [194]. Nonetheless, over the accessible range of wave vectors for each thickness the inverse relaxation time $1/\tau_c(q)$ scales with q^{-2}; moreover, all points lie on a single line, confirming that the diffusion coefficient of the clusters remains constant across chambers of different thickness.

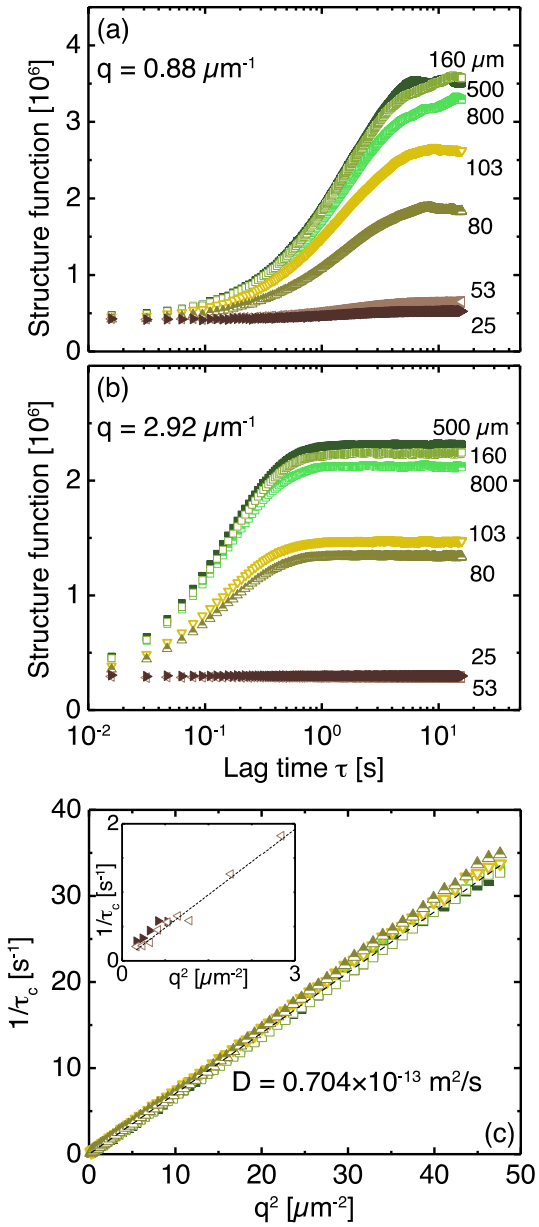

Figure 22.4. (a)—(b) Structure function $\Delta(q,\tau)$ as a function of lag time τ for a hemoglobin A solution at concentration 50 mg ml^{-1}, measured in chambers of indicated thicknesses as, at a wave vector (a) q = 0.88 μm^{-1} and (b) q = 2.92 μm^{-1}. (c) The reciprocal relaxation time $1/\tau_c$ as a function of the wave vector q for a hemoglobin A solution with concentration 50 mg ml^{-1} measured in chambers of varying thickness; symbols and colors correspond to those used in (a) and (b). Inset: same dependence for the two thinnest chambers (of thickness 25 μm and 53 μm), showing that the noisy and weak b-DDM signal can be measured only for a limited range of q.

Summary (DDM with weakly scattering clusters)

We show that DDM can be used to monitor the dynamics of weakly scattering and polydisperse biological nanoscale objects, protein-rich liquid clusters, and to characterize the sizes

of the clusters. The characteristic size measured by DDM is consistently larger than that measured by DLS at a scattering angle of 90°. Using the Mie scattering solution, we show that larger clusters preferentially contribute to the low-angle DDM signal, leading to a bias towards longer relaxation times and hence larger average sizes. This bias increases with the width of the cluster size distribution. This result neglects absorption from the clusters or scattering medium, which does not significantly affect the accuracy of data collected using scattering methods[206]; for example, the slight absorption of hemoglobin A does not affect cluster sizes measured using DLS[206] and we expect that it also does not significantly alter the shift in characteristic size using DDM. Increasing the thickness of the sample chamber enhances the signal from weakly scattering objects and hence increases the range of wave vectors accessible with DDM; above a certain thickness, here of order 100 μm, however, produces no further increase in the DDM signal.

Although here we focus on the dynamics of a well-characterized model system, our results are broadly applicable for polydisperse nanoscale biological particles that may weakly scatter light. Notably, we find that solutions with weakly polydisperse protein clusters exhibit exponential decays in DDM. This result is in sharp contrast to the stretched exponential dynamics of nanoparticles in homogeneous porous media measured using DDM[207], which may reflect local environmental heterogeneity[208]. This comparison suggests that DDM could be used to identify the physical origins of dynamical processes. When combined with optical methods used for concentrated suspensions[209] or extended analyses used for non-spherical objects[210, 211], we therefore expect that DDM will provide a simple, inexpensive, and rapid method to characterize the diffusive dynamics of a wide range of biological nanoscale objects in complex biological environments.

Chapter 5 Differential Dynamic Microscopy of Bidisperse Colloidal Suspensions

Introduction

In this chapter, we demonstrate a new application of DDM: the ability to resolve dynamics in a complex mixture containing two sizes of particles, using equipment comparable to that in the LMM on the ISS. We formulate dilute mixtures of polystyrene particles of radius 50 nm and 1 micron at different ratios of the large-to-small fraction at modest total volume fractions of $\phi \sim 10^{-3}$, at which both species freely diffuse. The 50 nm particles are too small to be resolved using standard optical methods. Using DLS and DDM, we measure the particle diffusivities in the mixtures. Whereas DLS is not sufficiently sensitive to resolve the dynamics of both species at these concentrations, DDM successfully measures the diffusivities of both large and small particles. The enhanced sensitivity of DDM derives from the preferential forward scattering of large objects. The scattered light from the large particles generates interference patterns that affect the amplitude of the dynamic correlation function. We show that this amplitude is non-monotonic and corresponds to the interference pattern, and thus may be used to characterize their average axial position. We anticipate that this approach can be applied to time series of images acquired on the LMM and in other space experiments – enhancing the time resolution and providing new insights into micro- and nanoscale dynamics in microgravity.

Material and methods

Fluoro-Max Dyed Red Fluorescent polystyrene particles with radii $a_L = 1$ µm and $a_S = 50$ nm (dispersity < 5%, as reported by the manufacturer) were purchased from Thermo Fisher Scientific. The nanoparticles were packaged as aqueous suspensions at a concentration of 1% solids by weight, which contained a trace amount of surfactant to inhibit particle aggregation. The refractive index of the nanoparticles was 1.59 and their density was 1.06 g cm^{-3}.

Samples for DLS and DDM experiments were prepared by diluting dispersions of nanoparticles from the as-received concentration (1 wt%) with deionized water that was filtered with 0.2 μm polyethersulfone syringe filters (Sterlitech). To minimize aggregation and ensure uniform dispersion, all samples were bath sonicated for 10 s prior to sample preparation. In these experiments, we fixed the volume fraction of the small particles at $\phi_S = 10^{-3}$ and prepared solutions with volume fraction ratio of large to small particles of $r = \phi_L/\phi_S$ = 0.003, 0.01, and 0.03 (i.e., $\phi_L = 3 \times 10^{-5}$ for r = 0.03, $\phi_L = 10^{-5}$ for r = 0.01, and $\phi_L = 3 \times 10^{-6}$ for r = 0.003). For dynamic light scattering measurement, we collected the light scattered at a fixed angle θ and a temperature of 20°C for 110 s and repeated this measurement ten times at each of three scattering angles θ = 30°, 50°, and 90°, corresponding to wavevectors $q = \left(\frac{4\pi n}{\lambda}\right)\sin(\theta/2)$ of 6.84, 11.18, and 18.7 μm^{-1}. For DDM data collection, particle suspensions were imaged on a Leica inverted microscope attached to a 63× oil immersion objective lens (NA = 1.4) using an 8-bit camera (AOS Technologies AG) at room temperature (≈ 20°C). The numerical aperture of the microscope condenser was 0.4 (NA $= D/f$, where f = 100 mm is the focal length of the tube lens and D = 40 mm is the diameter of exit light), which introduces too much incoherency to accurately implement DDM[194]. Hence to optimize the imaging conditions for DDM experiments, we manually reduced the condenser aperture to ~0.1 for r = 0.03 and 0.01 and to ~0.15 for r = 0.003, estimated by measuring the ratio of the average intensity of the images to the intensity of images acquired with the condenser fully open. For each sample, we recorded two series of 4200 images of size 480 × 640 $pixels^2$ at a frame rate of 63 frames s^{-1}.

Dynamic light scattering (bidisperse suspension of particles)

As a control experiment, we measured the diffusivities of particles of radius 50 nm and 1 μm, respectively, using DLS. In suspensions containing particles of uniform size, the intermediate scattering function $f(q,t)$ could be fitted to a single exponential, $f(q,t) = \exp\left(-\frac{t}{\tau_S}\right)$, (1.5),

where the time scale τ_s was related to the particle diffusivity via $D_s = 1/q^2\tau_s$. The measured diffusivities of the small (4.3 ± 0.1 μm^2/s) and large (0.20 ± 0.02 μm^2/s) particles were in good agreement with the diffusivities predicted from the Stokes-Einstein equation using the nominal radii (4.3 μm^2/s and 0.21 μm^2/s). To test the ability of DLS to measure dynamics of both species in a bidisperse mixture, we formulated samples containing a constant volume fraction of small particles, $\phi_S = 10^{-3}$, and added large particles at various concentrations to obtain volume fraction ratios of $r = \phi_L/\phi_s$ = 0.03, 0.01, and 0.003. The intermediate scattering functions $f(q,t)$, measured at three scattering angles, exhibited distinct shapes depending on the concentration of large particles. At the highest concentration of large particles (r = 0.03) and the lowest scattering wavevector (q = 6.8 μm^{-1}), $f(q,t)$ exhibited a second shoulder at long lag times (Fig. 23.5a); by contrast, no second shoulder was apparent at higher angles (e.g. for q = 18.7 μm^{-1} in Fig. 23.5a) or at lower concentrations of large particles (e.g. at q = 6.8 μm^{-1} and r = 0.003 in Fig. 23.5c). For bidisperse suspensions, the choice of an appropriate fitting model was determined by the scattering properties of the particles. The large particles used in these experiments were Mie scatterers[212]: the Mie parameter x for a particle of radius a_L= 1 μm interacting with light of wavelength $\lambda = 632.8$ nm in water (refractive index n = 1.33) was $x = 2\pi a_L n/\lambda$ = 13.2, much larger than the Rayleigh threshold[213] $x = 1$. The Mie parameter for the small particles was $x = 0.66$, slightly below this threshold. In the Mie regime, the scattering intensity is anisotropic with preferential forward scattering at low angles. Therefore, the contribution of both particles to the intermediate scattering function was angle- and concentration-dependent.

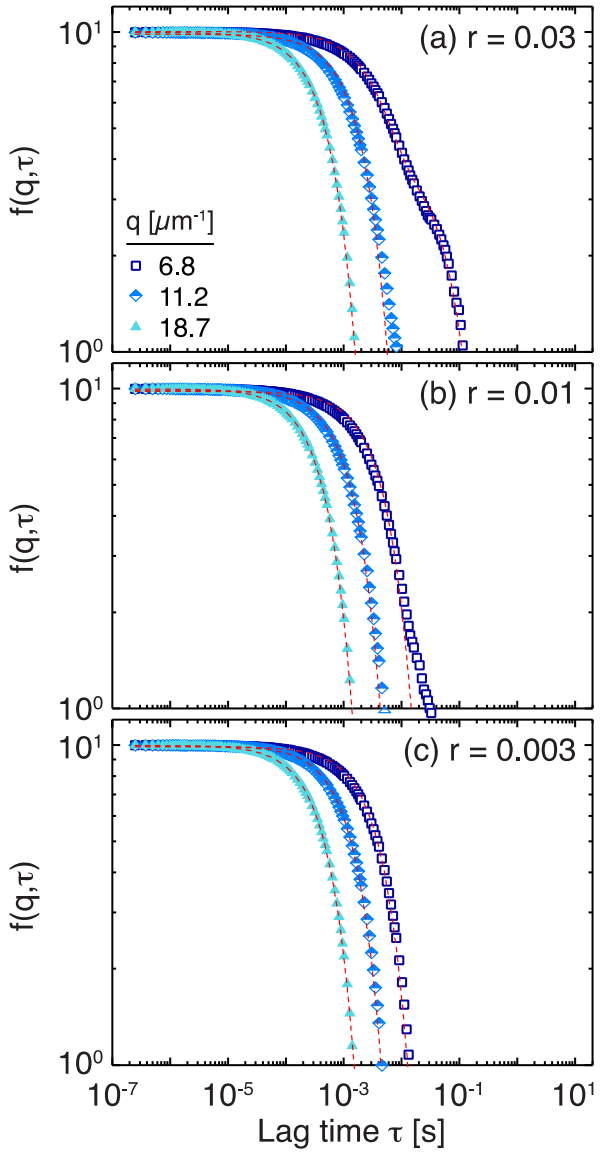

Figure 23.5. Intermediate scattering function $f(q,t)$ as a function of lag time t measured for bidisperse mixtures of particles of radius 50 nm and 1 μm formulated at a large-to-small volume fraction ratio r of (a) 0.03, (b) 0.01, and (c) 0.003 at wavevectors of q = 6.8 μm^{-1} (30°, squares), 11.2 μm^{-1} (50°, diamonds), and 18.7 μm^{-1} (90°, triangles). Red lines indicate fitting functions: eqn 2.5 for r = 0.03 and q = 6.8 μm^{-1} and eqn 1.5 otherwise.

The diffusivities calculated from the fitted time scale, $D_S = 1/q^2\tau_S$, reflected the rate of diffusion of small particles over the length scale $2\pi/q$ and were in good agreement with that from the unary control experiment (Table 1.5). At a higher large-particle ratio r = 0.03, the intermediate correlation function exhibited a second shoulder at the lowest wavevector (q = 6.8 μm^{-1}) indicative of two populations of diffusing particles. For r = 0.03, we fitted the intermediate

correlation functions at q = 6.8 μm^{-1} to the sum of two exponential functions, $f(q,t) = f_S \exp\left(-\frac{t}{\tau_s}\right) + f_L \exp\left(-\frac{t}{\tau_L}\right)$, (2.5), where τ_S and τ_L are the characteristic diffusion times of 50 nm and 1 μm particles, respectively, and f_S and $f_L = 1 - f_S$ are proportional to the amplitude of the scattered signal produced by each particle population. Again, the diffusion coefficient for each particle species was extracted from its characteristic diffusion time via $D_{S,L} = 1/q^2\tau_{S,L}$. The calculated diffusivities were larger than but comparable to those from the unary control measurements (Table 1.5); D_L, in particular, was significantly larger. The inability to accurately detect the large particles across the accessible range of wavevectors prohibited the use of DLS to characterize minority-large bidisperse suspensions at low volume fractions. Hence, we explored alternate methods for characterizing dynamics in these samples.

Differential dynamic microscopy

To evaluate the sensitivity of DDM to distinguish particles of two different sizes, we performed DDM measurements on the same series of samples. In the DDM theory, the structure function $\Delta(q;t)$ is related to the intermediate scattering function $f(q,t)$ via, $\Delta(q;t) = A(q)(1 - f(q,t)) + B(q)$, (3.5), where $A(q)$ depends on the optical transfer function of the imaging system and on the scattering properties of objects, and $B(q)$ captures any noise introduced into the system.[87, 194] For a population of monodisperse scatterers at low concentration, $f(q,t)$ is commonly fit to a single exponential decay (eqn 1.5). In samples with more complex dynamics, such as those featuring multiple relaxation timescales,[214, 215] a single exponential decay cannot be applied. Here, our goal was to determine the extent to which the sizes of particles in a bidisperse mixture could be resolved. Because DDM accesses a lower range of wavevectors than our DLS setup, the scattering intensity from the large particles is more pronounced than in DLS (Fig. 23.5d). Thus, we expected to observe two decays in the DDM signal for bidisperse mixtures, corresponding to the rate of diffusion for each particle size.

Table 1.5. Diffusivities obtained from dynamic light scattering measurements for unary (top two rows) and bidisperse (labeled with volume fraction ratio r) samples. [a]: measurements made on unary samples lacking this particle population. [b]: unable to resolve second particle population. Error bars are the standard deviation from 10 independent runs. Stokes-Einstein diffusivities are 4.4 and 0.22 μm^2/s for small and large particles, respectively.

				Diffusion coefficient [μm^2/s]	
	Radius [nm]	**ϕ**	***q* [μm^{-1}]**	**D_S**	**D_L**
	50	10^{-3}		4.3 ± 0.1	[a]
***r* = φ_L/φ_S**	1,000	10^{-5}		[a]	0.20 ± 0.02
0.003	50	10^{-3}	6.8	3.8 ± 0.2	[b]
			11.2	4.1 ± 0.1	[b]
	1,000	3×10^{-6}	18.7	4.3 ± 0.1	[b]
0.01	50	10^{-3}	6.8	4.5 ± 0.4	[b]
			11.2	4.3 ± 0.1	[b]
	1,000	1×10^{-5}	18.7	4.5 ± 0.1	[b]
0.03	50	10^{-3}	6.8	4.9 ± 0.3	0.30 ± 0.05
			11.2	4.1 ± 0.3	[b]
	1,000	3×10^{-5}	18.7	4.1 ± 0.1	[b]

At the highest concentration of large particles and at the lowest wavevectors, the signal from the large particles dominates; the small particles still contribute to the intensity at lower volume fraction ratios and higher wavevectors. To capture the contributions from both particles, we globally fit all relaxations across the wavevector range to the sum of two single-exponential functions with a weighting function $f_s(q)$ to describe the relative contribution from each particle population. This fitting form has five fitting parameters at each wavevector: $\tau_s(q), \tau_L(q), A(q), B(q)$, and $f_s(q)$. To reduce the number of independent fitting parameters, we noted that the ratio of the decay rates of the large and small particles should be constant across the range of wavevectors, even as the relative scattering contribution from each was modulated by the anisotropic scattering of the particles. For bidisperse mixtures, we therefore implemented

a global fitting process and fit to the structure function, $\Delta(q;t) = A(q)\left[1 - \left(f_s(q)\exp\left(-\frac{t}{\tau_L(q)/f_r}\right) + f_L(q)\exp\left(-\frac{t}{\tau_L(q)}\right)\right)\right] + B(q)$, (4.5), where $\tau_L(q)$ is the relaxation time of 1 μm particles at the wavevector q; the weighting functions $f_s(q)$ and $f_L(q) = 1 - f_S(q)$ describe the contribution of small (50 nm) and large (1 μm) particles, respectively, to the scattering intensity at q; and f_r is the ratio of relaxation times of large and small particles, which is independent of q and hence was globally fit. Although the ratio f_r is known for these particles from the control experiments, *a priori* knowledge of the particle sizes is not required to use this functional form. This functional form exploits the full dynamic range of the DDM technique to generate a more robust non-linear fitting methodology and thereby accurately measure the diffusivities of both particles in a bidisperse mixture.

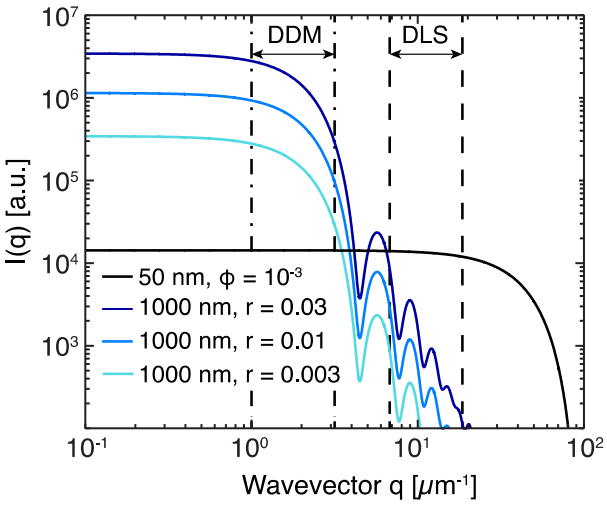

Figure 24.5. Predicted scattering intensity $I(q)$ for small particles at $\phi = 10^{-3}$ and large particles at volume fraction ratios of $r = 0.03$, 0.01, and 0.003 as a function of wavevector q using standard equations for hard spheres. The range of wavevectors probed by DLS and DDM are indicated by dashed and dash-dotted lines, respectively.

We obtained $f(q,t)$ for each wavevector from series of difference images.[117] In contrast to the intermediate scattering functions measured at higher angles using DLS, the DDM $f(q,t)$ clearly show non-exponential decays over 0.98 μm^{-1} < q < 3.01 μm^{-1} for all values of r

examined here (Fig. 23.5e – g). This q-range is narrower than that accessed by us in earlier measurements using similar equipment [193, 207, 216] and is limited by the dynamics of the particles relative to the rate of image acquisition. For q < 0.98 μm^{-1}, the upper plateau was not reached by the maximum lag time at which we obtained enough independent measurements for statistics, 35 s (2200 frames), which was set by the frame rate and camera buffer. For q > 3.01 μm^{-1}, the frame rate (63 fps) was insufficient to resolve the diffusive relaxation time scale of the smaller particles. Nonetheless, the data in Figure 23.5e – g indicate that DDM can resolve particle dynamics in a bidisperse mixture. The intermediate plateaus observed in the DDM intermediate scattering functions (Fig. 23.5e-g) resulted from the large particle size ratio ($\frac{a_L}{a_S} \approx 20$). When $\frac{a_L}{a_S} < 10$, the two relaxations will not be well separated. Instead, $f(q,t)$ will resemble a stretched exponential decay, characteristic of a dynamic process with a distribution of relaxation rates [207, 214]. Careful analysis of the residuals of a stretched exponential and a double exponential fit can distinguish between these decays.[217] For mixtures of particles of comparable size, the distribution of particle sizes will manifest as a polydispersity term, which can be captured by fitting a cumulant form to the intermediate scattering function.[117]

To confirm that DDM yields quantitative information on the dynamics of bidisperse mixtures, we examined the q-dependence of τ_L, which was not resolvable with DLS. The inverse of this time scale, τ_L^{-1}, scaled linearly with q^2 over the given range of wavevectors, indicating that the particle motion was diffusive (Fig. 26.5). Furthermore, the diffusion coefficient of the particles, extracted from the slope of a linear fit of τ_L^{-1} as a function of q^2, was in agreement with that obtained on a unary sample of large particles with DLS and with DDM. Finally, we compared relaxation times of the small particles $\tau_s = \tau_L / f_R$ extracted from the DDM fits on bidisperse suspensions to those obtained on unary suspensions in DLS. . Within fitting errors, we obtained

good agreement between the diffusion coefficients obtained in unary (control) and in bidisperse suspensions (Table 2.5). Thus, DDM accurately measures the dynamics of both particles in a bidisperse suspension, beyond the capabilities of DLS. This enhanced sensitivity of DDM arises because we study a small population of large scatterers in a suspension of smaller scatterers (a relevant limit for early-stage aggregation, as one example). In the opposite limit, where the small particles are the minority species in a bidispersed mixture, DLS would be a more sensitive technique because the scattering from the large population of large scatterers would overwhelm that from the small particles in DDM.

DDM signal generation in bidisperse suspensions

DDM is a heterodyne scattering method, in which the scattered light interferes with the transmitted light. The structural information extracted from heterodyne near field scattering depends on the sample-to-detector distance.[196] DDM, by contrast, accurately captures the dynamics of a sample regardless of the sample-to-detector distance[194] because the dynamic information is encoded in the time dependence of the intermediate scattering function rather than in the signal amplitude. In DDM, the signal amplitude $A(q)$ is the product of the optical transfer function, which depends on the imaging set up, and the scattering pattern of the particles [194]. For the bidisperse samples at *r* = 0.01 and 0.003, $A(q)$ was non-monotonic (Figure 27.5a). To investigate the origins of this non-monotonicity, we extracted the contributions to the DDM signal from the small and large particles (Fig. 27.5b,c) by multiplying $A(q)$ by the relative contributions $f_S(q)$ and $f_L(q)$, respectively. Whereas the intensity of the small particles decayed monotonically with increasing wavevector at all *r*, the intensity of the large particles exhibited non-monotonic oscillations at *r* = 0.01 and 0.003. Similar oscillations are seen in $I(q)$ for the large particles (Fig. 24.5), but at higher wavevectors than those probed with DDM; over the *q*-range probed by DDM, $I(q)$ of the large particles is predicted to decrease monotonically.

Thus, the oscillations in the DDM amplitude were not caused by the scattering intensity, but by the optical transfer function acting on the large particles.

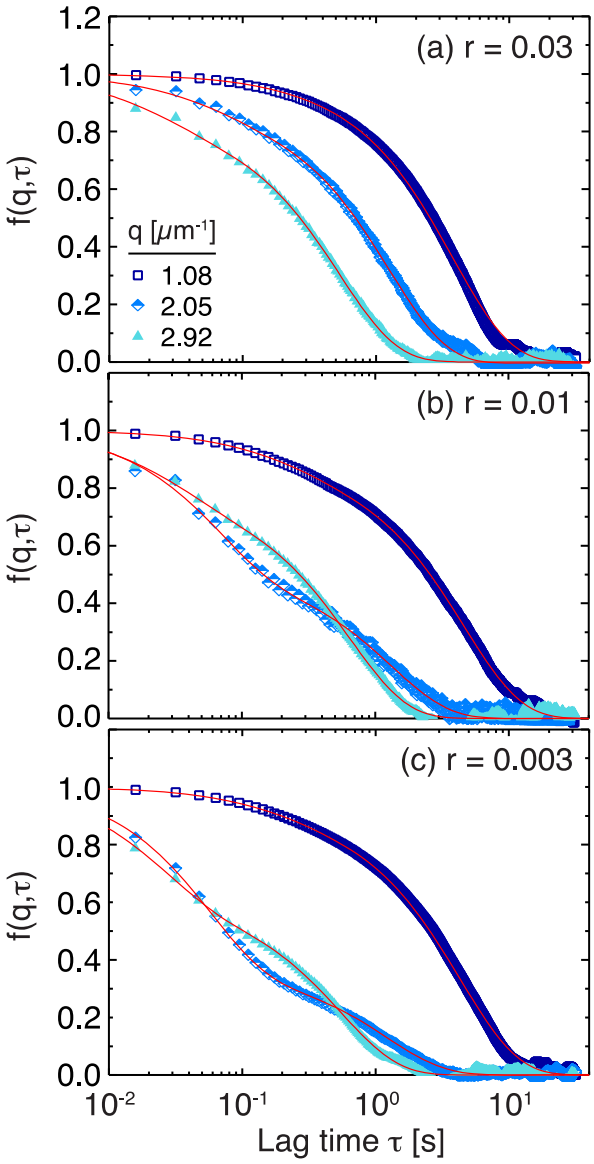

Figure 25.5. Intermediate scattering function $f(q,t)$, extracted from DDM measurements, as a function of lag time t measured for bidisperse mixtures of particles of diameter 100 nm and 2 μm formulated at large-to-small volume fraction ratios r of (a) 0.03, (b) 0.01, and (c) 0.003. For each ratio, data were analyzed over the wavevector range 0.98 μm^{-1} < q < 3.01 μm^{-1}; the figure shows representative correlation functions obtained for wavevectors q = 1.08 μm^{-1} (squares), 2.05 μm^{-1} (diamonds), or 2.92 μm^{-1} (triangles). Red lines indicate fits to eqn 3.5.

For monodisperse samples of small particles with $r/\lambda < 1$, the optical transfer function for the DDM signal decays exponentially with q with a rate set by a roll-off wavevector q_{ro}.[194]

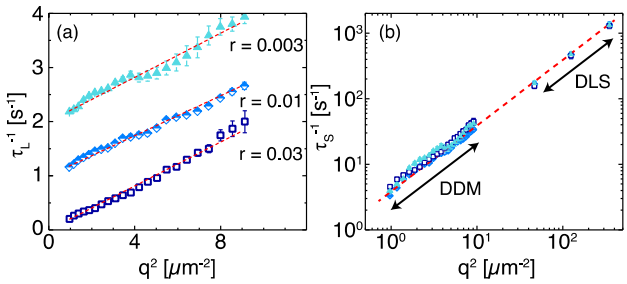

Figure 26.5. (a) Inverse of the large-particle time scale τ_L^{-1} as a function of the square of the wavevector q^2 for bidisperse mixtures of particles of radius 50 nm and 1 μm formulated at large-to-small volume fraction ratios r = 0.03 (squares), 0.01 (diamonds), and 0.003 (triangles). Data at r = 0.01 and r = 0.003 are offset by one and two unit increments on the y axis, respectively, for clarity. (b) Comparison of DLS and DDM inverse time scales for the small particles as a function of q^2. Data at low wavevectors are acquired in a bidisperse mixture using DDM; data at higher wavevectors are acquired in unary solutions using DLS. Dashed red lines in (a) and (b) indicate linear fits.

By contrast, large objects with $r/\lambda \gg 1$ act as phase objects, introducing oscillations to the optical transfer function and consequently to $A(q)$.[194, 212] To identify the positions of the non-monotonic oscillations in the large-particle signal, we examined the relative scattering intensity of the large particles $f_L(q)$ (Fig. 28.5).

Table 2.5 Diffusivities obtained from differential dynamic microscopy experiments for unary (top rows) and bidisperse (labeled with volume fraction ratio r) samples. [a]: measurements made on unary samples lacking this particle population. [b]: calculated from the experimentally-measured large-particle diffusivity using the globally-fit size ratio f_r. Error bars are numerical uncertainty from fitting functions. Stokes-Einstein diffusivities are 4.4 and 0.22 μm²/s for small and large particles, respectively.

			Diffusion coefficient [μm²/s]	
	Radius [nm]	**ϕ**	**D_S**	**D_L**
	50	10^{-3}	[a]	0.22 ± 0.01
***r* = φ_L/φ_s**	1,000	10^{-5}	4.1 ± 0.1	[a]
0.003	50	10^{-3}	4.3 ± 0.3 [b]	0.20 ± 0.01
	1,000	3×10^{-6}		
0.01	50	10^{-3}	4.0 ± 0.2 [b]	0.19 ± 0.01
	1,000	1×10^{-5}		
0.03	50	10^{-3}	4.4 ± 0.4 [b]	0.20 ± 0.01
	1,000	3×10^{-5}		

For $r = 0.03$ and 0.01, the primary minima occurred at $q^2 \approx 4$ μm^{-2} and for $r = 0.003$, at $q^2 \approx 5.5$ μm^{-2}. We attribute these minima to the interference patterns from the large particles present in the microscope images and in the series of difference images (Fig. 28.5b).

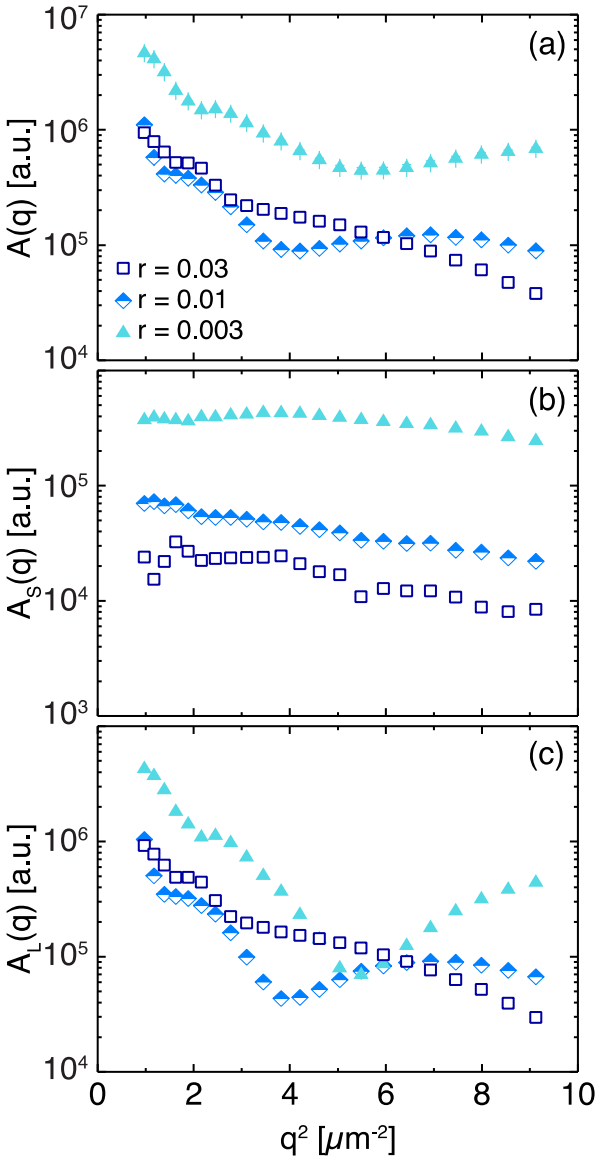

Figure 27.5 (a) DDM signal amplitude $A(q)$ as a function of wavevector squared q^2 for bidisperse mixtures of particles of radius 50 nm and 1 μm at varying volume fraction ratios r. (b) and (c) describe the contributions to signal intensity from small and large particles, $A_S(q)$ and $A_L(q)$, respectively.

In a heterodyne geometry, interference patterns are complex due to the presence of both scattered and transmitted fields. The best examples of interference patterns are holograms,[218-

221] in which the scattered field interferes with the transmitted light, and diffraction patterns,[222, 223] in which the scattered field interferes with itself. These patterns typically depend on the particle radius and the distance z between a particle and the image plane, which ideally can be resolved to 50 nm.[219, 222] The DDM algorithm, however, averages the scattering signal from multiple particles at varying axial positions. Additionally, the particles diffuse vertically and this motion changes the position of the rings over time.

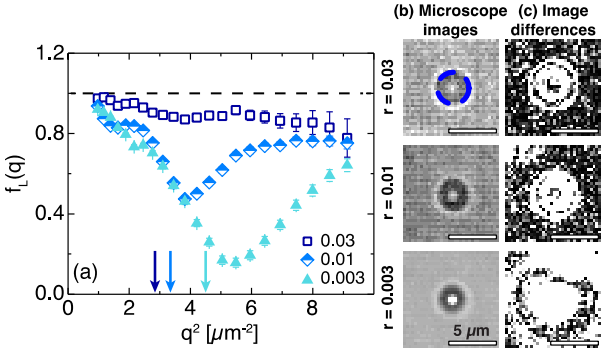

Figure 28.5. (a) Relative contribution to the DDM signal from the large particles $f_L(q)$ as a function of the square of the wavevector q^2. Arrows indicate predicted minima from diameter of diffraction rings. Examples of diffraction rings seen in (b) microscope images and (c) image differences at a lag time $\tau = 1.6$ s for each sample. Dashed circle indicates diameter of diffraction ring

Thus, the minima present in $f_L(q)$ are smeared without the ideal axial resolution of diffraction- or hologram-based particle tracking methods. Nevertheless, we compared the position of the minima $f_L(q_{\min})$ to the diameter $d = 2\pi/q_{\min}$ of the interference rings in the captured original images, calculated as the boundary between the dark ring and the outer light ring (dashed circle in Figure 28.6b). While we do not attempt to predict changes in the position of $f_L(q_{\min})$ between samples, the close agreement between the diameters of the rings and $f_L(q_{\min})$ (Table 3.5) suggests that it is the interference patterns that lead to the non-monotonic changes in the DDM signal intensity. This argument implies that $f_L(q_{\min})$ depends on particle size, incident wavelength, and distance of particles from focal plane but is in principle independent of particle concentration. To test this hypothesis, we performed a proof-of-concept experiment on

unary suspensions of large particles that were segregated via sedimentation to the bottom of the glass sample chamber. The particles remained diffusive on the glass surface, but hydrodynamic interactions with the surface reduced their diffusivity compared to that in the bulk. Focusing the lens at different distances z above the plane of the segregated particles, we controlled the distance between the particles and the image plane. The amplitude of the DDM signal $A(q)$ depended on the vertical position (Fig. 28.5c) and the locations of the minima corresponded nearly quantitatively with observed changes in the interference patterns (Fig. 28.5d). Thus, the amplitude $A(q)$ of the dynamic structure factor $\Delta(q;t)$ can, in principle, be used to extract information about the axial position of large particles, similar to diffraction-based[222] or holographic[218, 221] particle tracking methods in three dimensions. Although difficult to predict the interference patterns *a priori* due to the distribution of wavelengths and the spherical wavefront of the incident light in a DDM experiment, similar experiments could be performed at smaller height steps to calibrate the observed interference patterns. This calibration would allow determination of the height by matching the measured $A(q)$ to the calibrated $A(q)$. Future experiments could exploit a designed separation of time scales (by tuning particle size, solution viscosity, and/or density difference) to characterize multiple dynamic processes simultaneously. For example, in microgravity environments where sedimentation is minimal, experiments could separate aggregation[224] and conjugation[225] from the motion of individual particles. In terrestrial experiments, in-plane diffusion could be characterized with DDM, and sedimentation velocities could be calculated tracking the changes in $A(q)$ over a series of movies acquired over extended times.

Table 3.5. Measured diffraction pattern diameter and predicted q_{min} from microscope images. Error in ring diameter equivalent to $\pm$ 2 pixels. Error in q_{min} is equal to the q-resolution of DDM. Predicted height h between particle and focal plane.

$R = \varphi_L/\varphi_s$	Ring diameter d [μm]	Predicted $q_{\min} = 2\pi/d$ [μm^{-1}]	Actual $q_{\min}$ [μm^{-1}]	Predicted height $h = 1.22\, da/\lambda$ [μm]
0.003	3.0 ± 0.7	2.1 ± 0.5	2.3 ± 0.1	6.7 ± 1.6
0.01	3.5 ± 0.7	1.8 ± 0.4	2.0 ± 0.1	7.8 ± 1.6
0.03	3.7 ± 0.7	1.7 ± 0.3	2.0 ± 0.1	8.2 ± 1.6

Summary (Bidisperse suspensions in b-DDM)

We show that DDM can be used to obtain information about the dynamics of multiple constituents even at very dilute concentrations not detectable with DLS. In addition, DDM on bidisperse mixtures offers a new capability: inferring the axial position of the larger scatterers through physics similar to that underlying diffraction- and hologram-based particle tracking methods. We believe the ability to characterize both axial position and in-plane dynamics can be exploited to measure dynamics on different time scales, such as sedimentation velocity and diffusion. The simplicity of DDM, and the availability of compatible facilities on the ISS, indicates that this method can be applied to obtain dynamical information across a broad range of systems studied in microgravity. For example, ground-based studies use DDM to measure concentration fluctuations in binary[226] and ternary[227] fluid mixtures; hence this method can be readily applied to the wealth of image time-series data available from extant microgravity studies on similar systems.[228]

Future directions (p53)

Our study of p53 reveals the high tendency of this protein for fibrillar aggregation at higher temperatures. We also observed that crowding promotes aggregation of p53 into condensates that are initially distinct from fibrillar aggregates; moreover, these condensates halt the nucleation of fibrillar aggregates by slowing down the nucleation. This study raises two fundamental questions. First, how does Ficoll induce clustering of p53? What interactions are driving the p53 clustering? Which domains of p53 are involved? Second, a more fundamental question: does p53 phase separate inside the cell crowded environment and what are the implications of these dense liquid clusters for biological function of p53? To elucidate clustering mechanism of p53 in presence of Ficoll, a detailed study is required and the role of each domain of p53 should be mapped out. To gain information, we should investigate the role of disordered N- terminus (residues 1-92) in cluster formation of p53. By preparing a construct of deleted disordered domain (ΔN1-92, which lacks the N-terminus disordered domain) one can investigate the clustering behavior of ΔN1-92 [43, 44]. Now to test if the oligomerization domain drives the clustering or acts more as a catalyst, we should test the L344P p53 mutant that abolished the p53 tetramerization. In addition, simultaneous deletion of disordered domain and abolishment of tetramerization by L344P mutation (construct ΔN1-92-L344P) can allows us to map out respectively, the significance of disordered and oligomerization domain on p53 clustering. The previous study identifies which domains of p53 are involved in clustering of p53 [43]. These methods can also be applied to study a more fundamental question: what is the ability of p53 to phase separate in the cell crowded environment? By preparing a GFP-fused p53 construct (GFP-p53), we can investigate the formation of p53 dense liquid clusters inside the cells. If phase separation occurs we could track dense liquid droplets that appear as brighter spots compared to the uniformly distributed fluorescence. Furthermore, we can test how does post translational

modifications (PTMs) to p53, which are caused by stress, alter the p53 clustering. By addressing the significance of each p53 domain for clustering, now we can determine whether specific PTMs on that domain promote or reverse p53 phase separation. Furthermore, we can address how does phase-separated p53 function? Is the phase separation of p53 or PMT-p53 essential pathway to cell stress response? Does the phase separated p53 capture other proteins or nucleotides? We can investigate this by fusion of YFP or m-Cherry to Mdm2 or by tagging p53 downstream target genes such as BAX, P21, PUMA, and GADD with fluorophores and test for co-localization in p53 clusters. This study could potentially address if p53 phase separates in crowded environment of the cell and elucidate a detailed picture of how p53 clusters facilitate the right signaling and gene expression to recover stressed cells. In addition, we can characterize the in vitro and in vivo phase separation tendencies of different p53 mutants and ask if these clusters are essential for the mutant aggregation. We can correlate the tendency of the clustering to aggregation propensity by testing the mutant I254R p53, which is reported to abolish the aggregation of p53. We can further test if the mutant p53 co-localizes with the WT-p53 clusters, which could lead into exciting findings about loss/gain of function of p53 mutants [43]. Another question to answer is whether the oligomerization of p53 is at correlated with its aggregation. What if the oligomerization drives the p53 into phase separated clusters and unfolded monomeric p53 leaves the clusters and forms the fibrillar aggregates, similar to the mechanism proposed in 2001 for human TTR protein? To investigate this, we should compare the aggregation kinetics of L344P with WT-p53. Furthermore, we can employ high resolution silica-based size exclusion to purify the p53 tetramers from monomers and test aggregation of the protein at different ratio of monomer/tetramer fractions using the methods presented in this thesis. If, under intracellular conditions, p53 phase separates and the aggregates originate inside the mesoscopic clusters, we can target these dense liquid phases for drug delivery treatments to increase the efficacy of the process.

References

1. Hammarström, P., F. Schneider, and J.W. Kelly, "*Trans-Suppression of Misfolding in an Amyloid Disease"*. *Science*, 2001. **293**(5539): p. 2459-2462.
2. Glenner, G.G. and C.W. Wong, "*Alzheimer's disease: Initial report of the purification and characterization of a novel cerebrovascular amyloid protein*". *Biochemical and Biophysical Research Communications*, 1984. **120**(3): p. 885-890.
3. Seubert, P., *"Isolation and quantification of soluble Alzheimer's β-peptide from biological fluids*". *Nature*, 1992. **359**: p. 325.
4. Kelly, J.W., "Alternative conformations of amyloidogenic proteins govern their behavior." *Current Opinion in Structural Biology*, 1996. **6**(1): p. 11-17.
5. Ashton, L., "*Susceptibility of Different Proteins to Flow-Induced Conformational Changes Monitored with Raman Spectroscopy*". *Biophysical Journal*, 2010. **98**(4): p. 707-714.
6. McKinley, M.P., "*Scrapie prion rod formation in vitro requires both detergent extraction and limited proteolysis*". *Journal of Virology*, 1991. **65**(3): p. 1340-1351.
7. Prusiner , S.B., "*Neurodegenerative Diseases and Prions*". *New England Journal of Medicine*, 2001. **344**(20): p. 1516-1526.
8. Caughey, B., "*Transmissible spongiform encephalopathies, amyloidoses and yeast prions: Common threads*"*? Nature Medicine*, 2000. **6**: p. 751.
9. Sacchettini, J.C. and J.W. Kelly, "*Therapeutic strategies for human amyloid diseases." Nature Reviews Drug Discovery*, 2002. **1**: p. 267.
10. Dobson, C.M., "*Principles of protein folding, misfolding and aggregation*." *Seminars in Cell & Developmental Biology*, 2004. **15**(1): p. 3-16.
11. Dobson, C.M., "*Protein misfolding, evolution and disease.*" *Trends in Biochemical Sciences*, 1999. **24**(9): p. 329-332.

12. Sunde, M., Serpell, LC., Bartlam, M., Fraser, PE., Pepys, MB., and Blake, CC., "*Common core structure of amyloid fibrils by synchrotron X-ray diffraction"Edited by F. E. Cohen. Journal of Molecular Biology*, 1997. **273**(3): p. 729-739.

13. Pauling, L. and R.B. Corey, *"Configurations of Polypeptide Chains With Favored Orientations Around Single Bonds: Two New Pleated Sheets." Proceedings of the National Academy of Sciences of the United States of America*, 1951. **37**(11): p. 729-740.

14. Kirschner, D.A., C. Abraham, and D.J. Selkoe, "*X-ray diffraction from intraneuronal paired helical filaments and extraneuronal amyloid fibers in Alzheimer disease indicates cross-beta conformation." Proceedings of the National Academy of Sciences*, 1986. **83**(2): p. 503-507.

15. Morimoto, R.I., *"Proteotoxic stress and inducible chaperone networks in neurodegenerative disease and aging." Genes & Development*, 2008. **22**(11): p. 1427-1438.

16. Hartl, F.U., A. Bracher, and M. Hayer-Hartl, *"Molecular chaperones in protein folding and proteostasis." Nature*, 2011. **475**: p. 324.

17. Balch, WE., Morimoto RI., Dillin A., Kelly JW., *"Adapting Proteostasis for Disease Intervention." Science*, 2008. **319**(5865): p. 916-919.

18. Lansbury, P.T. and H.A. Lashuel, *"A century-old debate on protein aggregation and neurodegeneration enters the clinic." Nature*, 2006. **443**: p. 774.

19. Bishop, N.A. and L. Guarente, *"Two neurons mediate diet-restriction-induced longevity in C. elegans." Nature*, 2007. **447**: p. 545.

20. Olzscha, H., Schermann, SM., Woerner, AC., Pinkert, S., Hecht, MH., Tartaglia, GG., Vendruscolo, M., Hayer-Hartl, M., Hartl, FU., Vabulas, RM., *"Amyloid-like Aggregates Sequester Numerous Metastable Proteins with Essential Cellular Functions." Cell*, 2011. **144**(1): p. 67-78.

21. Arndt, V., Dick, N., Tawo, R., Dreiseidler, M., Wenzel, D., Hesse, M., Fürst, D., Saftig P., Saint, R., Fleischmann, BK., Hoch, M., Höhfeld, J., *"Chaperone-Assisted Selective Autophagy Is Essential for Muscle Maintenance." Current Biology*, 2010. **20**(2): p. 143-148.

22. Crews, L. and E. Masliah*, "Molecular mechanisms of neurodegeneration in Alzheimer's disease." Human Molecular Genetics*, 2010. **19**(R1): p. R12-R20.

23. Niedowicz, D.M., P.T. Nelson, and M.P. Murphy, *"Alzheimer's Disease: Pathological Mechanisms and Recent Insights." Current Neuropharmacology*, 2011. **9**(4): p. 674-684.

24. LIN, H., R. BHATIA, and R. LAL, *"Amyloid β protein forms ion channels: implications for Alzheimer's disease pathophysiology." The FASEB Journal*, 2001. **15**(13): p. 2433-2444.

25. Shankar, GM., Bloodgood, BL., Townsend, M., Walsh, DM., Selkoe, DJ., Sabatini, BL., *"Natural Oligomers of the Alzheimer Amyloid-β Protein Induce Reversible Synapse Loss by Modulating an NMDA-Type Glutamate Receptor-Dependent Signaling Pathway." The Journal of Neuroscience*, 2007. **27**(11): p. 2866-2875.

26. M. Pitschke, R. Prior, M. Haupt, and D. Riesner, *"Detection of single amyloid [beta]-protein aggregates in the cerebrospinal fluid of Alzheimer's patients by fluorescence correlation spectroscopy." Nat Med*, 1998. **4**(7): p. 832-834.

27. Haass, C. and D.J. Selkoe, *"Soluble protein oligomers in neurodegeneration: lessons from the Alzheimer's amyloid [beta]-peptide." Nat Rev Mol Cell Biol*, 2007. **8**(2): p. 101-112.

28. Broersen, K., F. Rousseau, and J. Schymkowitz, *"The culprit behind amyloid beta peptide related neurotoxicity in Alzheimer's disease: oligomer size or conformation?" Alzheimer's Research & Therapy*, 2010. **2**(4): p. 12-12.

29. Ehud, C., Jan, B., Rhonda, M., Perciavalle, J., Kelly, W. , Dillin, A., *"Opposing Activities Protect Against Age-Onset Proteotoxicity." Science*, 2006. **313**(5793): p. 1604-1610.

30. Bartolini, M., Bertucci, C., Bolognesi, ML., Cavalli, A., Melchiorre C., Andrisano V., *"Insight Into the Kinetic of Amyloid β (1–42) Peptide Self-Aggregation: Elucidation of Inhibitors' Mechanism of Action." ChemBioChem*, 2007. **8**(17): p. 2152-2161.

31. Sakono, M. and T. Zako, *"Amyloid oligomers: formation and toxicity of Aβ oligomers." FEBS Journal*, 2010. **277**(6): p. 1348-1358.

32. Shankar, G.,Li, S.,Mehta, T.,Garcia-Munoz, A.,Shepardson, N.,Smith, I.,Brett, F.,Farrell, M., Rowan, M.,Lemere, C.,Regan, C.,Walsh, D., Sabatini, B.,Selkoe, D., *"Amyloid-[beta] protein dimers isolated directly from Alzheimer's brains impair synaptic plasticity and memory." Nat Med*, 2008. **14**(8): p. 837-842.

33. Ross, C.A. and S.J. Tabrizi, *"Huntington's disease: from molecular pathogenesis to clinical treatment." The Lancet Neurology*, 2011. **10**(1): p. 83-98.

34. Gidalevitz T, Ben-Zvi A, Ho KH, Brignull HR, Morimoto RI., *"Progressive Disruption of Cellular Protein Folding in Models of Polyglutamine Diseases." Science*, 2006. **311**(5766): p. 1471-1474.

35. Li W, Serpell LC, Carter WJ, Rubinsztein DC, Huntington JA*., "Expression and Characterization of Full-length Human Huntingtin, an Elongated HEAT Repeat Protein." Journal of Biological Chemistry*, 2006. **281**(23): p. 15916-15922.

36. Yanai, A., Huang, K,. Kang, R., Singaraja, R., Arstikaitis, P., Gan, L., Orban, P.C., Mullard, A., Cowan, C., Raymond, L., Drisdel, R., Green, W., Ravikumar, B., Rubinsztein, D., Husseini, A., Hayden, M., *"Palmitoylation of huntingtin by HIP14is essential for its trafficking and function." Nature Neuroscience*, 2006. **9**: p. 824.

37. Miller J, Arrasate M, Brooks E, Libeu CP, Legleiter J, Hatters D, Curtis J, Cheung K, Krishnan P, Mitra S, Widjaja K, Shaby BA, Lotz GP, Newhouse Y, Mitchell EJ, Osmand A, Gray M, Thulasiramin V, Saudou F, Segal M, Yang XW, Masliah E, Thompson LM, Muchowski PJ,

Weisgraber KH, Finkbeiner S. *"Identifying polyglutamine protein species in situ that best predict neurodegeneration." Nature Chemical Biology*, 2011. **7**(12): p. 925-934.

38. Thakur, A.K. and R. Wetzel, *"Mutational analysis of the structural organization of polyglutamine aggregates." Proceedings of the National Academy of Sciences*, 2002. **99**(26): p. 17014-17019.

39. Poirier, M.A., H. Jiang, and C.A. Ross, *"A structure-based analysis of huntingtin mutant polyglutamine aggregation and toxicity: evidence for a compact beta-sheet structure." Human Molecular Genetics*, 2005. **14**(6): p. 765-774.

40. Pearce MM, Spartz EJ, Hong W, Luo L, Kopito RR., "*Prion-like transmission of neuronal huntingtin aggregates to phagocytic glia in the Drosophila brain*." *Nature Communications*, 2015. **6**: p. 6768.

41. Ross, C.A. and M.A. Poirier, "*Protein aggregation and neurodegenerative disease*." *Nature Medicine*, 2004. **10**: p. S10.

42. Jerson L.Silva,Claudia V. De MouraGallo, Danielly C.F.Costa, Luciana P.Rangel, "*Prion-like aggregation of mutant p53 in cancer*." *Trends in Biochemical Sciences*, 2014. **39**(6): p. 260-267.

43. Xu, J., Reumers, J.,Couceiro, J.,Smet, F.,Gallardo R.,Rudyak, S., Cornelis, A.,Rozenski, J., Zwolinska, A., Marine, J.,Lambrechts, D.,Suh, Y.,Rousseau, F.,Schymkowitz, J., "*Gain of function of mutant p53 by coaggregation with multiple tumor suppressors.*" *Nature Chemical Biology*, 2011. **7**(5): p. 285-295.

44. Bullock, A.N. and A.R. Fersht, "*Rescuing the function of mutant p53*." *Nature Reviews Cancer*, 2001. **1**: p. 68.

45. Oren, M. and V. Rotter, "*Mutant p53 Gain-of-Function in Cancer*." *Cold Spring Harbor Perspectives in Biology*, 2010. **2**(2): p. a001107.

46. Kim, M.P., Y. Zhang, and G. Lozano, "*Mutant p53: multiple mechanisms define biologic activity in cancer*." *Frontiers in Oncology*, 2015. **5**.

47. Muller, P.A.J., K.H. Vousden, and J.C. Norman, "*p53 and its mutants in tumor cell migration and invasion.*" *The Journal of Cell Biology*, 2011. **192**(2): p. 209-218.

48. van Oijen, M.G.C.T. and P.J. Slootweg, "*Gain-of-Function Mutations in the Tumor Suppressor Gene p53 .*" *Clinical Cancer Research*, 2000. **6**(6): p. 2138-2145.

49. Carnero, A., Hudson, J., Hannon, G., Beach, G., "*Loss-of-function genetics in mammalian cells: the p53 tumor suppressor model.*"*Nucleic Acids Research*, 2000. **28**(11): p. 2234-2241.

50. Muller, P.A.J. and K.H. Vousden, "*p53 mutations in cancer.*"*Nature Cell Biology*, 2013. **15**.

51. Marin MC, Jost CA, Brooks LA, Irwin MS, O'Nions J, Tidy JA, James N, McGregor JM, Harwood CA, Yulug IG, Vousden KH, Allday MJ, Gusterson B, Ikawa S, Hinds PW, Crook T, Kaelin WG Jr., "*A common polymorphism acts as an intragenic modifier of mutant p53 behaviour*." *Nature Genetics*, 2000. **25**: p. 47.

52. Xu, J., Reumers, J.,Couceiro, J.,Smet, F.,Gallardo R.,Rudyak, S., Cornelis, A.,Rozenski, J., Zwolinska, A., Marine, J.,Lambrechts, D.,Suh, Y.,Rousseau, F.,Schymkowitz, J., "*Gain of function of mutant p53 by coaggregation with multiple tumor suppressors.*" *Nature Chemical Biology*, 2011. **7**(5): p. 285-295.

53. Joerger, A.C. and A.R. Fersht, "*Structural Biology of the Tumor Suppressor p53.*" *Annual Review of Biochemistry*, 2008. **77**(1): p. 557-582.

54. Bieging, K.T., S.S. Mello, and L.D. Attardi, "*Unravelling mechanisms of p53-mediated tumour suppression*." *Nat Rev Cancer*, 2014. **14**(5): p. 359-370.

55. Carter S, Bischof O, Dejean A, Vousden KH., "*C-terminal modifications regulate MDM2 dissociation and nuclear export of p53.*" *Nature Cell Biology*, 2007. **9**(4): p. 428+.

56. Sykes SM, Mellert HS, Holbert MA, Li K, Marmorstein R, Lane WS, McMahon SB. *"Acetylation of the p53 DNA-Binding Domain Regulates Apoptosis Induction." Molecular Cell*, 2006. **24**(6): p. 841-851.

57. Joerger, A.C. and A.R. Fersht, "*The Tumor Suppressor p53: From Structures to Drug Discovery.*" *Cold Spring Harbor Perspectives in Biology*, 2010. **2**(6): p. a000919.

58. Adorno M, Cordenonsi M, Montagner M, Dupont S, Wong C, Hann B, Solari A, Bobisse S, Rondina MB, Guzzardo V, Parenti AR, Rosato A, Bicciato S, Balmain A, Piccolo S., "*A Mutant-p53/Smad Complex Opposes p63 to Empower TGFβ-Induced Metastasis.*" *Cell*, 2009. **137**(1): p. 87-98.

59. Ano, B., Rangel, L., Costa, D., Oliveira, G., Sanches,Braga A., Gava L.,Ramos, C.,Cepeda, A., Stumbo, A., Gallo, C.,Cordeiro, Y.,Silva, J., "*Mutant p53 Aggregates into Prion-like Amyloid Oligomers and Fibrils: IMPLICATIONS FOR CANCER.*" *The Journal of Biological Chemistry*, 2012. **287**(33): p. 28152-28162.

60. Vousden, K.H. and C. Prives, "*Blinded by the Light: The Growing Complexity of p53.*" *Cell*, 2009. **137**(3): p. 413-431.

61. Pellarin, R. and A. Caflisch, "*Interpreting the Aggregation Kinetics of Amyloid Peptides*." *Journal of Molecular Biology*, 2006. **360**(4): p. 882-892.

62. Auer, S., P. Ricchiuto, D. Kashchiev, "*Two-Step Nucleation of Amyloid Fibrils: Omnipresent or Not?*" *Journal of Molecular Biology*, 2012. **422**(5): p. 723-730.

63. Li, Y., V. Lubchenko, and P.G. Vekilov, "*The use of dynamic light scattering and Brownian microscopy to characterize protein aggregation*." *Review of Scientific Instruments,* 2011. **82**(5): p. -.

64. Frare, E.,Polverino, P.,Zurdo, J.,Dobson, C.,Fontana, A., *"A Highly Amyloidogenic Region of Hen Lysozyme.*" *Journal of Molecular Biology*, 2004. **340**(5): p. 1153-1165.

65. Vekilov, P.G. and M.A. Vorontsova, "*Nucleation precursors in protein crystallization.*" *Acta Crystallographica Section F*, 2014. **70**(3): p. 271-282.

66. Oleg, G., Pan, W., Katsonis, P.,Neumaier, N.,Weinkauf, S.,Vekilov, P.G., "*Metastable Liquid Clusters in Super- and Undersaturated Protein Solutions.*" *The Journal of Physical Chemistry B*, 2007. **111**(12): p. 3106-3114.

67. Galkin, O.,Pan, W.,Filobelo, L.,Hirsch, R.,Nagel, R.,Vekilov, P.G., "*Two-Step Mechanism of Homogeneous Nucleation of Sickle Cell Hemoglobin Polymers*." *Biophysical Journal*, 2007. **93**(3): p. 902-913.

68. Galkin, O. and P.G. Vekilov, "*Control of protein crystal nucleation around the metastable liquid–liquid phase boundary*." *Proceedings of the National Academy of Sciences*, 2000. **97**(12): p. 6277-6281.

69. Vorontsova, M.A., D. Maes, and P.G. Vekilov, "*Recent advances in the understanding of two-step nucleation of protein crystals.*" *Faraday Discussions*, 2015. **179**(0): p. 27-40.

70. Vekilov, P.G., "*Dense Liquid Precursor for the Nucleation of Ordered Solid Phases from Solution.*" *Crystal Growth & Design*, 2004. **4**(4): p. 671-685.

71. Galkin, O. and P.G. Vekilov, "*Mechanisms of Homogeneous Nucleation of Polymers of Sickle Cell Anemia Hemoglobin in Deoxy State.*" *Journal of Molecular Biology*, 2004. **336**(1): p. 43-59.

72. Pan, W., P.G. Vekilov, and V. Lubchenko, "*Origin of Anomalous Mesoscopic Phases in Protein Solutions.*" *The Journal of Physical Chemistry B*, 2010. **114**(22): p. 7620-7630.

73. Pan, W., A.B. Kolomeisky, and P.G. Vekilov, "*Nucleation of ordered solid phases of proteins via a disordered high-density state: Phenomenological approach." The Journal of Chemical Physics*, 2005. **122**(17): p. -.

74. Pan, W.,Galkin, O.,Filobelo, L.,Nagel, R.,Vekilov, P.G., *"Metastable Mesoscopic Clusters in Solutions of Sickle-Cell Hemoglobin." Biophysical Journal*, 2007. **92**(1): p. 267-277.

75. Li, Y.,Lubchenko, V.,Vorontsova, M.,Filobelo, M.,Vekilov, P.G.,"*Ostwald-Like Ripening of the Anomalous Mesoscopic Clusters in Protein Solutions.*" *The Journal of Physical Chemistry B*, 2012. **116**(35): p. 10657-10664.

76. Sleutel, M. and A.E.S. Van Driessche, "*Role of clusters in nonclassical nucleation and growth of protein crystals." Proceedings of the National Academy of Sciences*, 2014. **111**(5): p. E546-E553.

77. Yamazaki, Y.T,Kimura, Y.,Vekilov, P.G.,Furukawa, E.,Shirai, M.,Matsumoto, M., Van Driessche, A.V.,Tsukamoto, K., "*Two types of amorphous protein particles facilitate crystal nucleation.*" *Proceedings of the National Academy of Sciences*, 2017. **114**(9): p. 2154-2159.

78. Maes, D.,Vorontsova, M., Potenza, M., Sanvito, T.,Sleutel, M.,Giglio, M.,Vekilov, P.G., "*Do protein crystals nucleate within dense liquid clusters?" Acta Crystallographica. Section F, Structural Biology Communications*, 2015. **71**(Pt 7): p. 815-822.

79. Krishnan, R. and S.L. Lindquist, "*Structural insights into a yeast prion illuminate nucleation and strain diversity.*" *Nature*, 2005. **435**: p. 765.

80. Luiken, J.A. and P.G. Bolh*uis, "Prediction of a stable associated liquid of short amyloidogenic peptides*." *Physical Chemistry Chemical Physics*, 2015. **17**(16): p. 10556-10567.

81. Gibbs, J.W., "*On the equilibrium of heterogeneous substances." American Journal of Science*, 1878. **Series 3 Vol. 16**(96): p. 441-458.

82. Pruppacher, H.R., J.D. Klett, and P.K. Wang, *"Microphysics of Clouds and Precipitation." Aerosol Science and Technology*, 1998. **28**(4): p. 381-382.

83. Gliko, O., "*A Metastable Prerequisite for the Growth of Lumazine Synthase Crystals*." *Journal of the American Chemical Society*, 2005. **127**(10): p. 3433-3438.

84. Ashton, L.,"*Shear-Induced Unfolding of Lysozyme Monitored In Situ.*" *Biophysical Journal*, 2009. **96**(10): p. 4231-4236.

85. Asano, K., "*Crystal growth of ribonuclease S under microgravity.*" *Journal of Crystal Growth*, 1992. **122**(1–4): p. 323-329.

86. Borgstahl GE, V.-F.A., Lovelace J, Bellamy HD, Snell EH, *"A test of macromolecular crystallization in microgravity: large well ordered." insulin crystals* 2001.

87. Cerbino, R. and V. Trappe, "*Differential Dynamic Microscopy: Probing Wave Vector Dependent Dynamics with a Microscope.*" *Physical Review Letters*, 2008. **100**(18): p. 188102.

88. Fabio Giavazzi, D.B., . Veronique Trappe,. Tommaso Bellini,. Roberto Cerbino, "*Scattering information obtained by optical microscopy: Differential dynamic microscopy and beyond.*" *Physical Review Letters*, 2009. **100**(18): p. 188102.

89. Roberto Cerbino, V.T., "*Differential Dynamic Microscopy: Probing Wave Vector Dependent Dynamics with a Microscope.", Physical Review Letters*, 2008. **100**(18): p. 188102.

90. Wilson, L.G., "*Differential Dynamic Microscopy of Bacterial Motility." Physical Review Letters, 2011.* ***106****(1):* p. 018101.

91. Galkin, O. and P.G. Vekilov, *"Are Nucleation Kinetics of Protein Crystals Similar to Those of Liquid Droplets?" Journal of the American Chemical Society*, 2000. **122**(1): p. 156-163.

92. Vorontsova, M.A., P.G. Vekilov, and D. Maes, "*Characterization of the diffusive dynamics of particles with time-dependent asymmetric microscopy intensity profiles." Soft Matter*, 2016. **12**(33): p. 6926-6936.

93. Gill, S.C. and P.H. von Hippel, *"Calculation of protein extinction coefficients from amino acid sequence data*." *Analytical Biochemistry*, 1989. **182**(2): p. 319-326.

94. Biancalana, M. and S. Koide, "*Molecular Mechanism of Thioflavin-T Binding to Amyloid Fibrils." Biochimica et biophysica acta*, 2010. **1804**(7): p. 1405-1412.

95. Hawe, A., M. Sutter, and W. Jiskoot, "*Extrinsic Fluorescent Dyes as Tools for Protein Characterization." Pharmaceutical Research*, 2008. **25**(7): p. 1487-1499.

96. Khurana, R., *"Mechanism of thioflavin T binding to amyloid fibrils." Journal of Structural Biology*, 2005. **151**(3): p. 229-238.

97. Stryer, L., *"The interaction of a naphthalene dye with apomyoglobin and apohemoglobin: A fluorescent probe of non-polar binding sites." Journal of Molecular Biology*, 1965. **13**(2): p. 482-495.

98. Vassar, P.S. and C.F. Culling, *"Fluorescent stains, with special reference to amyloid and connective tissues." Archives of pathology*, 1959. **68**: p. 487-498.

99. Dombkowski, A.A., K.Z. Sultana, and D.B. Craig, *"Protein disulfide engineering." FEBS Letters*, 2014. **588**(2): p. 206-212.

100. Yang, M., C. Dutta, and A. Tiwari, *"Disulfide-Bond Scrambling Promotes Amorphous Aggregates in Lysozyme and Bovine Serum Albumin." The Journal of Physical Chemistry B*, 2015. **119**(10): p. 3969-3981.

101. Guez, V., *"Role of individual disulfide bonds in hen lysozyme early folding steps.*" *Protein Science : A Publication of the Protein Society*, 2002. **11**(5): p. 1136-1151.

102. Burns, J.A., "*Selective reduction of disulfides by tris(2-carboxyethyl)phosphine." The Journal of Organic Chemistry,* 1991. **56**(8): p. 2648-2650.

103. Ellman, G.L., *"Tissue sulfhydryl groups." Archives of Biochemistry and Biophysics,* 1959. **82**(1): p. 70-77.

104. Riener, C.K., G. Kada, and H.J. Gruber*, "Quick measurement of protein sulfhydryls with Ellman's reagent and with 4,4′-dithiodipyridine." Analytical and Bioanalytical Chemistry*, 2002. **373**(4): p. 266-276.

105. Riddles, P.W., R.L. Blakeley, and B. Zerner, *"Ellman's reagent: 5,5′-dithiobis(2-nitrobenzoic acid)—a reexamination." Analytical Biochemistry*, 1979. **94**(1): p. 75-81.

106. Frare, E., *"Characterization of Oligomeric Species on the Aggregation Pathway of Human Lysozyme." Journal of Molecular Biology*, 2009. **387**(1): p. 17-27.

107. Shugar, D., *"The measurement of lysozyme activity and the ultra-violet inactivation of lysozyme". Biochimica et biophysica acta*, 1952. **8**(3): p. 302-309.

108. Maes, D., "*Do protein crystals nucleate within dense liquid clusters?" Acta Crystallographica Section F,* 2015. **71**(7): p. 815-822.

109. Li, Y., V. Lubchenko, and P.G. Vekilov*, "The Use of Dynamic Light Scattering and Brownian Microscopy to Characterize Protein Aggregation." Rev. Sci. Instrum.*, 2011. **82**: p. 053106

110. Filipe, V., A. Hawe, and W. Jiskoot, *"Critical Evaluation of Nanoparticle Tracking Analysis (NTA) by NanoSight for the Measurement of Nanoparticles and Protein Aggregates." Pharmaceutical Research*, 2010. **27**(5): p. 796-810.

111. Pan, W., *"Metastable mesoscopic clusters in solutions of sickle cell hemoglobin." Biophys. J., 2007*. **92**(1): p. 267-277.

112. Vorontsova, M.A*., "Lack of Dependence of the Sizes of the Mesoscopic Protein Clusters on Electrostatics." Biophysical Journal*, 2015. **109**(9): p. 1959-1968.

113. Byington, M.C. *"Protein Conformational Flexibility Enables the Formation of Dense Liquid Clusters: Tests Using Solution Shear."* *The Journal of Physical Chemistry Letters*, 2016. **7**: p. 2339-2345.

114. Kayed, R., *"Common Structure of Soluble Amyloid Oligomers Implies Common Mechanism of Pathogenesis." Science*, 2003. **300**(5618): p. 486-489.

115. Canet, D., *"Local cooperativity in the unfolding of an amyloidogenic variant of human lysozyme." Nat Struct Mol Biol*, 2002. **9**(4): p. 308-315.

116. Fändrich, M., *"Oligomeric Intermediates in Amyloid Formation: Structure Determination and Mechanisms of Toxicity." Journal of Molecular Biology*, 2012. **421**(4–5): p. 427-440.

117. Safari, M.S., *"Differential dynamic microscopy of weakly scattering and polydisperse protein-rich clusters.*" *Physical Review E*, 2015. **92**(4): p. 042712.

118. Ford, N.C*., "Biochemical applications of laser Rayleigh-scattering." Chemica Scripta*, 1972. **2**(5): p. 193.

119. Chen, F.C. *"Experimental evaluation of macromolecular polydispersity in intensity correlation spectrodcopy using the cumulant expansion technique." The Journal of Chemical Physics*, 1974. **60**(4): p. 1675-1676.

120. Chaikin, P.M. and T.C. Lubensky, *"Principles of condensed matter physics"* 1995, *Cambridge*: Cambridge Unversity Press.

121. Gliko, O., *"A metastable prerequisite for the growth of lumazine synthase crystals." J. Amer. Chem. Soc.*, 2005. **127**: p. 3433-3438.

122. Pan, W., P.G. Vekilov, and V. Lubchenko, *"The origin of anomalous mesoscopic phases in protein solutions.*" *J. Phys. Chem. B*, 2010. **114** p. 7620-7630.

123. Gliko, O., *"Metastable liquid clusters in super- and undersaturated protein solutions." J. Phys. Chem. B*, 2007. **111**(12): p. 3106-3114.

124. Sleutel, M. and A.E. Van Driessche, *"Role of clusters in nonclassical nucleation and growth of protein crystals." Proceedings of the National Academy of Sciences of the United States of America*, 2014. **111**(5): p. E546-53.

125. Schubert, R., , *"Real-Time Observation of Protein Dense Liquid Cluster Evolution during Nucleation in Protein Crystallization." Crystal Growth & Design*, 2017. **17**(3): p. 954-958.

126. Yamazaki, T., *"Two types of amorphous protein particles facilitate crystal nucleation." Proceedings of the National Academy of Sciences*, 2017. **114**: p. 2154-2159.

127. Kolomeisky, A.B., *"Staying Together: Protein Molecules in Mesoscopic Clusters." Biophysical Journal*, 2015. **109**(9): p. 1759-1760.

128. Elcock, A.H. and J.A. McCammon, *"Identification of protein oligomerization states by analysis of interface conservation." Proceedings of the National Academy of Sciences*, 2001. **98**(6): p. 2990-2994.

129. Elcock, A.H., D. Sept, and J.A. McCammon, *"Computer Simulation of Protein−Protein Interactions." The Journal of Physical Chemistry B*, 2001. **105**(8): p. 1504-1518.

130. Elcock, A.H. and J.A. McCammon, *"Calculation of Weak Protein-Protein Interactions: The pH Dependence of the Second Virial Coefficient." Biophysical Journa*l, 2001. **80**(2): p. 613-625.

131. Chan, Ho Y.,*"Anisotropy of the Coulomb Interaction between Folded Proteins: Consequences for Mesoscopic Aggregation of Lysozyme." Biophysical Journa*l, 2012. **102**(8): p. 1934-1943.

132. Hill, S.E., "*Amyloid Protofibrils of Lysozyme Nucleate and Grow Via Oligomer Fusion." Biophysical Journal*, 2009. **96**(9): p. 3781-3790.

133. Hill, S.E., T. Richmond, and M.M. Muschol, *"Denatured-State Conformation As Regulator of Amyloid Assembly Pathways?" Biophysical Journal*, 2010. **98**(3): p. 17a-17a.

134. Hill, S.E., *"Spatial Extent of Charge Repulsion Regulates Assembly Pathways for Lysozyme Amyloid Fibrils." Plos One*, 2011. **6**(4).

135. Muschol, M., *"Structural Evolution of Oligomeric Vs. Oligomer-Free Amyloid Fibril Growth." Biophysical Journal*, 2013. **104**(2): p. 49a-49a.

136. Krieger, E. and G. Vriend, *"New ways to boost molecular dynamics simulations." Journal of Computational Chemistry*, 2015. **36**(13): p. 996-1007.

137. Crosas, E., *"Uridine as a new scavenger for synchrotron-based structural biology techniques." Journal of Synchrotron Radiation*, 2017. **24**(1): p. 53-62.

138. Ibrahim, H.R., T. Matsuzaki, and T. Aoki*, "Genetic evidence that antibacterial activity of lysozyme is independent of its catalytic function." Febs Letters*, 2001. **506**(1): p. 27-32.

139. McCammon, J.A., *"The Hinge-Bending Mode of Lysozyme." Nature* 1976. **262**: p. 325-326.

140. Arnaudov, L.N. and R. de Vries, *"Thermally Induced Fibrillar Aggregation of Hen Egg White Lysozyme." Biophysical Journal*, 2005. **88**(1): p. 515-526.

141. Gasymov, O.K. and B.J. Glasgow, *"ANS Fluorescence: Potential to Augment the Identification of the External Binding Sites of Proteins." Biochimica et biophysica acta*, 2007. **1774**(3): p. 403-411.

142. Persichilli, C., *"Does Thioflavin-T Detect Oligomers Formed During Amyloid Fibril Assembly." Biophysical Journal*, 2011. **100**(3): p. 538-538.

143. Ackerson, B.J., *"Correlations for Interacting Brownian Particles." Journal of Chemical Physics*, 1978. **69**(2): p. 684-690.

144. Muschol, M. and F. Rosenberger*, "Interaction in undersaturated and supersaturated lysozyme solutions: static and dynamic light scattering results." J. Chem. Phys.*, 1995. **103**: p. 10424-10432.

145. Cabriolu, R. and S. Auer, *"Amyloid Fibrillation Kinetics: Insight from Atomistic Nucleation Theory.*" *Journal of Molecular Biology*, 2011. **411**(1): p. 275-285.

146. Buell, A.K., *"Population of Nonnative States of Lysozyme Variants Drives Amyloid Fibril Formation." Journal of the American Chemical Society*, 2011. **133**(20): p. 7737-7743.

147. Mossuto, M.F., "*The Non-Core Regions of Human Lysozyme Amyloid Fibrils Influence Cytotoxicity." Journal of Molecular Biology*, 2010. **402**(5): p. 783-796.

148. Kato, G.J., *"Sickle cell disease."* *Nature Reviews Disease Primers*, 2018. **4**: p. 18010.

149. Knowles, T.P.J., M. Vendruscolo, and C.M. Dobson, *"The amyloid state and its association with protein misfolding diseases." Nature Reviews Molecular Cell Biology*, 2014. **15**: p. 384.

150. Aguzzi, A. and T. O'Connor, *"Protein aggregation diseases: pathogenicity and therapeutic perspectives." Nature Reviews Drug Discovery*, 2010. **9**: p. 237.

151. Joerger, A.C. and A.R. Fersht, *"The p53 Pathway: Origins, Inactivation in Cancer, and Emerging Therapeutic Approaches." Annual Review of Biochemistry*, 2016. **85**(1): p. 375-404.

152. Bieging, K.T., S.S. Mello, and L.D. Attardi*, "Unravelling mechanisms of p53-mediated tumour suppression." Nature reviews. Cancer*, 2014. **14**(5): p. 359-370.

153. Soragni, A., "*A designed inhibitor of p53 aggregation rescues p53 tumor-suppression in ovarian carcinomas." Cancer cell*, 2016. **29**(1): p. 90-103.

154. Wilcken, R., *"Kinetic mechanism of p53 oncogenic mutant aggregation and its inhibition." Proceedings of the National Academy of Sciences*, 2012. **109**(34): p. 13584-13589.

155. Wang, G. and A.R. Fersht, *"Multisite aggregation of p53 and implications for drug rescue." Proceedings of the National Academy of Sciences*, 2017. **114**(13): p. E2634-E2643.

156. Wang, G. and A.R. Fersht*, "Propagation of aggregated p53: Cross-reaction and coaggregation vs. seeding." Proceedings of the National Academy of Sciences*, 2015. **112**(8): p. 2443-2448.

157. Ang, H.C., *"Effects of Common Cancer Mutations on Stability and DNA Binding of Full-length p53 Compared with Isolated Core Domains." Journal of Biological Chemistry*, 2006. **281**(31): p. 21934-21941.

158. Costa, D.C.F., *"Aggregation and Prion-Like Properties of Misfolded Tumor Suppressors: Is Cancer a Prion Disease?" Cold Spring Harbor Perspectives in Biology*, 2016. **8**(10).

159. Fersht, A., Structure and mechanism in protein science 1999, New York: W.H. Freeman.

160. Gogna, R., "*Re-oxygenation causes hypoxic tumor regression through restoration of p53 wild-type conformation and post-translational modifications." Cell Death &Amp; Disease*, 2012. **3**: p. e286.

161. Sasaki, M., L. Nie, and C.G. Maki*, "MDM2 Binding Induces a Conformational Change in p53 That Is Opposed by Heat-shock Protein 90 and Precedes p53 Proteasomal Degradation." Journal of Biological Chemistry*, 2007. **282**(19): p. 14626-14634.

162. Ayed, A.*, "Latent and active p53 are identical in conformation." Nature Structural Biology*, 2001. **8**: p. 756.

163. Bell, S.*,"p53 Contains Large Unstructured Regions in its Native State." Journal of Molecular Biology*, 2002. **322**(5): p. 917-927.

164. Wong, K.-B., *"Hot-spot mutants of p53 core domain evince characteristic local structural changes." Proceedings of the National Academy of Sciences of the United States of America*, 1999. **96**(15): p. 8438-8442.

165. Tang, S.-Y., *"Screening for Enhanced Triacetic Acid Lactone Production by Recombinant Escherichia coli Expressing a Designed Triacetic Acid Lactone Reporter." Journal of the American Chemical Society*, 2013. **135**(27): p. 10099-10103.

166. Rajagopalan, S., F. Huang, and A.R. Fersht, *"Single-Molecule characterization of oligomerization kinetics and equilibria of the tumor suppressor p53." Nucleic Acids Research*, 2011. **39**(6): p. 2294-2303.

167. Frisken, B.J., *"Revisiting the method of cumulants for the analysis of dynamic light-scattering data." Applied Optics*, 2001. **40**(24): p. 4087-4091.

168. Safari, M.S., *"Polymorphism of Lysozyme Condensates."* *The Journal of Physical Chemistry B*, 2017. **121**(39): p. 9091-9101.

169. Einstein, A., INVESTIGATIONS ON THE THEORY OF THE BROWNIAN MOVEMENT .Ann. der Physik, 1905.

170. Inman, J.K., *"Thymus-Independent Antigens: The Preparation of Covalent, Hapten-Ficoll Conjugates." The Journal of Immunology*, 1975. **114**(2 Part 1): p. 704-709.

171. Milley, B., *"Optimization, Production, and Characterization of a CpG-Oligonucleotide-Ficoll Conjugate Nanoparticle Adjuvant for Enhanced Immunogenicity of Anthrax Protective Antigen." Bioconjugate Chemistry*, 2016. **27**(5): p. 1293-1304.

172. Kim, J., *"Increasing Binding Efficiency via Reporter Shape and Flux in a Viral Nanoparticle Lateral-Flow Assay." ACS Applied Materials & Interfaces*, 2017. **9**(8): p. 6878-6884.

173. Berne, B.J., Dynamic light scattering : with applications to chemistry, biology, and physics 1976: New York : Wiley, [1976] ©1976.

174. Munishkina, L.A. and A.L. Fink, *"Fluorescence as a method to reveal structures and membrane-interactions of amyloidogenic proteins." Biochimica et Biophysica Acta* (BBA) - Biomembranes, 2007. **1768**(8): p. 1862-1885.

175. Bullock, A.N., *"Thermodynamic stability of wild-type and mutant p53 core domain." Proceedings of the National Academy of Sciences of the United States of America*, 1997. **94**(26): p. 14338-14342.

176. Kelley, L.A., *"The Phyre2 web portal for protein modeling, prediction and analysis." Nature Protocols, 2015*. **10**: p. 845.

177. Knowles, T.P.J., M. Vendruscolo, and C.M. Dobson, *"The amyloid state and its association with protein misfolding diseases." Nat Rev Mol Cell Biol*, 2014. **15**(6): p. 384-396.

178. Knowles, T.P.J., *"An Analytical Solution to the Kinetics of Breakable Filament Assembly." Science*, 2009. **326**(5959): p. 1533-1537.

179. Hartmann, M., Light scattering by small particles. *Von H. C. VANDE HULST. New York: Dover Publications, Inc. 1981. Paperback, 470 S., 103 Abb. und 46 Tab., US $ 7.50.* Acta Polymerica, 1984. **35**(4): p. 338-338.

180. Byington, M.C., *"Shear flow suppresses the volume of the nucleation precursor clusters in lysozyme solutions." Journal of Crystal Growth*, 2017. **468**: p. 493-501.

181. Byington, M.C., *"Protein Conformational Flexibility Enables the Formation of Dense Liquid Clusters: Tests Using Solution Shear." The Journal of Physical Chemistry Letters*, 2016. **7**(13): p. 2339-2345.

182. Šarić, A., *"Physical determinants of the self-replication of protein fibrils." Nature Physics*, 2016. **12**: p. 874.

183. Buck, M., S.E. Radford, and C.M. Dobson*, "A partially folded state of hen egg white lysozyme in trifluoroethanol: structural characterization and implications for protein folding." Biochemistry*, 1993. **32**(2): p. 669-678.

184. Krebs, M.R.*H., "Formation and seeding of amyloid fibrils from wild-type hen lysozyme and a peptide fragment from the β-domain." Journal of Molecular Biology*, 2000. **300**(3): p. 541-549.

185. Chiti, F. and C.M. Dobson, *"Amyloid formation by globular proteins under native conditions." Nature Chemical Biology*, 2008. **5**: p. 15.

186. Friedler, A.*,"Kinetic Instability of p53 Core Domain Mutants: IMPLICATIONS FOR RESCUE BY SMALL MOLECULES." Journal of Biological Chemistry*, 2003. **278**(26): p. 24108-24112.

187. Wang, G. and A.R. Fersht*, "First-order rate-determining aggregation mechanism of p53 and its implications." Proceedings of the National Academy of Sciences of the United States of America*, 2012. **109**(34): p. 13590-13595.

188. De Yoreo, J.J.*, "Cry*stallization by particle attachment in synthetic, biogenic, and geologic environments." *Science*, 2015. **349**(6247).

189. Aich, A., M. Freundlich, and P.G. Vekil*ov, "The free heme concentration in healthy human erythrocytes." Blood cells, molecules & diseases*, 2015. **55**(4): p. 402-409.

190. Babaye Khorasani, F., *"Mobility of Nanoparticles in Semidilute Polyelectrolyte Solutions." Macromolecules*, 2014. **47**(15): p. 5328-5333.

191. He, K., *"Diffusive dynamics of nanoparticles in aqueous dispersions." Soft Matter*, 2012. **8**(47): p. 11933-11938.

192. Giavazzi, F., "*Scattering information obtained by optical microscopy: Differential dynamic microscopy and beyond." Physical Review E*, 2009. **80**(3): p. 031403.

193. Bayles, A.V., T.M. Squires, and M.E. Helgeson, *"Dark-field differential dynamic microscopy*." *Soft Matter*, 2016. **12**(8): p. 2440-2452.

194. Ferri, F., *"Heterodyne near-field scattering: A technique for complex fluids." Physical Review E*, 2004. **70**(4): p. 041405.

195. Magatti, D., *"Dynamic heterodyne near field scattering." Applied Physics Letters,* 2008. **92**(24): p. 241101.

196. He, K.*, "Diffusive Dynamics of Nanoparticles in Aqueous Dispersions." Soft Matter*, 2012. **8**: p. 11933-11938.

197. Provencher, S.W., "CONTIN*: A General Purpose Constrained Regularization Program for Inverting Noisy Linear Algebraic and Integral Equations." Computer Physics Communications, 19*82. **27**(3): p. 229-242.

198. Provencher, S.W., *"Inverse Problems in Polymer Characterization: Direct Analysis of Polydispersity with Photon Correlation Spectroscopy." Die Makromolekular Chemie*, 1979. **180**: p. 201-209.

199. Pan, W., P.G. Vekilov, and V. Lubchenko, *"Origin of Anomalous Mesoscopic Phases in Protein Solutions." Journal of Physical Chemistry B*, 2010. **114**(22): p. 7620-7630.

200. Mie, G., *"Beiträge zur Optik trüber Medien, speziell kolloidaler Metallösungen." Annalen der Physik*, 1908. **330**(3): p. 377-445.

201. Bohren, C.F. and D.R. Huffman, Absorption and Scattering of Light by Small Particles2010, New York: Wiley-Interscience.

202. Wriedt, T., Mie Theory: A Review, W. Hergert and T. Wriedt, Editors. 2012, Springer-Verlag: Berlin, Heidelberg. p. 53-71.

203. Matzler, C. MATLAB Functions for Mie Scattering and Absorption. 2014-10-03].

204. Pan, W., V.V. Uzunova, and P.G. Vekilov, *"Free Heme in Micromolar Amounts Enhances the Attraction Between Sickle Cell Hemoglobin Molecules." Biopolymers*, 2009. **91**(12): p. 1108-1116.

205. He, K., , *"Diffusive Dynamics of Nanoparticles in Arrays of Nanoposts." ACS Nano,* 2013. **7**(6): p. 5122-5130.

206. Kwon, G., B.J. Sung, and A. Yethiraj, *"Dynamics in Crowded Environments: Is Non-Gaussian Brownian Diffusion Normal?" Journal of Physical Chemistry B*, 2014. **118**(28): p. 8128-8134.

207. Lu, P.J., *"Characterizing Concentrated, Multiply Scattering, and Actively Driven Fluorescent Systems with Confocal Differential Dynamic Microscopy."* *Physical Review Letters*, 2012. **108**(21): p. 218103.

208. Reufer, M., *"Differential Dynamic Microscopy for Anisotropic Colloidal Dynamics."* *Langmuir, 2012*. **28**(10): p. 4618-4624.

209. Reufer, M., *"Switching of Swimming Modes in Magnetospirillium gryphiswaldense."* *Biophysical Journal*, 2014. **106**(1): p. 37-46.

210. Gao, Y., J. Kim, and M.E. Helgeson, *"Microdynamics and arrest of coarsening during spinodal decomposition in thermoreversible colloidal gels."* *Soft Matter*, 2015. **11**: p. 6360-6370.

211. Giavazzi, F., *"Structure and dynamics of concentration fluctuations in a non-equilibrium dense colloidal suspension."* *Soft Matter*, 2016. **12**: p. 6588-6600.

212. Jacob, J.D.C., *"Diffusive dynamics of nanoparticles in ultra-confined media."* *Soft Matter*, 2015. **11**: p. 7515-7524.

213. Poling-Skutvik, R., *"Structure and Dynamics of Interacting Nanoparticles in Semidilute Polymer Solutions."* *Macromolecules*, 2016. **49**(17): p. 6568-6577.

214. Cheong, F.C., B.J. Krishnatreya, and D.G. Grier, *"Strategies for three-dimensional particle tracking with holographic video microscopy."* *Optics Express*, 2010. **18**(13): p. 13563-13573.

215. Lee, S.-H., *"Characterizing and tracking single colloidal particles with video holographic microscopy."* *Optics Express*, 2007. **15**(26): p. 18275-18282.

216. Fung, J., *"Imaging multiple colloidal particles by fitting electromagnetic scattering solutions to digital holograms."* *Journal of Quantitative Spectroscopy and Radiative Transfer*, 2012. **113**(18): p. 2482-2489.

217. Fung, J.M., Vinothan N., *"Holographic measurements of anisotropic three-dimensional diffusion of colloidal clusters." Physical Review E*, 2013. **88**(2): p. 020302.

218. Gineste, J.-M., *"Three-dimensional automated nanoparticle tracking using Mie scattering in an optical microscope." Journal of Microscopy*, 2011. **243**(2): p. 172-178.

219. Patterson, E.A. and M.P. Whelan, *"Optical signatures of small nanoparticles in a conventional microscope." Small*, 2008. **4**(10): p. 1703-1706.

220. Ferri, F., *"Kinetics of Colloidal Fractal Aggregation by Differential Dynamic Microscopy." The European Physical Journal*: Special Topics, 2011. **199**(1): p. 139-148.

221. Dai, Q., " *A One-Step Highly Sensitive Method for DNA Detection Using Dynamic Light Scattering.*" *Journal of the American Chemical Society*, 2008. **130**(26): p. 8138-8139.

222. Croccolo, F., H. Bataller, and F. Scheffold, "*Static versus dynamic analysis of the influence of gravity on concentration non-equilibrium fluctuations.*" *The European Physical Journal E: Soft Matter and Biological Physics*, 2014. **37**(11): p. 105-5.

223. Oprisan, A., "*Direct imaging of long-range concentration fluctuations in a ternary mixture." The European Physical Journal E: Soft Matter and Biological Physics*, 2015. **38**(3): p. 17-9.

224. Ahadi, A., S.V. Varenbergh, and M.Z. Saghir, "*Measurement of the Soret coefficients for a ternary hydrocarbon mixture in low gravity environment.*" *Journal of Chemical Physics*, 2013. **138**(20): p. 204201-18.

225. Kruse, J.-P. and W. Gu, "*Modes of p53 Regulation." Cell*, 2009. **137**(4): p. 609-622.

226. Kruse, J.-P. and W. Gu, "*SnapShot: p53 Posttranslational Modifications." Cell*, 2008. **133**(5): p. 930-930.e1.

227. Vogelstein, B., D. Lane, and A.J. Levine, *"Surfing the p53 network.*" *Nature*, 2000. **408**(6810): p. 307-310.

228. Enami, M. and A. Ishihama, *"Protein phosphorylation in Escherichia coli and purification of a protein kinase*." *Journal of Biological Chemistry*, 1984. **259**(1): p. 526-533.

229. Kumar, D.K.V., *"Amyloid-β peptide protects against microbial infection in mouse and worm models of Alzheimer's disease." Science Translational Medicine*, 2016. **8**(340): p. 340ra72-340ra72.

230. White, E., "*The role for autophagy in cancer*." *The Journal of Clinical Investigation*, 2015. **125**(1): p. 42-46.